UTRECHT UNIVERSITY

DEBYE INSTITUTE

SOFT CONDENSED MATTER

Optical properties and alloying of metal nanorods

Author:
T.A.J. WELLING

Supervisors:
WIEBKE ALBRECHT
Prof. Dr. ALFONS VAN BLAADEREN

Master thesis
February 9, 2017

Abstract

In this thesis we study the plasmonic properties and alloying process of metallic nanoparticles (NPs) by means of experiments and calculations. Specifically, we mainly focus on Au nanorods (NRs) and bimetallic Au-Ag core-shell or alloyed NRs. Firstly, Mie-Gans theory, modified to fit our needs, was employed to analytically calculate extinction cross sections for these systems. We found that alloyed NRs had a relatively bad plasmonic performance compared to pure Au NRs. Subsequently, we studied the radiative decay of the localized surface plasmon resonance (LSPR) of metal NPs using finite-difference time-domain (FDTD) calculations and discovered a dependence on resonance energy and dielectric constant of the medium for various metals, including a reduced radiative decay rate at resonance energies for which interband transitions occur. Furthermore, we analyzed experimental ensemble extinction spectra by using our knowledge of Mie-Gans modelling and damping mechanisms, and determined important parameters from the extinction spectrum like the aspect ratio distribution and sample concentration. By comparing the extracted results with proven characterization methods, the accuracy and limits of this approach were investigated.

In the second part of the thesis we employed the from calculations obtained knowledge to analyze measurements on silica-coated Au-Ag core-shell and alloyed NRs. Core-shell NRs were first synthesized and then characterized via transmission electron microscopy (TEM) and visible-near infra-red (vis-NIR) Fourier Transform Infra-red (FTIR) spectroscopy. With the synthesized silica-coated Au-Ag core-shell NRs we studied the alloying process of Au-Ag NRs with thermal heating experiments, that we followed in-situ with vis-NIR FTIR spectroscopy. From these measurements we determined activation energies (E_A) for diffusion in the NRs that were two to three times lower than the activation energies for Au and Ag atoms in bulk Au-Ag alloys. To determine whether the alloying process depends on the shape of the NPs, we compared nanospheres and NRs of the same volume and Au-Ag composition in in-situ heating experiments in an electron microscope. No difference in alloying temperature was observed, indicating that the NR shape did not facilitate the alloying process.

Contents

1   Introduction

Metals are very common in our everyday lives and are known for conducting electricity well. Metals are good conductors because the electrons are not tightly bound to their respective atom cores. The electrons are free to move around the metal and can be manipulated by e.g. applying a voltage. An electromagnetic wave such as a light wave can also manipulate these free charges. In order to make use of this manipulation, it is possible to make metal NPs that have dimensions much smaller than the wavelength of light, which is on the order of 500-1000 nm. In fact, the size of these NPs is around the penetration depth of an electromagnetic field in a metal, which is around 20 nm for noble metals at a wavelength of 500 nm. It is the size that results in different properties of these NPs compared to bulk metals. One of these properties is related to the response of the free electrons in such a NP to an incoming light wave. Since metal NPs are significantly smaller than optical wavelengths, all electrons in the metal are affected by the electric field component of a light wave. The charges are separated due to the electric field, which results in a restoring force which attempts to restore the charge distribution. When the eigenfrequency of this restoring force matches the frequency of the incoming light, the electron oscillation is in resonance. At this resonance wavelength a localized surface plasmon resonance (LSPR) occurs. It is this resonance behaviour that causes interesting optical properties. When an incoming light wave interacts with the metal NP, strong scattering and absorption of light happens at the resonance wavelength. The scattering and absorption is especially strong in noble metals, like gold and silver.

Interestingly, the LSPR was already made use of as far back as the Roman era. Albeit unknowingly, they used the plasmon effect of Au NPs to make a bright red colour in glass-stained windows and cups. The interest of scientists in plasmons resonances dates back to the beginning of the twentieth century, when in 1908 Gustav Mie solved Maxwell's equations analytically for the interaction of an electromagnetic plane wave with a spherical NP.[1] In 1912 Richard Gans expanded on Mie's theory by solving Maxwell's equations for small anisotropic spheroidal NPs.[2] Experimental characterization of the plasmon resonance of small Au and Ag spherical NPs was not achieved until 1970 by Kreibig and Zacharias.[3] The interest in plasmonic NPs was revitalized when synthesis methods improved. This allowed more complex metal nanostructures to be made, such as NRs,[4-6] nanoprisms,[7-9] bipyramids[5] and nanoshells.[10]

The increased availability of various shapes has sparked scientific interest in metal NPs due to their tunable optical and photothermal properties, stemming from LSPRs. These resonances can be tuned by changing the size, shape, dielectric environment and composition of the NP.[11-13] Specifically, the NR shape is of great interest. NRs have a transverse LSPR along the short axes of the NR and a longitudinal LSPR along the long axis of the NR. The longitudinal LSPR can be tuned with the aspect ratio and spans the visible until the near-infrared (NIR) region of the spectrum for noble metal NRs. Metal nanorods are superior to metal nanospheres as their plasmonic properties are stronger, leading to sharper and more intense plasmon resonance peaks. They consequently also exhibit stronger local field enhancements near the surface of the NP, especially at the tips.

From all metals, Ag has the least lossy plasmonic properties in the ultraviolet and visible regime due to low intrinsic damping,[14-18] but Au NPs are most often used, because Au is more chemically stable than Ag. For that reason, especially Au NRs are employed in a wide variety of applications. For example, 5-dimensional optical data storage with Au NRs makes use of the wavelength tunability and the polarization dependence of the LSPR of the NRs.[19] Furthermore, small deviations in parameters that shift the resonance wavelength, such as the dielectric environment around metal NRs, are accurately detectable, which makes them particularly suitable for sensing applications where small amounts of analytes bind to the surface of a NR.[20] Interestingly, the large electric field enhancements that are a result of the plasmon resonance are especially useful for surface-enhanced Raman scattering (SERS)[21] and photovoltaics.[22]

An understanding of the decay channels of the LSPR is important for applications, as the decay of the LSPR determines how sharp and intense the plasmon resonance peak is. We can distinguish bulk damping and size-dependent damping mechanisms of the LSPR in plasmonic NPs. Electron-surface scattering is an important damping mechanism for sizes below 20 nm, whereas radiation damping is the cause of size-dependent dephasing at sizes above 20 nm. How these size-dependent damping mechanisms are influenced by parameters such as shape and resonance energy is not yet clear. Specifically, the radiation damping of the LSPR, which occurs, amongst others, due to photon emission of the radiative dipole, is not yet fully understood.

Bimetallic Au-Ag alloyed NPs combine the good plasmonic properties of Ag with the stability of Au. The composition can be used to have additional tunability of the LSPR frequency. Furthermore, Au-Ag alloyed NPs are interesting for catalysis, as it was shown that Au-Ag alloyed NPs with both atom species available as active sites were more catalytically active for e.g. CO conversion than either Au or Ag monometallic NPs.[23] They could also be useful in photocatalysis were the LSPR is used to enhance the catalytic activity.[24] Ideally, the stability of Au and the good plasmonic performance of Ag is combined in a NR shape, as recently synthesized by Albrecht and Van der Hoeven et al.[25] The influence of size, shape and Au/Ag ratio on the alloying process has not yet been investigated.

In this thesis, we use a combination of calculations and experiments to look at several aspects of metal NPs. In chapter 2, we delve into the theory of plasmonics and employ analytical modelling of plasmon resonances with Mie-Gans theory to get a good perception of the factors that influence the plasmonic properties of metal NPs. The influences of the surrounding medium, as well as the size and shape of single metal NPs on the plasmon resonance are investigated from a modelling point of view. Furthermore, we study the influence of the composition of bimetallic NPs on the plasmon resonance. More specifically, the plasmonic properties of Au-Ag core-shell and alloyed NPs are reviewed. Chapter 3 provides a systematic study of the radiative decay of the plasmon resonance of Au, Ag, Cu and Al NPs with FDTD calculations. In chapter 4 we look to improve the characterization of plasmonic NP samples by combining extinction spectroscopy and Mie-Gans theory to extract useful information from ensemble extinction measurements. We discuss the obtained aspect ratio distributions and concentrations by comparing them to known characterization methods. We also determine the dephasing of the LSPR due to electron-surface scattering from inhomogeneously broadened ensemble spectra. In chapter 5 we study the influence of size, shape and Au/Ag ratio on the alloying process of Au-Ag NRs. We synthesized Au-Ag NRs coated with mesoporous silica and use them for heating experiments. First we thermally heated the NRs and followed the alloying process in-situ with extinction spectroscopy measurements. Second, in-situ heating measurements in the electron microscope were conducted for Au-Ag nanorods and nanospheres. The third experiment revolved around the heating of Au-Ag NRs by excitation with a femtosecond laser. Finally, chapter 6 provides a summary of this thesis and an outlook is given as well.

2   Theory & modelling of plasmons

2.1   Plasmons

A plasma is a large number of freely moving charged particles i.e. electrons in a metal. A plasmon is a quantum of plasma oscillation. They mainly exist in metals as collective oscillations of conduction electrons. There are different types of plasmons: bulk, surface and localized surface plasmons. Bulk plasmons are collective oscillations of electrons in the bulk of the metal. A simple model to describe the behaviour of bulk plasmons is the free electron model,[26] which models the plasmon as an electron cloud that freely propagates over a background of positively charged atom cores. We can define the equation of motion for each electron in the oscillation due to a time-dependent electric field, oscillating at frequency ω, $\boldsymbol{E}(t) = \boldsymbol{E_0} e^{i\omega t}$ as

$$m\ddot{\boldsymbol{x}}(t) = -m\gamma\dot{\boldsymbol{x}}(t) - e\boldsymbol{E}(t) \tag{2.1}$$

where m and e are the electron mass and charge respectively, $\boldsymbol{x}(t)$ is the displacement of an electron from their equilibrium position and γ is the intrinsic damping of the metal, due to electrons scattering off of phonons, defects, impurities or other electrons, which happens with a characteristic rate $\gamma = 2/T$, where T is the relaxation time. The solution to the free electron model is given by

$$\boldsymbol{x}(t) = \frac{e}{m(\omega^2 + i\gamma\omega)}\boldsymbol{E}(t) \tag{2.2}$$

Due to the displacement of the electrons relative to the atom cores there is a polarization $\boldsymbol{P} = -ne\boldsymbol{x}$, with n the electron density. As a consequence of the polarization the electrons must be displaced once more. The dielectric displacement $\boldsymbol{D}$ is defined as

$$\boldsymbol{D} = \varepsilon_0\boldsymbol{E} + \boldsymbol{P} = \varepsilon_0\varepsilon\boldsymbol{E} \tag{2.3}$$

where ε is the dielectric function, which is an important property of a metal as it determines the response of electrons to an electric field. We can write the dielectric function ε in terms of the dielectric constant of vacuum ε_0, the electric field $\boldsymbol{E}$ and the polarization $\boldsymbol{P}$

$$\varepsilon(\omega) = 1 + \frac{\boldsymbol{P}}{\varepsilon_0\boldsymbol{E}} = 1 - \frac{\omega_p^2}{\omega^2 + i\gamma\omega} \tag{2.4}$$

where the plasmon frequency ω_p is a material property and is defined as

$$\omega_p = \sqrt{\frac{ne^2}{\varepsilon_0 m}} \tag{2.5}$$

For most metals, the plasma frequency ω_p lies in the ultra-violet regime ($5 - 15\,eV$), which is the frequency at which the collective longitudinal excitation mode would be formed. We revisit the plasma frequency of metals in more details when we explore the influence of a material's dielectric function on plasmons.

Surface plasmon polaritons are electromagnetic excitations that propagate along the interface between a metal and a dielectric medium. An electromagnetic wave propagates in the dielectric medium, whereas an oscillating electron plasma, the surface plasmon, resides in the metal. The field in the dielectric medium typically has a penetration depth of $\lambda/2$, while for the metal the penetration depth is determined by the skin depth, which is of the order of $20\,nm$ for plasmonic materials in the visible light regime.

For metallic NPs with sizes of the order of the skin depth of the metal, all the electrons in the NP are shifted by an electric field (Figure 2.1). As a result the charge distribution in the NP is inhomogeneous. A restoring force, due to positive lattice ions attracting the built-up negative charge, attempts to restore charge homogeneity. When the frequency
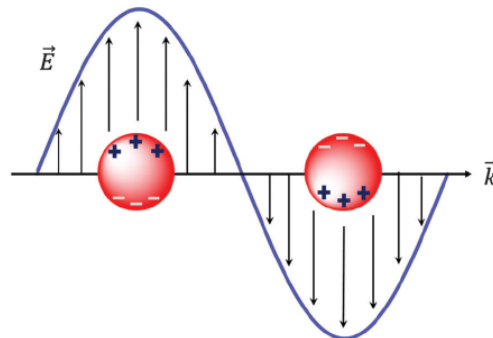

Figure 2.1: The shifting of conduction electrons in a NP by the electric field of the light.[27]

of the excitation light is in resonance with the eigenfrequency of the restoring force, a strong oscillation occurs, which is known as the localized surface plasmon resonance (LSPR). This behaviour is well modelled by a driven, damped harmonic oscillator,

$$m\ddot{\boldsymbol{x}}(t) = -K\boldsymbol{x}(t) - m\gamma\dot{\boldsymbol{x}}(t) - e\boldsymbol{E}(t) \tag{2.6}$$

where $K = m\omega_0^2$ and ω_0 is the eigenfrequency of the restoring force. As it is a driven, damped oscillator, the solution we seek is the non-decaying particular solution, which is independent of the initial conditions. Complex variables will be used to obtain the particular solution. We therefore use z as a variable, where $\boldsymbol{x}(t) = Re[\boldsymbol{z}(t)]$. The equation of motion is now

$$m\ddot{\boldsymbol{z}}(t) = -K\boldsymbol{z}(t) - m\gamma\dot{\boldsymbol{z}}(t) - e\boldsymbol{E_0}e^{i\omega t} \tag{2.7}$$

With $\boldsymbol{z}(t) = \boldsymbol{z_0}e^{i\omega t}$ as a solution, we solve for $\boldsymbol{z_0}$:

$$\boldsymbol{z_0} = \frac{e\boldsymbol{E_0}/m}{(\omega_0^2 - \omega^2) + i\gamma\omega} = \frac{e\boldsymbol{E_0}}{m}\frac{(\omega_0^2 - \omega^2) - i\gamma\omega}{(\omega_0^2 - \omega^2)^2 + \gamma^2\omega^2} \tag{2.8}$$

Rewriting $\boldsymbol{z_0}$ in polar coordinates gives

$$\boldsymbol{z_0} = \frac{e\boldsymbol{E_0}}{m}\frac{\sqrt{(\omega_0^2 - \omega^2)^2 + \gamma^2\omega^2}}{(\omega_0^2 - \omega^2)^2 + \gamma^2\omega^2}e^{i\phi} = \frac{e\boldsymbol{E_0}}{m}\frac{1}{\sqrt{(\omega_0^2 - \omega^2)^2 + \gamma^2\omega^2}}e^{i\phi} \tag{2.9}$$

with ϕ the phase of the oscillation, where

$$tan(\phi) = \frac{\gamma\omega}{\omega_0^2 - \omega^2} \tag{2.10}$$

The real displacement $\boldsymbol{x}(t)$ is now given by $\boldsymbol{x}(t) = Re[\boldsymbol{z}(t)] = Re[\boldsymbol{z_0}e^{i\omega t}]$ as

$$\boldsymbol{x}(t) = \frac{e\boldsymbol{E_0}}{m}\frac{1}{\sqrt{(\omega_0^2 - \omega^2)^2 + \gamma^2\omega^2}}cos(\omega t + \phi) \tag{2.11}$$

Equation 2.11 confirms that the amplitude is highest when the frequency of the incoming light wave equals the eigenfrequency of the restoring force: $\omega = \omega_0$. The resonance frequency is therefore mainly determined by the strength of the restoring force, which depends on the separation between the surface charges (size and shape) and the polarizability of the material the NP is made of as well as its surrounding medium.

To investigate the lineshape we expect in the frequency domain for LSPRs, we consider a decaying oscillation with eigenfrequency ω_0 described by $A(t) = A_0 cos(\omega_0 t)e^{-\gamma t}$. The Fourier transform gives

$$A(\omega) = \mathscr{F}(A(t)) = A_0\sqrt{\frac{2}{\pi}}\frac{\gamma}{(\omega - \omega_0)^2 + \gamma^2} \tag{2.12}$$

which is a so-called Lorentzian lineshape. Equation 2.12 is characterized by the resonance frequency ω_0 and the full-width-at-half-maximum (FWHM). It can be shown that half of the maximum value of a Lorentzian lineshape is reached at $|\omega - \omega_0| = \gamma/2$, so the FWHM is described by the parameter γ, which is called the damping facto.[28]

2.2 The dielectric function and plasmon resonance decay

2.2.1 The dielectric function

It is good to explore what happens when light interacts with such a plasmonic NP. The plasmon has a dipolar character, because electrons are shifted to one side of the NP, giving that side a negative charge and the opposite side a positive charge. At the LSPR frequency, the incoming light is absorbed and scattered strongly due to this dipolar character. In order to fully describe plasmon resonances, a description of how a NP of a certain metal interacts with light is required. From the free electron model, we learnt that the influence of both an incoming field and the induced polarization could be described by the dielectric function in Eq. 2.4. Therefore, we will closely examine the dielectric function to describe the interaction of a metal NP with incoming light.

The dielectric function can be split in a real and imaginary part. The real part is related to the energy stored in the metal and describes how easily the metal is polarized and needs to be negative for a plasmon to exist in the material. The imaginary part is related to the loss of energy in the metal and describes the damping of the plasmon. For well-performing plasmonic materials, we therefore require the ratio of real and imaginary part of the dielectric function to be as high as possible. For this ratio to be high, the material needs to be easily polarizable and the loss of energy, i.e. damping, in the

material must be minimized. The polarization, determined by the real part of the dielectric function, is just an energy-dependent material property, whereas damping can depend on multiple factors for plasmonic NPs, as we explore later.

We can write the dielectric function in two parts, namely the dielectric function due to interband transitions and due to intraband transitions.

$$\varepsilon(\omega) = \varepsilon_{intra}(\omega) + \varepsilon_{inter}(\omega) \tag{2.13}$$

The interband contribution to the dielectric function is caused by transitions of electrons between the d-band of a metal and the conduction band with the energy absorbed from the incoming light wave. This contribution is normally modelled by using Lorentzian oscillators[14,29,30] and is negligible when the incoming photons do not have sufficient energy for interband excitations (e.g. below 1.8 eV for Au and 3.5 eV for Ag). Intraband damping is caused by the nearly-free electrons in a metal scattering off of other electrons, phonons, impurities and defects and is described by the Drude free electron model. The dielectric function of a bulk metal is thus given by

$$\varepsilon(\omega) = \varepsilon_\infty - \frac{\omega_p^2}{\omega^2 + i\gamma\omega} + \varepsilon_{inter}(\omega) \tag{2.14}$$

Here, ε_∞ is the contribution to the dielectric function from high-energy transitions. The material-dependent electron plasma frequency is given by ω_p, which is, as derived previously, related to the electron density n, the charge of an electron e and the effective mass of the electron m via

$$\omega_p^2 = \frac{ne^2}{\varepsilon_0 m}. \tag{2.15}$$

The plasma frequency ω_p is the typical electrostatic oscillation frequency of electrons in a certain material in response to a charge separation and is partly responsible for the restoring force. It is therefore obvious that the material's plasma frequency plays a crucial role in the LSPR of a metal NP.

2.2.2 Damping mechanisms

The damping factor γ does not only depend on the metal for NPs, but also on the size and shape of the NP. We can define a size-dependent dielectric function, in which this damping factor has multiple contributions.

$$\gamma = \gamma_b + \gamma_s + \gamma_r \tag{2.16}$$

Here, γ_b is the bulk damping, γ_s the electron-surface scattering and γ_r the radiation damping. The bulk damping γ_b describes the intrinsic damping that is also present in bulk material, like interband damping and intraband damping. The intraband contribution to the bulk damping is related to the mean free path l of electrons in the metal by v_F/l, where v_F is the material-dependent Fermi velocity.

For bulk gold, the electron mean free path at room temperature is around 20 nm. An electron-surface scattering contribution γ_s comes into play when the effective mean free path of the electrons changes due to the limited size of the NP, i.e. when it is smaller than the mean free path in the bulk metal.[31] The effective mean free path is then decreased due to electrons scattering off of the small NP's surface. It is therefore reasonable to describe the surface-scattering contribution in a similar way as other electron scattering contributions, which gives

$$\gamma_s = \frac{Av_F}{l_{eff}} \tag{2.17}$$

This contribution depends on the the Fermi velocity v_F, the effective mean free path of the electrons l_{eff} and A, which is a constant that depends on details of the electron-surface interaction. We use a description for the effective mean free path of electrons which is derived from a billiard model, in which l_{eff} is calculated for arbitrary shape as $l_{eff} = 4V/S$, where V is the volume and S the surface area of the particle.[32,33] The electron-surface interaction constant A has been determined experimentally by several authors.[34–40] For Au NRs of aspect ratios between 2 and 4, Novo et al.[34] found $A = 0.27$, which agrees with Hu et al.[35] who got $A = 0.30 \pm 0.03$ for Au NRs of aspect ratio 3. Both values were obtained via dark-field scattering experiments. When the dimensions of the NP are below 10 nm the energy levels of the electrons start to be discretized by quantum effects, and this description for γ_s can no longer be used.[41] Another surface damping phenomenon observed in experiments is chemical interface damping (CID), which depends on the chemical species attached to the interface and the charge transfer between the NP and the medium,[42,43] which is not described by Equation 2.17. To the best of our knowledge no accurate description for CID exists.

The radiation damping γ_r describes the damping due to electrons losing their energy via photon emission. Radiation damping is proportional to the volume of the NP and can be described as[28]

$$\gamma_r = 2\hbar\kappa V \tag{2.18}$$

where $\hbar = h/2\pi$ is the reduced Planck constant. Quantifying the κ parameter is a problem. A few measurements on Au and Ag NPs were performed to quantitatively obtain κ but different values were reported. For instance, Sönnichsen et al.[28] found $\kappa = 4 \times 10^{-7}\,\mathrm{fs}^{-1}\mathrm{nm}^{-3}$ for spherical Au NPs. Hu et al.[35] obtained $\kappa = 6.2 \times 10^{-7}\,\mathrm{fs}^{-1}\mathrm{nm}^{-3}$ for Au NRs of average aspect ratio 3, while Novo et al.[34] extracted $\kappa = 7 \times 10^{-7}\,\mathrm{fs}^{-1}\mathrm{nm}^{-3}$ for Au NRs of aspect ratios 2 to 4. For Ag nanoprisms $\kappa = 12 \times 10^{-7}\,\mathrm{fs}^{-1}\mathrm{nm}^{-3}$ was obtained.[44] In chapter 3 we will use numerical calculations to show that κ depends on the resonance energy of the LSPR.

2.2.3   Dielectric functions for Au-Ag alloys

We have seen that the metal and size of the NP has an influence on the dielectric function and thus on the plasmon resonance. Since chapter 5 deals with alloying of Au-Ag core-shell NRs, we also investigate the influence of the composition on the dielectric function for alloys.

The dielectric functions for noble metals are well known.[16–18, 45–48] Less measurements exist for the dielectric functions of alloy compositions.[14, 15, 49] It has been established that a weighted average of the dielectric functions of Au and Ag cannot reproduce the experimental ellipsometry data for alloy dielectric functions.[15] Ellipsometry data measured by Peña-Rodríguez et al.[15] lead to a Drude model for Au-Ag alloys, where the dielectric function depends on the Au molar fraction. Although this model only works in the energy region below interband transitions (by them reported as 3.1 eV for Ag, 2.1 eV for Au and varying linearly between those two as a function of composition for alloys), it does give us an analytical dielectric function to predict plasmon resonances in this region which is significant for certain applications. Another analytical dielectric function for Au-Ag alloys was developed by Rioux and co-workers.[14] This dielectric func-
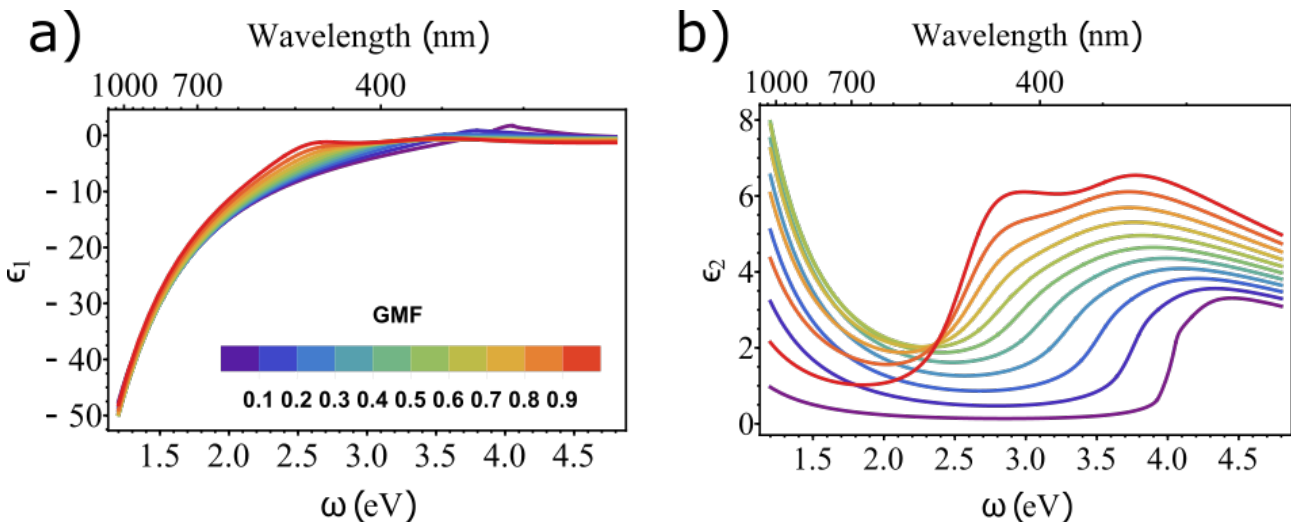

Figure 2.2: a) Real and b) imaginary part of the dielectric function $\varepsilon(\omega)$ of Rioux et al.[14] for Au-Ag alloys. The composition of the alloy is characterized with the gold molar fraction (GMF). A GMF of 1 is pure gold (red) and a GMF of 0 is pure silver (purple).

tion spans the whole energy range due to the inclusion of interband transitions. It is based on the band structure of the metals and modelled by Lorentzian oscillators.[14] Their model uses a total of 10 parameters to describe the dielectric function of the metal over an energy range from 1 to 5 eV. Due to the similar band structures of Au and Ag, Rioux et al.[14] assume the model to be identical for Au, Ag and alloy compositions. Only the parameter values in the model change for different compositions. The smooth composition dependence of the parameters are modelled with a second-order polynomial composition function, which is fully determined by the parameter values for pure Au, pure Ag and the 50/50 composition. This yields a complete dielectric function that depends on energy and composition with 30 variable parameters. We use the dielectric function of Rioux et al.[14] for modelling the optical response of metal NPs throughout this thesis. The dielectric function can be modelled for different compositions, which is shown in Figure 2.2. In these plots, the Au molar fraction (GMF) is used to show the composition of the alloy. Pure Au has a Au molar fraction of one (red in Figure 2.2), while pure Ag has a Au molar fraction of zero (purple).

It can be seen that the real part of the dielectric function of the pure metals and alloys do not differ overly much. Only in the regime from 1.5 to 3.5 eV the alloys with more Ag have a significantly greater negative value for ε_1, indicating that the metal is more easily polarizable in this energy regime for those compositions. We see that between 3.8 and 4.5 eV, the real part of the dielectric function of Ag is positive, meaning plasmons cannot exist in Ag in that energy range. The different alloy compositions with less than 80% Ag do not have a positive real part in the energy regime shown here.

As mentioned before, the imaginary part of the dielectric function describes the energy lost in the material and therefore determines the damping of the plasmon resonance. If we look at pure Au, we see that interband damping indeed starts to play a role for energies higher than approximately 1.8 eV. For Ag this threshold is around 3.9 eV. For alloy compositions the onset for interband damping is less well defined, but it exists in between the threshold energies of pure Au and Ag. For an alloy with a high molar fraction of Au (Ag) the threshold is closer to pure Au (Ag). We compare the alloy plasmonic properties to those of Au. This is because Au is the most used metal for plasmonic NPs due to its stability, whereas Ag is less chemically stable in most media. For energies above 1.8 eV, beyond the onset of interband transitions for Au, the compositions that contain more Ag experience less damping. This is because the onset for interband transitions only happens at higher energies for these compositions. The more Ag in the alloy, the higher the energy needed to excite electrons from the d-band to the conduction band, which is a competing energy loss mechanism for the plasmon. Thus, alloy compositions with more Ag have better plasmonic properties than Au in the energy regime beyond the interband transition onset for Au at 1.8 eV. The imaginary part of the dielectric function of Au-Ag alloys also shows that more energy is lost in alloyed NPs than Au NPs below 1.8 eV. This indicates that the plasmonic properties of alloys in the energy regime below 1.8 eV are worse than pure Au or pure Ag. This may be due to more defects and impurities in the alloy compositions compared to the pure metals, even though the lattice constants of Au and Ag are comparable. The small difference in lattice constants of Au and Ag may also result in significant differences between atoms due to loss of periodicity. The loss of periodicity in an alloy NP can be explained by the differences in electronegativity between Au and Ag (2.54 and 1.93 respectively, in the Pauling scale).[15,50] Electronic density is transferred from Ag to Au, which likely stresses and/or distorts the lattice, causing the additional damping.[15] The most understandable way to look at these influences on the damping of a plasmon is by looking at the behaviour of the restoring force. If there are extra defects and impurities or extra stresses in an atom lattice, the positive atom core background is not homogeneous over the volume of the NP. This means that every location has a different contribution to the total restoring force. The restoring force then acts more forcefully on certain electrons and has less influence on electrons in a different part of the NP. This leads to an inhomogeneous distribution of local plasmon frequencies. As a consequence, the dephasing of the total localized surface plasmon resonance is much faster. We have two energy regimes. One regime below 1.8 eV where alloy compositions generally have worse plasmonic properties than Au. In the other energy regime above 1.8 eV, the alloy compositions perform better with high Ag fractions, due to the shift in the onset of interband transitions.

It needs to be mentioned that different ellipsometry data for alloy compositions give different dielectric functions. The data of Peña-Rodríguez et al. is fairly similar to those of Rioux and coworkers.[14,15] However, the data found by Gong et al. show suppressed energy losses of the 50/50 Au/Ag alloy composition compared to Au over the whole investigated wavelength range ($200 - 1000$ nm).[49] Thus, more research on alloy dielectric functions and alloyed NPs is needed to fully understand the optical response of these materials.

2.3 Mie-Gans theory

In order to study the localized surface plasmon resonance (LSPR) of a NP, we need to calculate the extinction cross section of that NP. The optical response of a metal NP is determined by Maxwell's equations. For a spherical NP, the Maxwell equations were solved exactly in 1908 by Mie.[1] Gans extended the theory for spheroidal NPs that are much smaller than the wavelength of the incoming light.[2] Mie-Gans theory only takes the dipole term of the plasmon resonance into account, which is applicable for NRs that have diameters smaller than 30 nm. Because the NPs are much smaller than the wavelength of the light, the electric field can be approximated as being static. This is called the quasi-static approximation. The main input for modelling the plasmon resonance of a NP of a certain metal is the dielectric function as it describes the response of electrons in a metal under influence of an electric field. We use the model based on the data of Rioux et al. to model the plasmon resonances of Au, Ag and alloy NPs.[14] Other important parameters such as size, aspect ratio and surrounding medium, which are described later, also affect the plasmon resonance. In the following, the equations needed to accurately describe the extinction spectra of spheroidal NPs with Mie-Gans theory is given and briefly discussed.

Firstly, the polarizability of an elongated particle parallel to one of its principal axes needs to be calculated in the quasi-static approximation.

$$\alpha_x = \frac{V(\varepsilon(\omega) - \varepsilon_m)}{\varepsilon_m + L_x(\varepsilon(\omega) - \varepsilon_m)} = \frac{V}{L_x + \frac{\varepsilon_m}{\varepsilon(\omega) - \varepsilon_m}} \tag{2.19}$$

Here α_x is the polarizability of the particle along a certain principal axis, V the volume, $\varepsilon(\omega)$ the dielectric function of the metal, ε_m the dielectric constant of the surrounding medium and L_x the shape factor for the polarizability along the x, y or z axis. In Mie-Gans theory for spheroids this shape factor of the long axis is related to the aspect ratio via the following relation:

$$L_x = \frac{1 - e^2}{e^2} \left(\frac{1}{2e} Ln \left(\frac{1 + e}{1 - e} \right) - 1 \right) \tag{2.20}$$

Here e is related to the aspect ratio (AR) as

$$e = \sqrt{1 - \frac{1}{AR^2}} \tag{2.21}$$

The shape factor of the shorter axes is then given by

$$L_y = L_z = \frac{1 - L_x}{2} \tag{2.22}$$

L_x is always lower than L_y and L_z. Therefore, the polarizability along the long axis of the spheroid is larger than the polarizability along the short axis. However, these shape factors do not correctly describe experimental NRs, since their shape rather resembles the shape of a spherocylinder, which is a cylinder capped with hemispheres. Prescott and Mulvaney determined corrected shape factors which can be used for better results by correlating DDA simulations and Mie-Gans theory for these shapes.[51] Due to the differences in polarizability for the long axis and the short axes, NRs have two different LSPR modes: a longitudinal mode along the long axis of the NR and a transverse mode along the short axes of the NR. Because of the higher polarizability of the longitudinal mode, the longitudinal LSPR is more intense and more interesting. In this work we therefore focus on the longitudinal LSPR. By combining Mie-Gans theory with the shape factors found by Prescott & Mulvaney we can describe the extinction cross sections of experimentally synthesized NRs due to the longitudinal LSPR.[51] Unless otherwise mentioned, we model spherocylinders for the remainder of this chapter.

The polarizability in the electrostatics approximation only gives accurate results for NPs with a radius lower than 15 nm. For larger NPs higher order terms can be added to the polarizability to include retardation effects. Several attempts at achieving this have been made in literature. Kuwata et al. expanded the first TM mode of the Mie formulation, which is applicable to NPs of any shape.[52] The polarizability along the long axis for NPs up to 25 nm radius is then given by

$$\alpha_x^{Kuwata} = \frac{V}{L_x + \frac{\varepsilon_m}{\varepsilon(\omega) - \varepsilon_m} + A\varepsilon_m x^2 + B\varepsilon_m^2 x^4 - i\frac{4\pi^2 \varepsilon_m^{3/2}}{3}\frac{V}{\lambda^3}} \tag{2.23}$$

where $x = \pi a / \lambda$ is the size parameter for a spheroidal NP of length a, and A and B are fit parameters. These fit parameters determine the energy-shift due to retardation effects. The imaginary contribution to the denominator describes the radiative damping caused by dynamics beyond the quasi-static approximation. However, the most common way to describe the optical response of larger NPs beyond the quasi-static approximation is the Modified Long Wavelength Approximation (MLWA), which also includes radiation damping. This approximation describes the polarizability of larger NPs as[53,54]

$$\alpha_x^{MLWA} = \frac{\alpha_x}{1 - \frac{k^2}{4\pi a}\alpha_x - i\frac{1}{6\pi}k^3\alpha_x} \tag{2.24}$$

where a is half the length of the NR. The second term in the denominator is due to dynamic depolarization, which red-shifts the plasmon resonance as the NP gets bigger. The imaginary term in the denominator describes the radiative damping. Notice that these two approximations for the polarizability, α_x^{Kuwata} and α_x^{MLWA}, are descriptions for spheroids and cannot be used in combination with the shape factors from Prescott et al. to describe spherocylinders.[51]

The wavevector for light in a surrounding medium is given by

$$k = 2\pi \frac{\sqrt{\varepsilon_m}}{\lambda} \tag{2.25}$$

where k is the wavevector of the light in the medium and λ the wavelength of the light in vacuum. To analyze the far-field optical performance of NPs, the scattering and absorption cross sections need to be calculated. The scattering, absorption and extinction spectra depend only on the wavevector and polarizability (Eq. 2.25 and 2.19, respectively). The cross sections are given by the following equations

$$C_{sca} = \frac{k^4}{6\pi}|\alpha|^2 \tag{2.26}$$

$$C_{abs} = kIm(\alpha) \tag{2.27}$$

$$C_{ext} = C_{sca} + C_{abs} \tag{2.28}$$

where C_{sca}, C_{abs} and C_{ext} represent the scattering, absorption and extinction cross sections, respectively. Thus, the scattering cross section of the NPs depends on the absolute value of the polarizability squared, while the absorption cross section only depends on the imaginary part of the polarizability. The bigger the particle, the more it scatters, while the relative contribution of absorption to the total extinction diminishes.
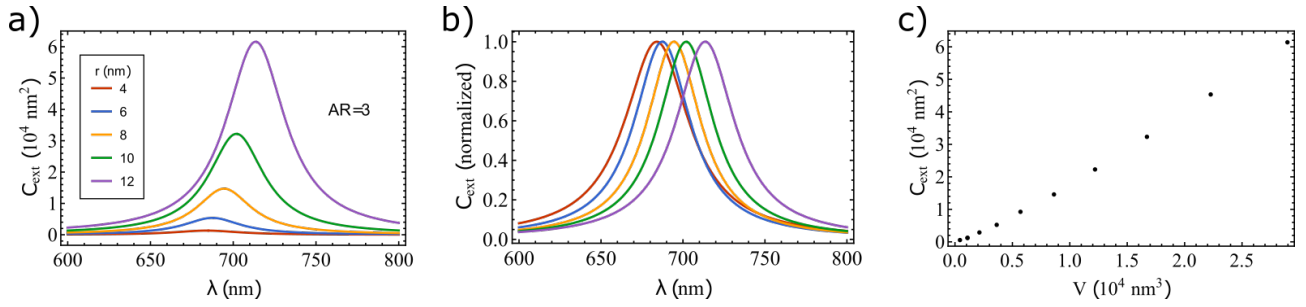
Figure 2.3: a) Extinction cross sections (C_{ext}) calculated with Mie-Gans theory for Au NRs of aspect ratio (AR) 3 in water for different radii (r). b) Normalized calculated extinction cross sections of a), showing the broader spectrum for the very small NP due to surface scattering. c) The non-linear dependency of the extinction cross section peak intensity on volume (V) due to size-dependent damping.

In order to model core-shell NRs, this procedure needs to be extended. The composition, radius and length of the shell are additional parameters that need to be considered. The polarizability of a coated spheroid is given by[30]

$$\alpha_{x,} = \frac{((\varepsilon_s - \varepsilon_m)(\varepsilon_s + (\varepsilon_c - \varepsilon_s)(L_c - fL_s)) + f\varepsilon_s(\varepsilon_c - \varepsilon_s))V}{(\varepsilon_s + (\varepsilon_c - \varepsilon_s)(L_c - fL_s))(\varepsilon_m + (\varepsilon_s - \varepsilon_m)L_s + fL_s\varepsilon_s(\varepsilon_c - \varepsilon_s))} \tag{2.29}$$

where ε_m is the dielectric constant of the medium, ε_c the dielectric function of the material in the core, ε_s the dielectric function of the material in the shell, L_c the shape factor of the core along the long axis, L_s the shape factor of the shell of the long axis and $f = V_c/V_s$ the ratio between core and shell volumes.

2.4   Modelling plasmon resonances with Mie-Gans theory

Now that we have described all the equations related to Mie-Gans theory for NRs it is possible to calculate the localized surface plasmon resonances. The interesting properties of the LSPRs that we can characterize are the resonance peak position and the width of the resonance peak. These properties can be tuned by a number of parameters, which will be discussed here.

2.4.1   Size

We have already shown that the damping factor of the dielectric function depends on size. For NPs with widths greater than 10 nm, the radiation damping term has to be taken into account as will become evident in chapter 3. When the size of the metal NP is comparable to or lower than the electron mean free path of the material electron scattering off of surfaces cannot be ignored. This electron-surface scattering broadens the resonance peak and reduces its intensity. We will include both radiative decay and electron-surface scattering for all further calculations in this chapter, with $\kappa = 6.2 \times 10^{-7}\,\mathrm{fs}^{-1}\mathrm{nm}^{-3}$ and $A = 0.3$. These values were determined in dark-field scattering experiments by Hu et al. for NRs of aspect ratio 3.[35] Figure 2.3 shows spectra calculated with shape-corrected Mie-Gans theory for Au spherocylinders with aspect ratio 3 but various sizes. Both the resonance wavelength and the peak intensity depend heavily on size. Dephasing due to surface scattering results in a broader resonance for the smaller size NPs. The resonance spectrum for the NP with a 4 nm radius is more broad than the spectrum for the 6 nm radius NP, for example. Also, radiation damping broadens the plasmon resonances for larger NPs. For example, the plasmon resonance for the 12 nm radius NP is broadened compared to the spectrum of the 10 nm NP. This means there is an optimal radius for the NPs, for which the combination of bulk damping, surface-scattering and radiative decay is minimized. This will be looked at in chapter 3. Due to the use of small NPs in our experiments, we do not focus on calculating extinction spectra for larger NPs. To study these sort of NPs, the Modified Long Wavelength Approximation or numeric solving of Maxwell's equations are good options.

2.4.2   Dielectric constant of the medium

Next we investigate the influence of the dielectric constant of the medium ε_m, which is the square of the refractive index n. The dependence of the surrounding medium on the surface plasmon resonance can be understood by studying the plasmon resonance condition. The plasmon resonance condition says that the denominator of the polarizability in Equation 2.19 approaches zero at the plasmon resonance. For spherical NPs this condition is

$$Re[\varepsilon(\omega)] + 2\varepsilon_m = 0 \tag{2.30}$$

where $Re[\varepsilon(\omega)]$ is the real part of the dielectric function and ε_m the dielectric constant of the surrounding medium. It has been shown that the plasmon peak red-shifts roughly linearly with the refractive index of the surrounding medium for
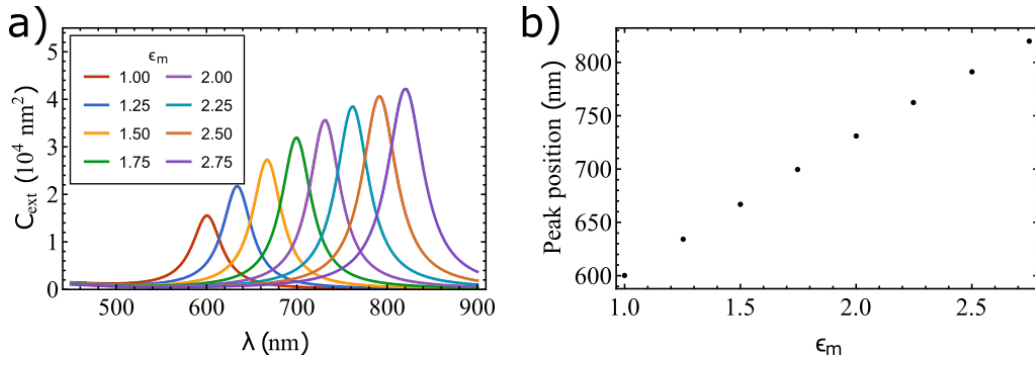
Figure 2.4: a) Extinction cross sections (C_{ext}) calculated with Mie-Gans theory for Au NRs of aspect ratio (AR) 3 and a radius (r) of 10 nm in media of various dielectric constants (ε_m). b) Peak position shift with increasing dielectric constant of the medium ε_m.

spherical NPs[53,55]

$$\lambda = \lambda_{p,b}\sqrt{2n_m^2+1} \approx \sqrt{3}\lambda_{p,b}(1+\frac{1}{3}(n_m-1)) \tag{2.31}$$

where λ is the wavelength of the localized surface plasmon resonance, $\lambda_{p,b}$ the wavelength of the bulk plasmon and n_m the refractive index of the surrounding medium. It has also been shown that the plasmon resonance of a non-spherical NP also shows a linear dependence on the refractive index of the surrounding medium.[53] The resonance condition for rod-like NPs can also be extracted from the equation for the polarizability (Eq. 2.19) and is given by

$$\varepsilon_m + L_x(\varepsilon(\omega)-\varepsilon_m) = 0 \tag{2.32}$$

The wavevector of the light in the medium k and the polarizability α of a metal NP, which are both used to calculate the plasmon resonance, depend on the dielectric constant of the surrounding medium in our Mie-Gans calculations. We present the calculated dependence of the LSPR of Au NRs with aspect ratio 3 and a radius of 10 nm on the medium in Figure 2.4. A significant red-shift is observed if the dielectric constant of the medium is increased. The resonance wavelength increases linearly with the dielectric constant of the medium ε_m. The intensity of the longitudinal plasmon resonance also increases for higher dielectric constant of the medium.

Often, metal NPs are surrounded by ligands or coating like silica for stability. In our experiments in chapter 5, a meso-porous silica coating is used. This coating has an impact on the dielectric constant of the medium and therefore on the plasmon resonance of the metal NP. For calculations, the coating should be taken into account when using the dielectric constant of the medium ε_m. Since the dielectric constant is related to the square of the refractive index, the dielectric constant of the medium for a coated metal NP in a medium can be calculated with effective medium theory and is given by

$$\varepsilon_m = n_{coat}^2(1-porosity)+n_m^2 \times porosity \tag{2.33}$$

where n_{coat} is the refractive index of the coating, n_m the refractive index of the medium and the porosity lies between 0 and 1.

2.4.3   Shape

For non-spherical NPs the plasmon resonance depends on the polarization of the incident light. This is because the electrons are displaced perpendicular to the polarization of the light, because the electric field component of the light is perpendicular to the polarization direction. In the following NRs are focused on due to their significance in this work. As mentioned before, NRs have two different plasmon resonances, due to the shape of the NP. If the electrons are displaced along the long axis, the plasmon resonance is called the longitudinal plasmon resonance. Perpendicular to this longer axis a transverse plasmon resonance can be observed. Along the long axis, the NR has the highest polarizability, so the longi-tudinal LSPR is more intense than its transverse counterpart and the LSPR of a sphere of the same volume. We therefore focus on the longitudinal LSPR. The most interesting parameter for rod-like NPs is the aspect ratio $AR = L/D$. In Figure 2.5 the extinction spectra for Au NRs with different aspect ratios are plotted. The NRs are in water and all have a constant volume $V = 1.68 \times 10^4$ nm^3. When the aspect ratio increases, so does the peak intensity (Figure 2.6). This is because the NR has a higher polarizability at higher aspect ratio which increases the extinction cross section. By looking at the equation for the polarizability (Eq. 2.19) it can be seen that the lower the shape factor L_x, the higher the polarizability. The shape factor decreases for higher aspect ratios, meaning a higher aspect ratio increases both the real and imaginary part of the polarizability. Since the absolute value and the imaginary part of the polarizability increase, so will the scattering and absorption cross sections (Eq. 2.26 and 2.27) and with that the extinction cross section (Eq. 2.28). The intensity of the peak increases dramatically with aspect ratio in the low aspect ratio regime, due to an increased polarizability. However, at higher aspect ratios the intensity differences are not high. This is due to extra damping at higher wavelengths, because
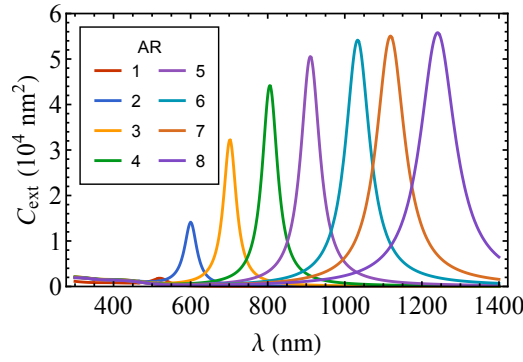
Figure 2.5: Extinction cross sections (C_{ext}) calculated with Mie-Gans theory for Au NRs of different aspect ratios (AR) in water for constant volumes $V = 1.68 \times 10^4 \, \text{nm}^3$.
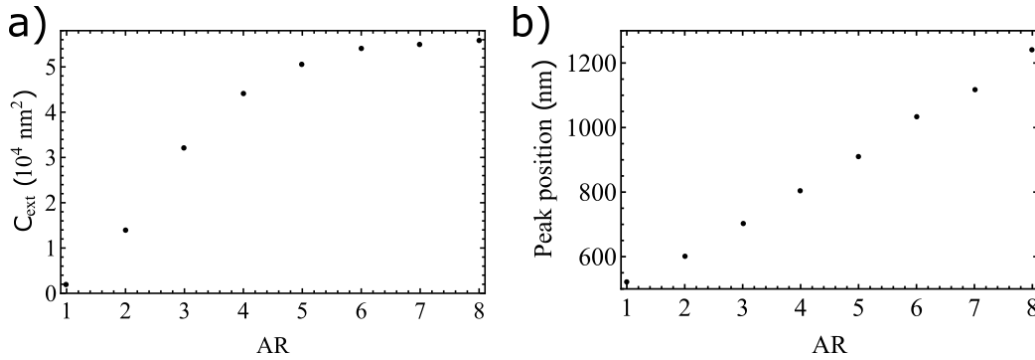

Figure 2.6: The influence of aspect ratio (AR) on a) peak intensity and b) peak position, calculated with Mie-Gans theory for the same NRs as used in Figure 2.5.

there the imaginary part of the dielectric function for Au increases. Electrons experience more scattering in the low energy regime, which counters the effect of the higher polarizability. The LSPR also red-shifts when the aspect ratio is increased (Figure 2.6). This shift to larger wavelength occurs due to the larger charge separation and therefore a reduction in the eigenfrequency of the restoring force. The peak position in the wavelength regime increases linearly with aspect ratio, as shown in Figure 2.5b).

The aspect ratio is not the only shape related influence on the plasmon resonance. Bansal and Verma have shown that NPs with sharp edges have better plasmonic properties.[56] Incident light will cause a larger density of electrons at the sharp corners and edges which induces strong electric field enhancements and increases the extinction cross section.

It has been shown that the plasmonic properties depend strongly on the shape of the end caps of NRs.[57] This is visualized in Figure 2.7 using the shape factors of Prescott & Mulvaney.[51] The eccentricity is a measure for the curvature of the end cap. Here we used a weighted average of cylindrical and spherocylindrical shape factors from Prescott and Mulvaney, where the eccentricity is the normalized weight of the spherocylindrical shape factor. An eccentricity of 0 thus represents a cylindrical NR, while an eccentricity of 1 is a spherocylindrical NR. A flatter end cap means a red-shifted resonance wavelength and a slightly higher peak intensity, due to the slightly higher polarizability.
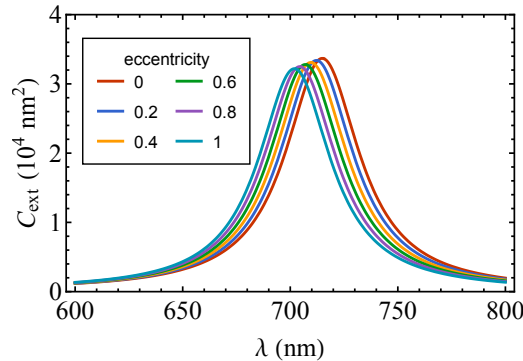

Figure 2.7: Extinction cross sections (C_{ext}) calculated with Mie-Gans theory for Au NRs of aspect ratio (AR) 3 and radii (r) of 10 nm in water with different end cap curvatures.
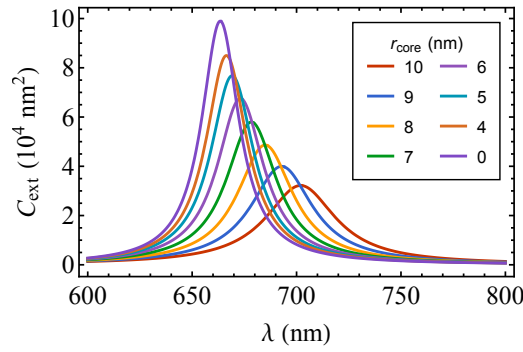
Figure 2.8: Extinction cross sections (C_{ext}) calculated with Mie-Gans theory for spherocylindrical Au-Ag core-shell NRs with both core and shell having an aspect ratio 3. The radius of the total NP is 10 nm and the radius of the core (r_{core}) varies. The NRs are dispersed in water ($\varepsilon_m = 1.77$). The Au core is varied from 4 to 10 nm (Au NR). The pure Ag NR is also shown.

2.4.4   Core-shell particles

The LSPR can also be tuned by the composition of the NP. Firstly, we look at the influence of a Ag shell on the optical response of Au-Ag core-shell NRs. Figure 2.8 shows the extinction cross sections of core-shell NRs of equal total volume. We see that with decreasing core size, i.e. increasing Ag shell thickness, the resonance wavelength blue-shifts. Since the plasmon resonance of Ag NPs is blue-shifted compared to Au NPs of the same shape, this is expected. NPs with more Ag also have a higher extinction intensity. This is also expected, because Ag has a lower imaginary part of the dielectric function than Au and thus exhibits less bulk damping. However, it should be noted that Mie-Gans calculations do not take into account that electrons may scatter off the interface between Au and Ag. Liu et al. conducted dark-field scattering measurements and found that the plasmon resonance of core-shell NRs was broadened compared to simulated spectra, which they attributed to interface scattering.[33]

2.4.5   Alloyed particles

In section 2.2.3 we looked at the dielectric functions of bulk Au-Ag alloys (Figure 2.2). From the imaginary part of the dielectric functions we deduced that there are two different regimes. At energies below 1.8 eV all compositions of Au-Ag alloys have a higher imaginary part of the dielectric function than pure Au and thus more damping, whereas at higher energies the alloy NPs perform better. Thus for alloy NRs with a plasmon resonance at an energy below 1.8 eV, we expect the plasmon resonance of any alloy NP to be less intense than the plasmon resonance of a Au NP with the same shape and size, even though an alloyed NP consists of more Ag, which is the better plasmonic material. By modelling spheres and NRs with different alloy compositions and different aspect ratios, we can probe a large energy regime and compare the optical performance.

Extinction cross sections for spherical NPs of different Au-Ag alloy compositions calculated by using the dielectric function of Rioux et al. are shown in Figure 2.9. The plasmon resonance blue-shifts if the alloyed NP contains a higher Ag fraction. This is expected as the plasmon resonance of a Ag NP is blue-shifted compared to an identical Au NP. The intensity of the plasmon resonance of alloyed spheres with more Ag than Au is greater than the plasmon resonance of a Au sphere. This is mainly due to the shift of the onset of interband transitions, which suppresses interband damping for
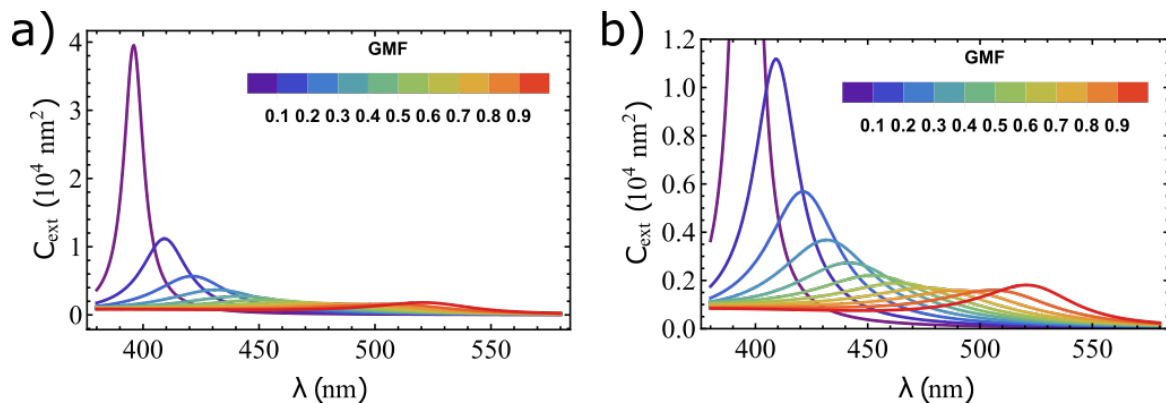

Figure 2.9: a) Extinction cross sections (C_{ext}) calculated with Mie-Gans theory for Au-Ag alloy spheres of different composition. The spheres have a constant volume $V = 1.68 \times 10^4$ nm^3 and are in water ($\varepsilon_m = 1.77$). b) Same calculations as in a), but with a differently scaled vertical axis so the plasmon resonances of the alloy compositions are clearly distinguishable. The composition of the alloy is characterized with the gold molar fraction (GMF). A GMF of 1 is pure gold (red) and a GMF of 0 is pure silver (purple).

Figure 2.10: Extinction cross sections (C_{ext}) calculated with Mie-Gans theory for Au-Ag alloy NRs of different composition. The four figures show plasmon resonances for NRs for aspect ratios (*AR*s) a) 1.5, b) 2, c) 3 and d) 4. All the NRs have a constant volume $V = 1.68 \times 10^4$ nm^3 and are dispersed in water ($\varepsilon_m = 1.77$). The composition of the alloy is characterized with the gold molar fraction (GMF). A GMF of 1 is pure gold (red) and a GMF of 0 is pure silver (purple).
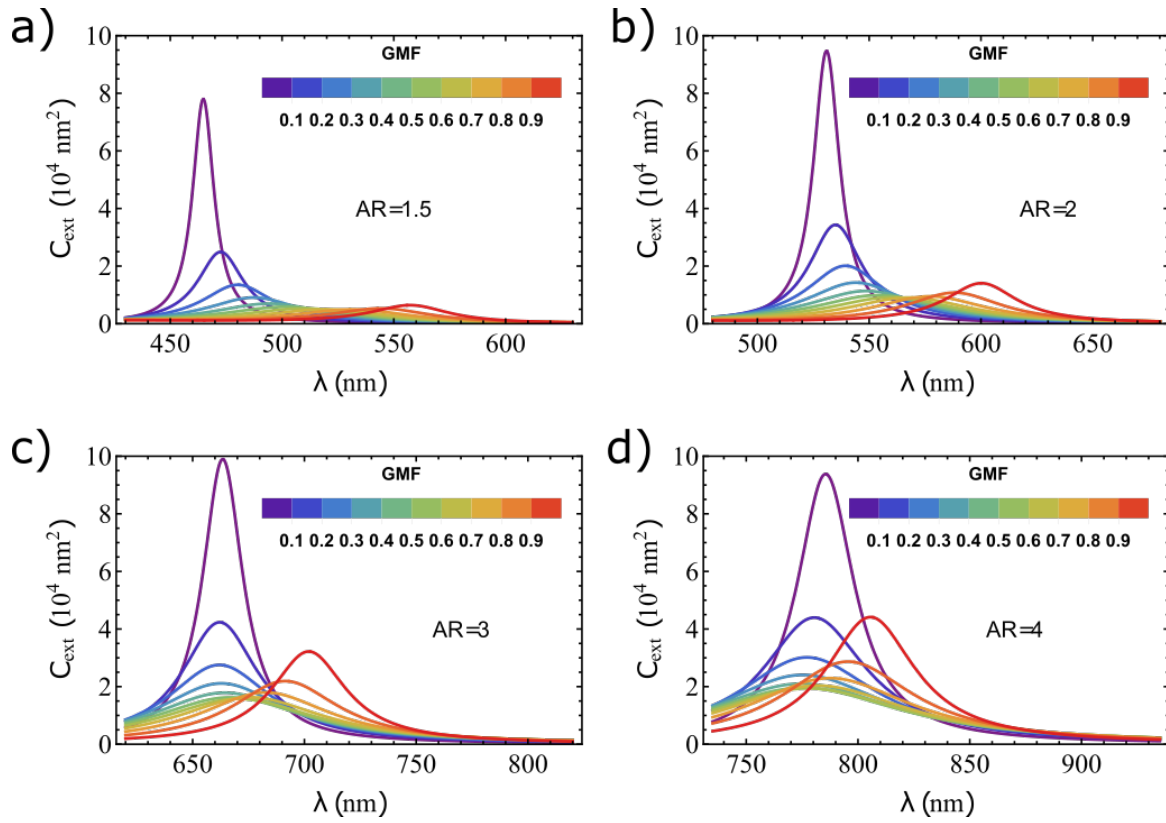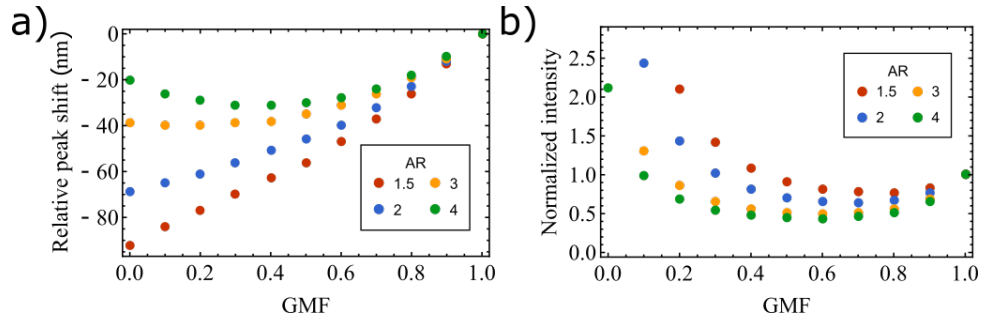
NPs with a higher Ag fraction.

Figure 2.11: a) Relative peak position shift of alloyed NRs of various composition compared to the peak position of a Au NR of the same aspect ratio (*AR*). b) Intensity of alloyed NRs of various compositions normalized on the intensity of a Au NR with the same *AR*.

The situation is different for alloyed NRs since the plasmon resonances shift towards energies below 1.8 eV. The plasmon resonances for alloyed NRs of 4 different ARs are shown in Figure 2.10. The plasmon resonance for NRs with a lower Au molar fraction generally shifts to the blue part of the spectrum (Figure 2.11a). However, for aspect ratio 3 and 4 the relative shift of the plasmon resonance as a function of alloy compositions compared to the pure Au composition of equal aspect ratio is less than for aspect ratio 1.5 and 2. For an aspect ratio of 4, the pure Ag composition is even red-shifted compared to alloy compositions with a GMF lower than 0.3, as seen in Figure 2.11a). This is counter-intuitive and may be caused due to errors in the ellipsometry data, as it is not observed when using the dielectric function of Peña-Rodríguez et al.[15] for alloyed NRs of aspect ratio 4 (Figure 2.12).

Furthermore, the alloyed NRs generally have a worse plasmonic performance than Au NRs, except for alloys with high Ag fractions. From comparing the extinction intensities of NPs with an alloy composition with pure Au NPs it can be seen that the plasmonic performance of the alloyed compositions gets relatively worse for higher aspect ratios (Figure 2.11b), as expected from the dielectric functions (Figure 2.2).

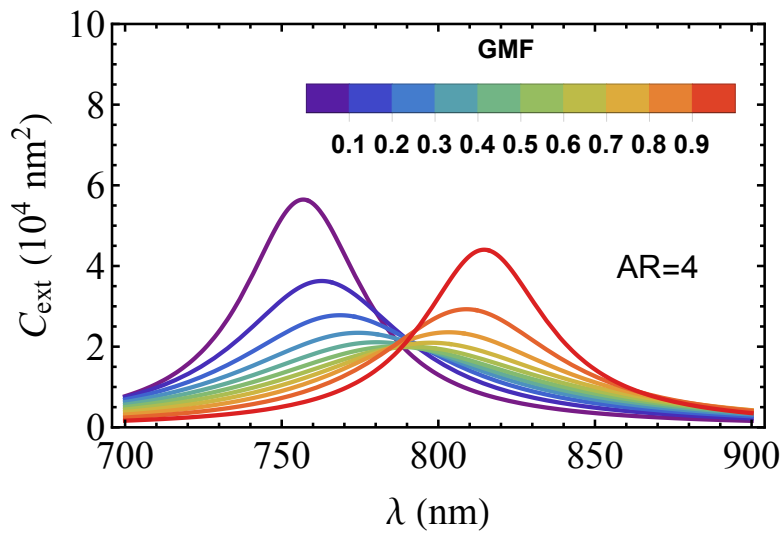Figure 2.12: Extinction cross sections (C_{ext}) calculated with Mie-Gans theory for Au-Ag alloy NRs of aspect ratio (*AR*) 4 of different composition with the model of Peña-Rodríguez et al.[15] All parameters are the same as for the alloyed NRs in Figure 2.10d). The composition of the alloy is characterized with the gold molar fraction (GMF). A GMF of 1 is pure gold (red) and a GMF of 0 is pure silver (purple).

3 Radiation damping for rods and spheres of various metals

3.1 Introduction

For most applications an intense and sharp plasmon resonance is crucial, which generally coincides with strong field enhancements. The strength of the resonance and the homogeneous broadening of the line width for single NPs is strongly influenced by the dephasing of the collective electron oscillations, which contributes to a phenomenon termed plasmon damping. Because of this, several recent studies focused on the line width of plasmonic resonances for differently shaped NPs.[28, 34–36, 38, 40, 44, 54, 58–62]

Both non-radiative and radiative decay mechanisms contribute to plasmon damping. The former involves, amongst other mechanisms, interband and intraband excitations which are determined by the inherent nature of the metal and are reflected in its bulk dielectric function. The intraband contributions are mainly related to electron scattering by phonons, defects or other electrons. At energies for which interband transitions occur, the electrons can also scatter into empty levels of the conduction band which is called interband or Landau damping. For small NPs with sizes below the electron mean free path (e.g. about 20 nm in Au) electron surface scattering needs to be taken into account as well which leads to additional non-radiative damping Γ_s. An effective mean free path l_{eff} can be defined and the electron-surface scattering contribution to the overall damping is generally included as $\Gamma_s = A v_f / l_{eff}$ where v_f is the Fermi velocity and A indicates the strength of the electron-surface scattering. A general expression for arbitrarily shaped NPs was recently derived yielding $l_{eff} = 4V/S$ where V and S are the volume and surface area of the NP, respectively.[32]

Radiation damping occurs due to photon emission of the radiative dipole and is proportional to the volume V of the NP. For example, with Au NRs it was shown that it matters for sizes above 20 nm.[34] Γ_r is commonly described as $\Gamma_r = 2\hbar\kappa V$ where κ indicates the strength of radiation damping.[28, 34, 35, 60] It is proposed that radiation damping depends on resonance energy and shape,[44, 52, 62–65] dependencies that are not yet well understood.

Au and Ag are normally model systems for plasmon resonances due to low intrinsic damping and because they do not exhibit interband transitions in the energy regions where plasmon resonances occur. Recently, interest has grown in non-precious metals like Cu and Al, mainly due to their high abundance and because they can exhibit plasmon resonances in different energy regions, e.g. in the UV for Al. In these metals interband transitions can overlap with the plasmon resonance and it was shown theoretically and experimentally that a double-peaked resonance can appear when the plasmon resonance comes close to an interband transition,[66, 67] e.g. about 1.5 eV in Al and 2.1 eV in Cu. The relative contributions of damping mechanisms can also be quite different compared to Au and Ag.[54] For example, for Al it was suggested that the radiative line width dominates the overall damping with only a small relative contribution from non-radiative processes, whereas for Ag non-radiative processes are far more important compared to radiative ones.[59]

This shows that it is important to learn more about radiative damping and a more quantitative description of it could help to understand damping over a large energy range. Whereas bulk and surface damping are quantitatively more studied,[34–36, 38] this is not the case for radiation damping, especially not for a large variety of metals. A few measurements on Au and Ag NPs were performed to quantitatively obtain κ but different values were reported. For instance, Sönnichsen et al.[28] found $\kappa = 4 \times 10^{-7}\,\text{fs}^{-1}\text{nm}^{-3}$ for spherical Au NPs and Novo et al.[34] extracted $\kappa = 7 \times 10^{-7}\,\text{fs}^{-1}\text{nm}^{-3}$ for Au NRs of aspect ratios 2 to 4. For Ag nanoprisms $\kappa = 12 \times 10^{-7}\,\text{fs}^{-1}\text{nm}^{-3}$ was obtained.[44] However, experimental studies are often limited by other influences such as surface scattering and chemical damping and have so far only been conducted for narrow energy ranges.[28, 34, 35, 44] Numerical calculations can help to probe a large parameter space. Numerical methods like finite-difference time-domain (FDTD) calculations are suitable since they intrinsically include radiation damping but not damping due to surface effects.[61] We therefore performed FDTD calculations on nanospheres and nanorods for a broad range of parameters and different metals (Au, Ag, Cu and Al) and extracted $\kappa(\omega)$. Changing the resonance energy by varying the shape of the NP and not as it was recently done by changing its volume,[44, 54] allows us to decouple the strong volume dependence of radiation damping from its other dependencies. We found that κ scales with the inverse of the imaginary part of the metal dielectric function and linearly with the surrounding dielectric constant and that an underlying material constant κ_{metal} can be ascribed to each metal as the corresponding proportionality constant. Our approach can reproduce the different κ measured so far and gives a more intuitive description of radiation damping. It can furthermore help to explain luminescence in Au NPs, a process which is mainly governed by the radiative decay of localized surface plasmons.[68–71] We furthermore show that by looking at the sum of the obtained radiation damping Γ_r, bulk damping Γ_b and surface scattering effects we can predict optimal radii for Au NRs of different aspect ratios, i.e. for which size the overall damping is the least. Our approach can be extended to many metals and shapes and helps to choose the right metal and NP size for which the least (or most) damping is obtained for each desired application.

3.2 Methods

3.2.1 Finite-difference time-domain (FDTD) calculations

In order to systematically study the radiation damping behaviour we performed various FDTD calculations of NPs with spherical or spherocylindrical shapes, motivated by our synthesis results as described in section 5.3.1, and extracted the corresponding line widths. By varying the sizes and aspect ratios (AR) of the NRs, LSPRs and thus κ over a large energy range could be probed. The calculations were carried out with the software package Lumerical FDTD Solutions 8.11. We primarily used the by McPeak and co-workers measured dielectric functions for Au, Ag, Cu and Al[17] which are plotted in Figure 3.1. A total field - scattered field source was employed to simulate a propagating plane wave interacting with the nanostructures. Spheres and rods ranging from aspect ratio 2 to 6 were used to investigate the radiation damping. The NRs were modelled as spherocylinder, which are cylinders with hemispherical endcaps. Only the longitudinal surface plasmon resonance was calculated by setting the polarization parallel to the long axis of the NRs. The dielectric function of the used material was imported as tabulated data[14,17,18] and fitted with a multi-coefficient model to obtain a continuous dielectric function. The NPs were always placed at the origin of the simulation box. The simulation box was $0.5 \times 0.5 \times 1\,\mu m$, with the extended side parallel to the long axis of the NRs. Perfectly matched layers (PMLs) surrounded the simulation box stretching $0.5\,\mu m$ to all sides. A three-dimensional non-uniform mesh was used for the volume around the nanostructure. The mesh grid size depended on the size of the nanostructure. For the smallest nanostructures ($r = 5\,nm$) a mesh of $0.2\,nm$ was used. For the largest ($r = 20\,nm$) a mesh of $0.6\,nm$ was used. Simulations with silver generally required a smaller mesh than simulations with other metals due to its small real refractive index. This smaller mesh was determined by decreasing the mesh and running the simulation until the resulting spectrum was the same as for the mesh before. The total field - scattered field source was placed on the boundary of the mesh volume. The simulations were normally run for 100 femtoseconds of simulation time. The simulation was automatically stopped when the field strength decayed to a fraction (10^{-5}) of the peak field intensity. If the simulation result was unreliable a longer simulation time of 300 femtoseconds was used. Frequency-domain field monitors were employed to record the power going through them. By using six 2D plane monitors a box was created, where the power was recorded going through all six planes of that monitor box. One of these monitor boxes was placed in between the plane wave source and the nanoparticle. This was used to calculate the absorption cross section. A second monitor box was placed outside the plane wave source, encapsulating both the source and the particle. This box was used to calculate the scattering cross section.

To determine the extinction cross section of the particles, both the absorption and scattering cross sections were calculated. To calculate these the amount of power transmitted through the monitor box enclosing the light source was recorded, whereby the transmitted power at a certain frequency is given by $\frac{1}{2}\int Re[\vec{P}(f)^{monitor}]\cdot d\vec{S}$, where $\vec{P}(f)$ is the Poynting vector and $d\vec{S}$ an infinitesimal surface area. The scattering and absorption cross sections are equal to the power transmitted through the monitor divided by the irradiance of the source.

$$C(f) = \frac{\frac{1}{2}\int Re[\vec{P}(f)^{monitor}]\cdot d\vec{S}}{\frac{1}{2}\int Re[\vec{P}(f)^{source}]\cdot d\vec{S}} \times A_{source} \tag{3.1}$$

where A_{source} is the total area of the source and C the scattering or absorption cross section, depending on the placement of the monitors. The absorption cross section was calculated similarly by recording the total power dissipated in a small volume surrounding the NP and dividing it by the incident light irradiance. The extinction spectrum follows from the sum of the absorption and scattering spectra. The spectra were generated via a parametric sweep containing around 200 frequency points.

Figure 3.2 shows calculated extinction spectra obtained for the four metals assuming a spherocylindrical shape with $AR = 3$ for four different volumes, i.e. radii of $r = 5, 10, 15, 20\,nm$. The dielectric environment was assumed to be water with a dielectric constant of $\varepsilon_m = 1.77$, which was taken to be independent of energy. For all four metals the spectra redshift with increasing volume due to retardation effects and increase in intensity since the extinction cross section increases with NP volume.[72]

3.2.2 Lorentzian fitting

We fitted the calculated extinction spectra with a Lorentzian function[39,58,60,73]

$$C_{ext} = \Xi \frac{\Gamma/2\pi}{(\omega - \omega_R)^2 + (\Gamma/2)^2} \tag{3.2}$$

where ω_R is the resonance energy and Ξ the integrated oscillator strength, yields the line width Γ. Example fits for the Au spectra are shown as dashed lines in Figure 3.3. The line width can be extracted from these fits. However, some spectra do not have a proper Lorentzian shape, due to absorption features, mainly from interband transitions. Examples of such spectra are shown in Figure 3.4a) for Au NPs and in Figure 3.4b) for Al NRs. This means those spectra cannot be reliably fitted with a Lorentzian. For the spherical Au NPs, the interband features prevent reliable Lorentzian fitting
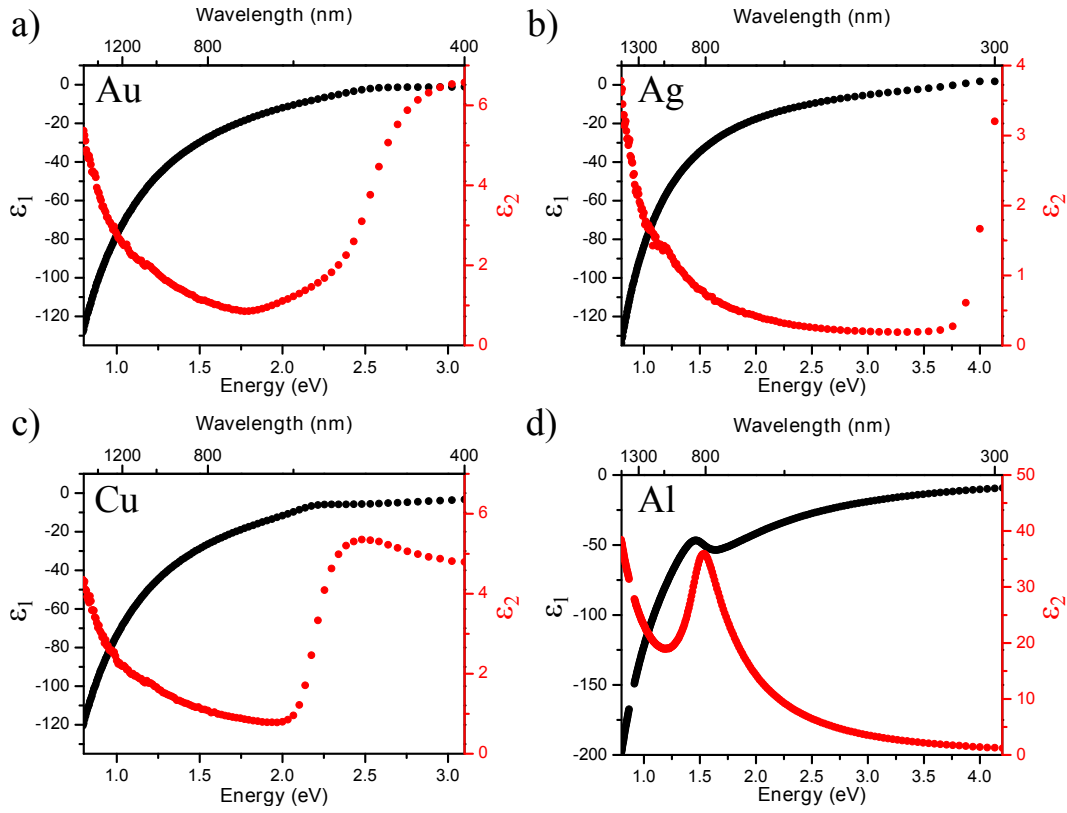
Figure 3.1: Real (ε_1) and imaginary (ε_2) part of the dielectric functions for a) Au, b) Ag, c) Cu and d) Al measured by McPeak et al.[17]
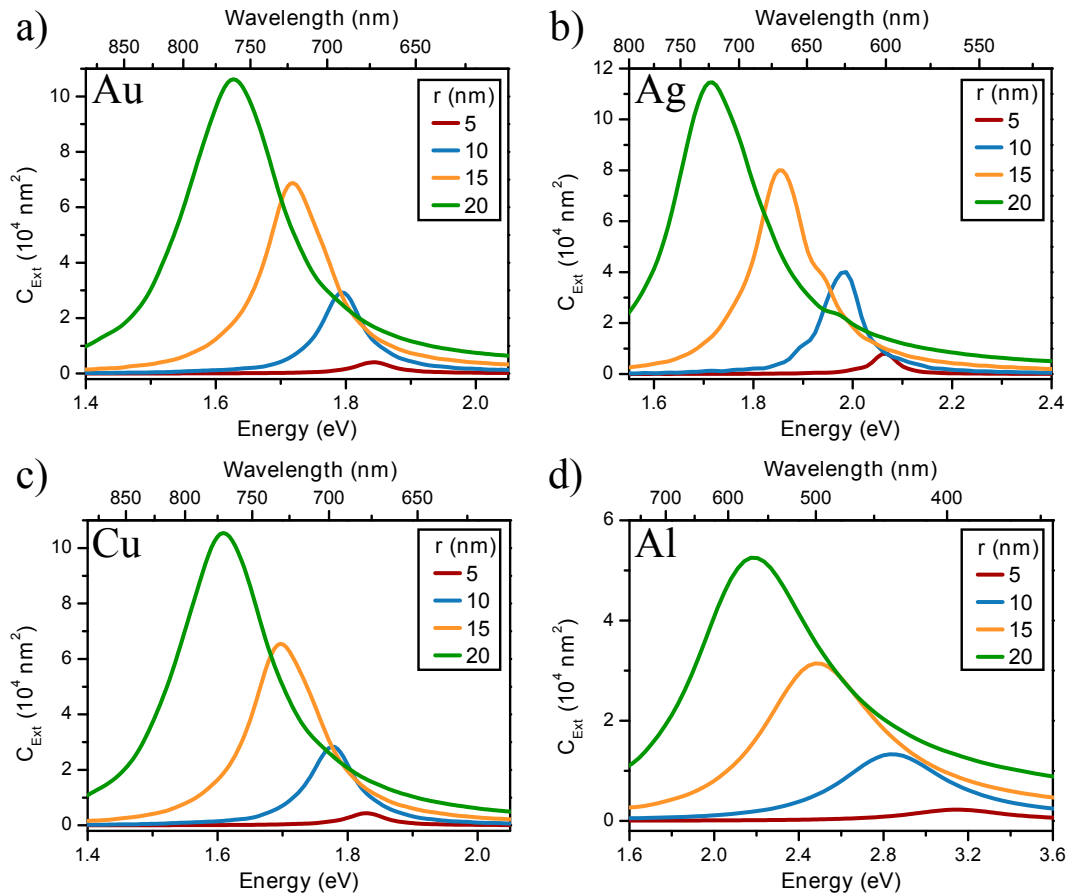

Figure 3.2: Extinction spectra obtained from FDTD simulations for NRs with aspect ratio (AR) 3 and different radii (r) in water for a) Au, b) Ag, c) Cu and d) Al NPs. The red-shifts of the LSPRs with increasing volumes are due to retardation effects.
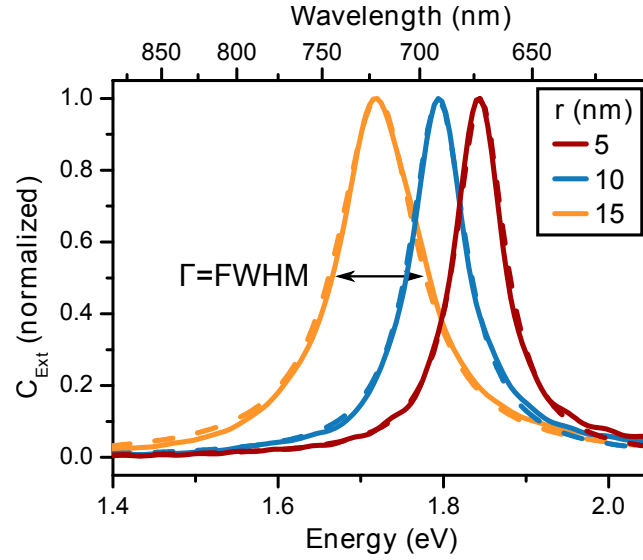
Figure 3.3: Typical Lorentzian fits (dashed) of FDTD extinction spectra (full lines).
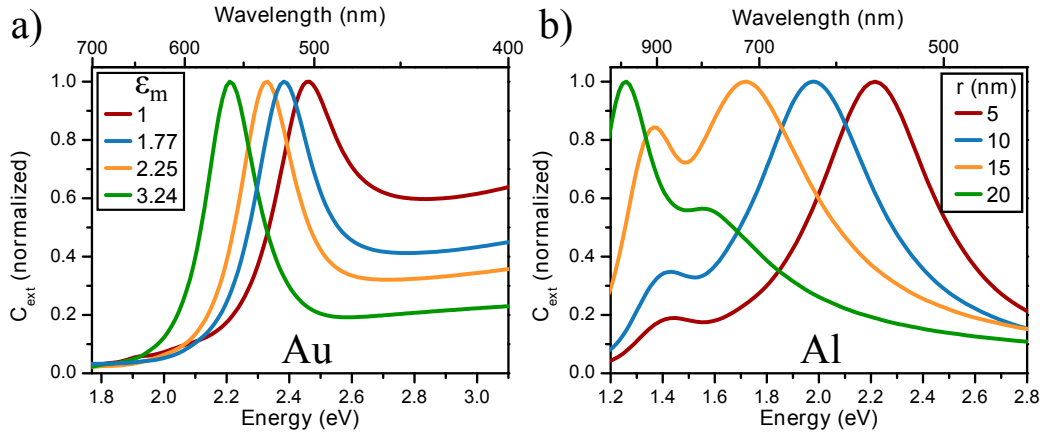

Figure 3.4: Examples of spectra that could not be reliably fitted. a) Normalized FDTD calculated extinction cross sections (C_{ext}) for spherical Au NPs ($r = 15$ nm) in different media. The higher the resonance energy the more the spectra deviates from a Lorentzian shape. b) Normalized FDTD spectra for Al NRs ($AR = 5$) in water around the interband transition.

for $\varepsilon_m = 1$ and $\varepsilon_m = 1.77$. Similarly, for Cu spheres Lorentzian fitting for $\varepsilon_m = 1$ and $\varepsilon_m = 1.77$ was unreliable. For Al NRs with energies close to the interband transition (at 1.5 eV) the plasmon resonances did not exhibit a proper Lorentzian shape. The interband transition influences both the line width and the peak position of the spectra, making the fits and its extracted parameters unreliable. Since the Al spectra were very broad, the interband transition influenced many spectra for NRs of various aspect ratio. For that reason the analysis for Al includes less data points. The interband transition for Ag lies outside the probed energy regime and does not influence the spectra.

3.3   Results & Discussion

3.3.1   Extracting bulk damping and radiation damping parameters

We repeated the procedure described in the methods section for different aspect ratios ranging from 1 to 6 and 3 to 4 different volumes per aspect ratio. A large energy range where plasmon resonances occur could be covered. Furthermore, the red-shift for the included volumes per aspect ratio was found to be relatively small (< 0.3 eV for Au, Ag and Cu) to make sure that the same wavelength range in the dielectric function is probed. For that reason not all 4 volumes corresponding to r = 5, 10, 15, 20 nm were always included in the analysis. Still, at least 3 volumes were included to get a reliable fit. For Al, where the red-shift is larger than for the other metals (Figure 3.2d), this therefore leads to a bigger shift in the energy range (< 0.75 eV). The obtained Γ values for $\varepsilon_m = 1.77$ are shown as data points in Figure 3.5.

In order to extract $\kappa(\omega)$ the line widths of the spectra of particles with equal aspect ratio but different volumes were then fitted using $\Gamma = \Gamma_b + 2\hbar\kappa V$ whereby Γ_b and κ were used as fitting parameters. The fits are shown as solid lines in Figure 3.5. The bulk damping Γ_b will influence the found κ. Therefore it is necessary to confirm that the extracted values of Γ_b are what we expect them to be. In Figure 3.6, we see that for Au and Cu Γ_b is constant up to the onset of interband
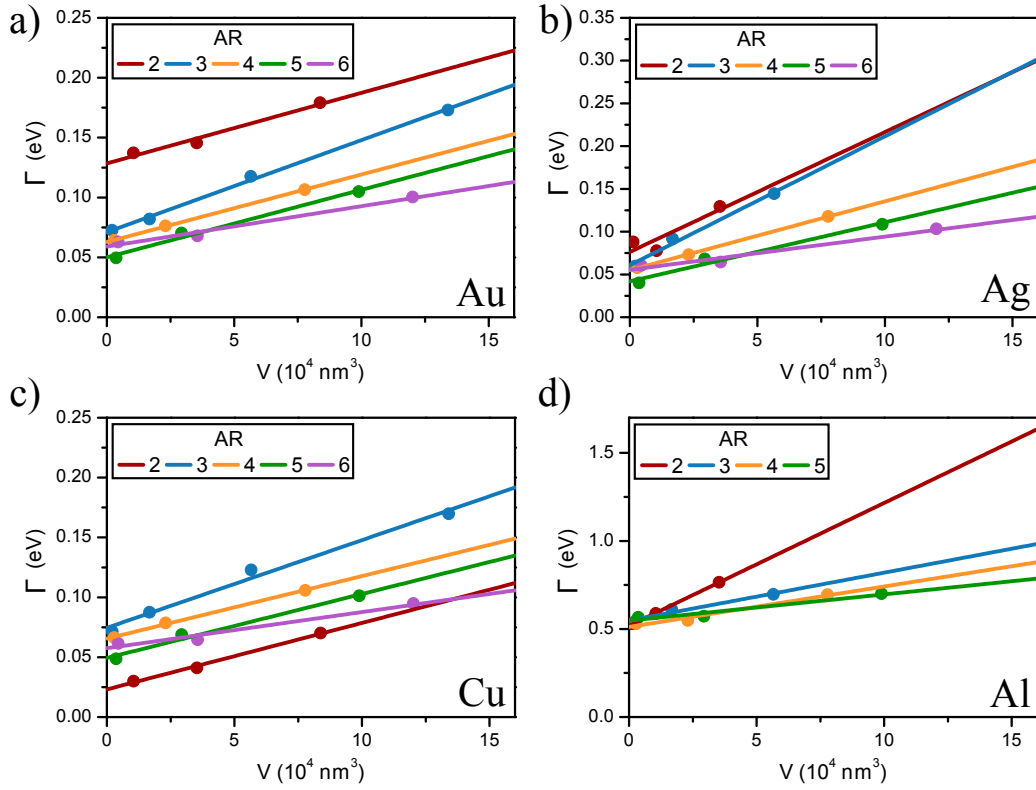
Figure 3.5: Dependence of the total damping Γ on volume (points) for a) Au, b) Ag, c) Cu and d) Al NRs of different aspect ratios. The solid lines are linear fits of the equation $\Gamma = \Gamma_b + 2\hbar\kappa V$. The total damping can thus be described as a sum of the bulk damping and the volume dependent radiation damping.
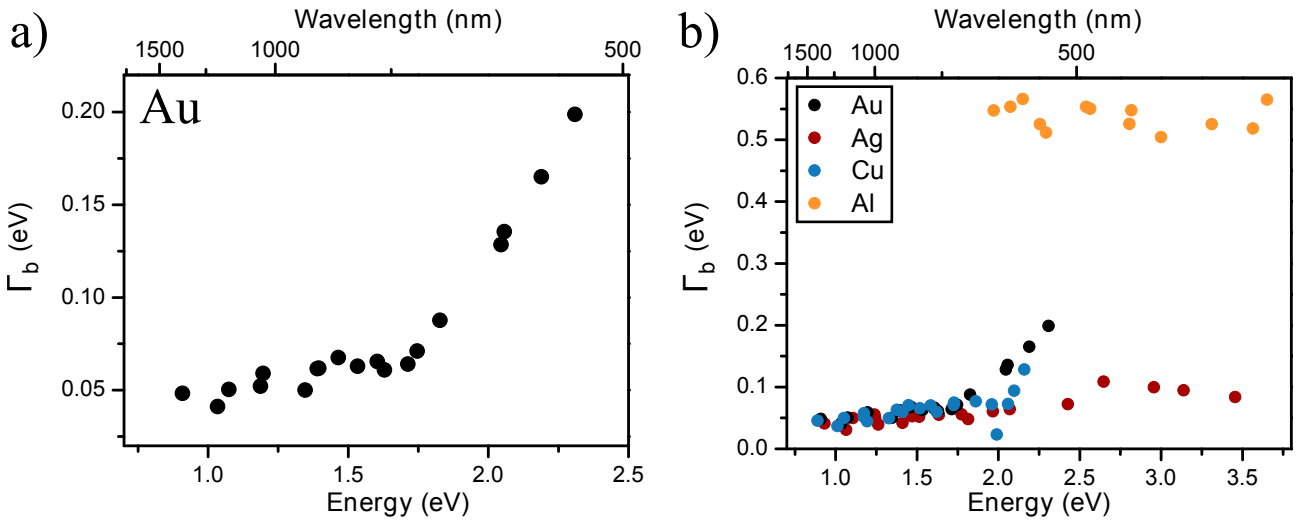

Figure 3.6: Values found for the fit parameter for the bulk damping Γ_b as function of resonance energy. a) Energy dependence of the extracted bulk damping for Au. b) Extracted bulk damping as function of energy for all four metals that were analysed.

transitions as below that range only energy-independent intraband contributions play a role.[54] At the onset of interband transitions Γ_b increases linearly which is in agreement with earlier work.[54] For Ag, Γ_b is constant over most of the energy range probed, which is below the onset of the interband transition in Ag, and only slightly increases at higher energies. In order to check if the bulk damping shows reasonable values for low energies, the used dielectric functions at low energies were fitted to a Drude model $\varepsilon(\omega) = \varepsilon_\infty - \omega_p^2/(\omega^2 + i\gamma\omega)$, where ε_∞, ω_p and γ are fit parameters. The constant values for Au, Ag and Cu at lower energies fit well to the obtained bulk damping constants γ from the Drude model which yields $\gamma_{Au} = 0.03$ eV, $\gamma_{Ag} = 0.02$ eV and $\gamma_{Cu} = 0.03$ eV. It is also in good agreement with Blaber et al. who found $\gamma_{Au} = 0.023$ eV and $\gamma_{Ag} = 0.018$ eV.[48] These values are also close to $\gamma_{Au} = 0.027$ eV, $\gamma_{Ag} = 0.018$ eV and $\gamma_{Cu} = 0.009$ eV found by Ordal and coworkers.[47] For Al, energy-independent Γ_b values around 0.55 eV were obtained from the Γ fits which is higher than $\gamma_{Al} = 0.17$ eV fitted by a Drude model. The reason for this deviation probably lies in the residual influence of the interband transition at around 1.5 eV (see Figure 3.1d). In literature, bulk damping parameters for Al vary significantly.

Blaber et al.[48] found $\gamma_{Al} = 0.598$, while Ordal et al.[47] found $\gamma_{Al} = 0.082$ and Zeman et al.[46] found $\gamma_{Al} = 0.129$. Thus, all Γ_b values agree reasonably well with literature values,[45–48] however, there are significant variations in bulk damping values reported for Al dielectric functions measured by various authors. The values for κ that were found are therefore reasonable.
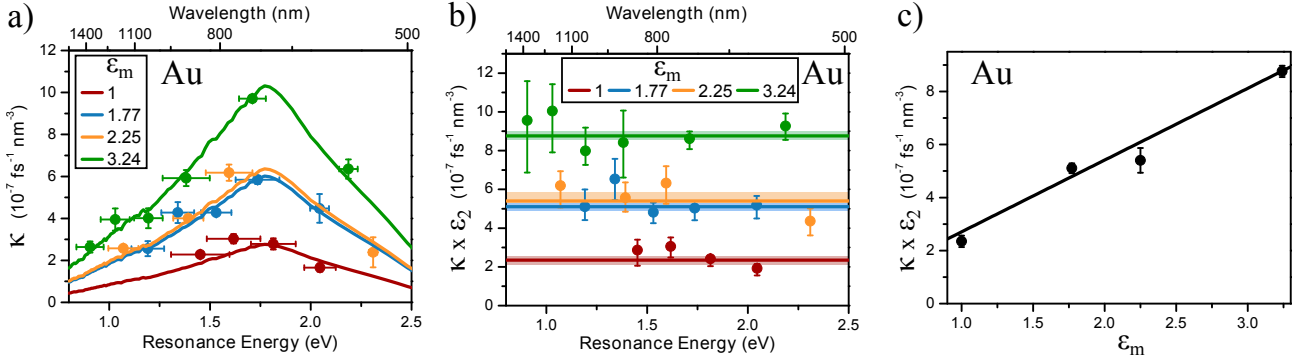

Figure 3.7: The procedure followed to determine κ dependencies. a) The radiation damping constant κ obtained for Au NPs as a function of energy for different dielectric media. The solid curves are least-square fits to the data points of $\kappa = B/\varepsilon_2^{Au}$. b) Fitting parameter $B = \kappa \times \varepsilon_2^{Au}$ for the four different dielectric media. c) $B = \kappa \times \varepsilon_2^{Au}$ as a function of ε_m. The solid line is a linear fit to $B = \kappa \times \varepsilon_2^{Au} = \kappa_{metal} \times \varepsilon_m$ yielding $\kappa_{metal} = (2.71 \pm 0.08)10^{-7} fs^{-1} nm^{-3}$ as a fitting parameter.

3.3.2   Radiation damping of plasmon resonances in Au nanoparticles

The κ values found from fits for $\Gamma = \Gamma_b + 2\hbar\kappa V$ for Au for all aspect ratios are plotted in Figure 3.7a) as a function of the resonance energy. The resonance energy for a certain aspect ratio is taken as the average of the LSPR resonance energies corresponding to the particles of the same aspect ratio but different volumes. Since the strength of radiation damping depends on the surrounding medium[35] this procedure was repeated for several dielectric constants ε_m and the results are also shown in Figure 3.7a).

There are two main errors that influence the analysis of the data, which result in the vertical and horizontal errors for the points in Figure 3.7a). Firstly, there is the error in the fit parameter κ determined from the fits for $\Gamma = \Gamma_b + 2\hbar\kappa V$. Secondly, an error in ε_2 that comes from an error in ω_{res} (horizontal error in Figure 3.7a), because NPs with the same aspect ratio but different volumes red-shift relative to each other. The errors in κ and ε_2 are propagated in $B = \kappa \times \varepsilon_2$ via $\sigma_B = \sqrt{(\sigma_\kappa \varepsilon_2(\bar{\omega}))^2 + (\sigma_{\varepsilon_2(\omega)} \bar{\kappa})^2}$.

Theoretical descriptions showed that radiation damping increases with frequency.[52,62,63] However, for all media κ starts to decrease at resonance energies above 1.8 eV. This decrease can be attributed to the onset of interband damping which makes scattering of electrons into empty conduction bands more likely. Interband damping is thus a competing damping mechanism at higher resonance energies lessening radiation damping.

Competing damping mechanisms were also observed by Frank Hubenthal for elongated Au NPs at resonance energies between 1.45 and 2.15 eV.[36] Hubenthal found a weakening of electron-surface scattering for photon energies beyond the onset of interband transitions and proposed that damping occurs as a correlated effect and not as step by step dephasing.[36]

It can be seen from Figure 3.7a) that κ has a similar dependence on resonance energy for each chosen dielectric constant ε_m. Specifically, by comparing the dependence of $\kappa(\omega)$ to the imaginary part $\varepsilon_2(\omega)$ of the dielectric function of Au (Figure 3.1a) it seems that $\kappa(\omega)$ scales inversely with $\varepsilon_2(\omega)$. To verify that we performed least square fits of the form $\kappa(\omega) = B/\varepsilon_2(\omega)$ with B as a fitting constant. The fits are presented as solid lines in Figure 3.7a) and reproduce the κ dependence very well. To further visualize this dependence we plot the corresponding $\kappa \times \varepsilon_2$ points together with the obtained values for B which are shown as straight lines in Figure 3.7b). It needs to be mentioned that the κ errors as well as the ε_2 errors from the energy uncertainties in Figure 3.7a) contribute to the resulting errors of $\kappa \times \varepsilon_2$. These errors are therefore large at lower resonance energies due to the steepening of ε_2 (Figure 3.1a). The uncertainties for B, shown as semi-transparent line thicknesses, stem from the quality of the fit in Figure 3.7a).

In order to understand the dependence of B with respect to ε_m we plot the obtained values for B versus ε_m in Figure 3.7c). It can be seen that B depends linearly on ε_m as shown by the solid lines which are linear fits to the B points. We denote the proportionality constant with κ_{metal}, a material constant that only depends on the type of metal, and thus $\kappa(\omega, \varepsilon_m)$ can be written as

$$\kappa(\omega, \varepsilon_m) = \kappa_{metal} \frac{\varepsilon_m}{\varepsilon_2(\omega)}. \tag{3.3}$$
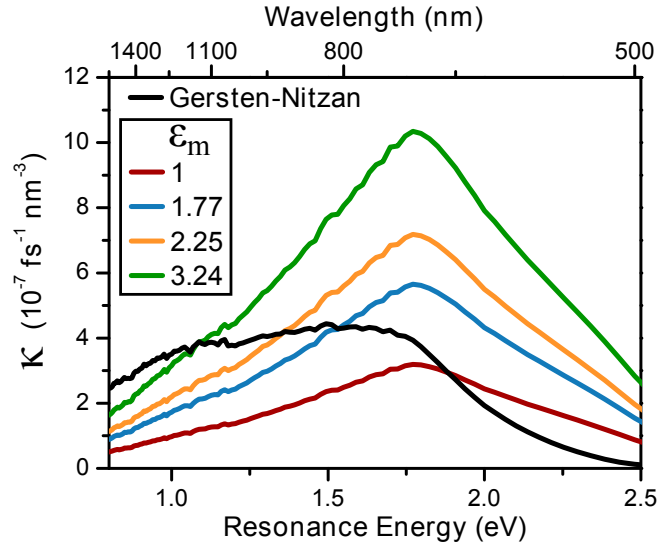
Figure 3.8: Our description of κ compared to the theoretical upper limit calculated by using the description of Gersten & Nitzan calculated in vacuum.[74]

For the dielectric function used for Au measured by McPeak,[17] we find

$$\kappa_{Au,McPeak} = (2.71 \pm 0.08)10^{-7} fs^{-1} nm^{-3} \tag{3.4}$$

The κ values calculated using Eq. 3.3 are plotted as solid lines in Figure 3.14a) and are compared to the obtained κ values from the FDTD calculations. As can be seen in Figure 3.14a) we found a good agreement for all ε_m in the analysed energy region. Radiation damping for NPs of a certain metal in the dipolar limit is thus governed by the medium, the imaginary part of the bulk dielectric function and the volume, resulting in

$$\Gamma_r(\omega) = 2\hbar\kappa_{metal}\frac{\varepsilon_m V}{\varepsilon_2(\omega)} \tag{3.5}$$

The inverse dependence of Γ_r on the imaginary part of the dielectric function ε_2 is reasonable because ε_2 determines the bulk damping of the metal and both processes are competing damping mechanisms, consistent with Hubenthal's work, which demonstrated that plasmon dephasing occurs in a correlated effect.[36] In the case of low bulk damping, i.e. low ε_2, radiation damping becomes more likely to happen. When bulk damping is strong, i.e. high ε_2, radiation damping is less efficient and bulk damping dominates. This is due to the fact that non-radiative processes in metals like electron-electron or electron-phonon scattering are fast.[72]

The theoretical description of Gersten and Nitzan[74] also predicts a decrease in κ at the onset of interband transitions. A comparison between their calculated upper limit of radiation damping for arbitrary shape and our description is shown in Figure 3.8. Gersten & Nitzan calculated an upper limit for the radiation damping for an isolated spheroid as[74]

$$\Gamma_r \leq \frac{4\pi^2 V}{3\lambda^3}\frac{((\varepsilon_1 - 1)^2 + \varepsilon_2)}{\varepsilon_2}\Gamma_{nr} \tag{3.6}$$

where Γ_{nr} is the nonradiative contribution to the line width. We calculated κ via their approach, using the bulk damping values extracted from our simulation data, and plotted it along with our results in Figure 3.8. Their description gives an upper limit for the radiation damping in vacuum, but does not describe the influence of the medium. When compared to our results for $\varepsilon_m = 1$, it can be seen that their approach gives an upper limit that does not describe the radiation damping data we found quantitatively. However, they do find that the radiation damping depends on $1/\varepsilon_2$ via a theoretical route, giving credibility to our found description.

Since radiation damping of localized surface plasmons has been proposed to be the main mechanism for luminescence of metal NPs,[68–71] the dependence of $\kappa(\omega)$ and measured quantum yields (QY) should show some qualitititative correlation. Yorulmaz et al. measured the QY of spherical Au NPs as well as NRs with resonance energies ranging from 1.6 eV to 2.35 eV. For NPs with aspect ratios lower than 3.5 and volumes of $V \approx 10^4$ nm^3, they found an increase in QY with decreasing resonance energy which was also attributed to a decreased non-radiative damping due to interband excitations. Although less measurements were performed in the region below 1.8 eV it seems from their data that the QY starts to decrease at lower energies. Fang et al. measured the QY of Au NRs with aspect ratios between 2.4 and 4 with resonance energies ranging from about 1.5 eV to 1.9 eV and found a decrease in QY with increasing aspect ratio and thus decreasing longitudinal LSPR resonance energy. They excited at the resonance energy of the transverse LSPR and explained their
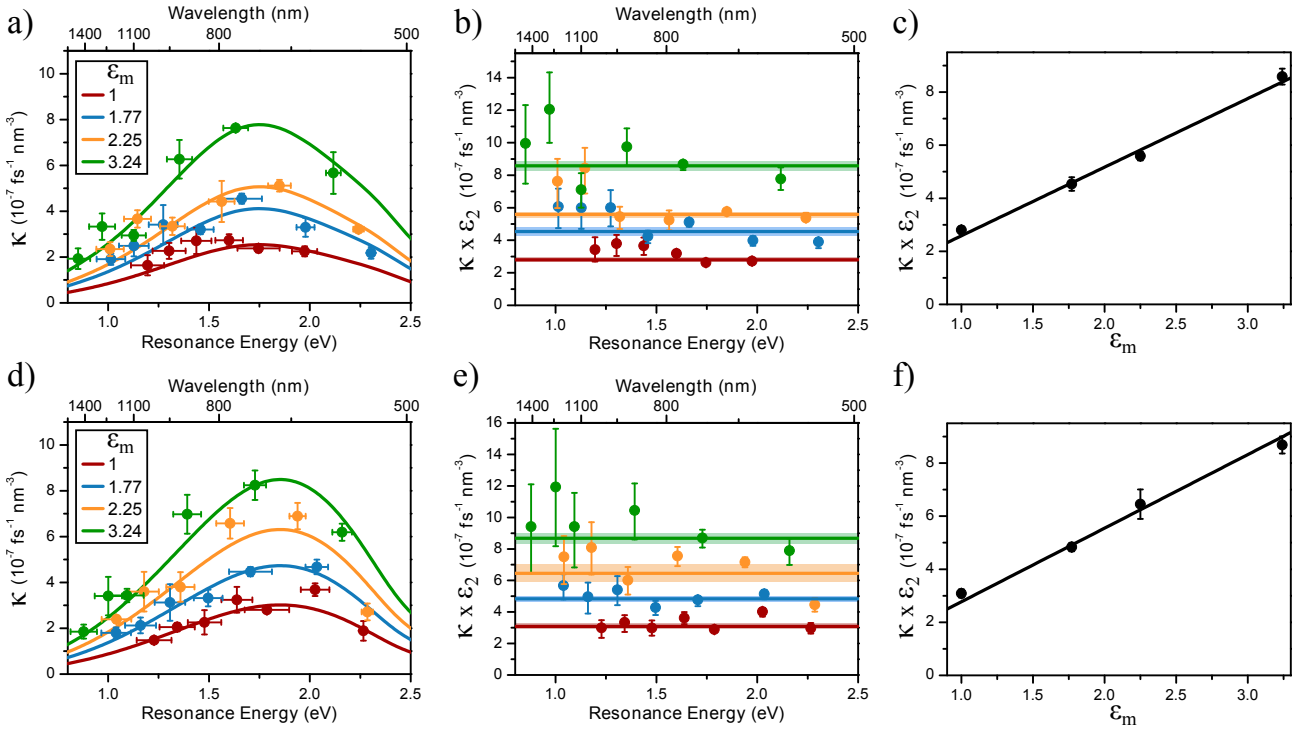
Figure 3.9: The procedure followed to determine κ dependencies for Au with the dielectric function of a-c) Olmon et al.[76] and d-f) Rioux et al.[77] a, d)The radiation damping constant κ obtained for Au NPs as a function of energy for different dielectric media. The solid curves are least-square fits to the data points of $\kappa = B/\varepsilon_2^{Au}$. b, e) Fitting parameter $B = \kappa \times \varepsilon_2^{Au}$ for the four different dielectric media. c, f) $B = \kappa \times \varepsilon_2^{Au}$ as a function of ε_m. The solid line is a linear fit to $B = \kappa \times \varepsilon_2^{Au} = \kappa_{metal} \times \varepsilon_m$.

findings by a weakening of the coupling strength between the absorption (transverse LSPR) and emission states (longitudinal LSPR) but it could also be explained by our results regarding the energy dependent strength of the radiative decay. Thus, both of the above mentioned measurements correlate well with our found κ dependence which suggests that our results could be used to predict luminescence efficiencies of metal NPs.

We furthermore compare our calculated results for κ by Eq. 3.3 to the ones measured in dark field scattering experiments[28,34,35] and obtained from simulations.[75] In experiments a smaller parameter space is generally accessible meaning that different groups probed different parts of the spectrum depending on their particles sizes and shapes. In dark field scattering experiments immersion oil is used as a surrounding medium (ε_m=2.25). We can reproduce the experimentally obtained κ values when using $\varepsilon_m = 2.25$ and the Au dielectric function of McPeak et al.[17] The comparison is shown in Figure 3.10. Considering possible differences in both the used dielectric functions and experimental uncertainties, like chemical interface damping, the agreement is very good.

In order to ensure that $\kappa_{Au,McPeak}$ is representative for the radiation damping behavior of Au and to validate our results we repeated the procedure for two different measurements of the Au dielectric function by Olmon et al.[18] and Rioux et al.[14] (Figures 3.9a-c) and 3.9d-f). The radiation damping calculated with these two dielectric functions obeyed Eq. 3.5 and yielded similar values for κ_{Au}: $\kappa_{Au,Olmon} = (2.59 \pm 0.06) \cdot 10^{-7}$ fs^{-1}nm^{-3} and $\kappa_{Au,Rioux} = (2.77 \pm 0.08) \cdot 10^{-7}$ fs^{-1}nm^{-3}. The slightly different values are not surprising as differences in preparing plasmonic films can lead to different qualities and thus varying dielectric functions.[17] For this reason we primarily used the dielectric functions from McPeak and co-workers[17] as much care was taken in preparing the plasmonic films. An average of the three obtained values for Au weighted by the inverse of their errors gives a representative value for the radiation damping parameter of Au which is $\kappa_{Au} = (2.67 \pm 0.06) \cdot 10^{-7}$ fs^{-1}nm^{-3}.
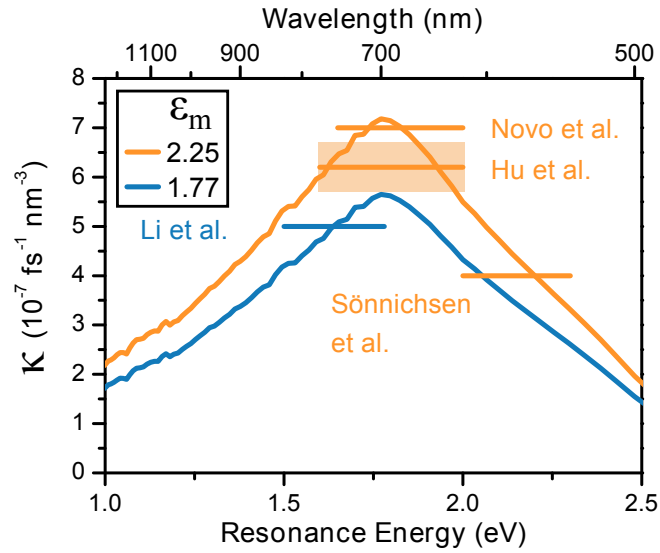
Figure 3.10: Comparison between our results based on Eq. 3.3 and experimental results by Sönnichsen et al.,[28] Novo et al.[34] and Hu et al.[35] in immersion oil ($\varepsilon_m = 2.25$). Simulation results of Li et al.[60] in water ($\varepsilon_m = 1.77$) are also included. The semi-transparent box around κ found by Hu et al.[35] indicates the error of their measurements.

Figure 3.11: Comparison of bulk damping Γ_b (black points) and radiation damping Γ_r calculated by Eq. 3.5 for the three different volumes $V = 10^3 \, \text{nm}^3$ (red solid line), $V = 10^4 \, \text{nm}^3$ (blue solid line) and $V = 10^5 \, \text{nm}^3$ (orange solid line) for a) Au, b) Ag, c) Cu and d) Al. The surrounding dielectric constant was $\varepsilon_m = 1.77$.

24

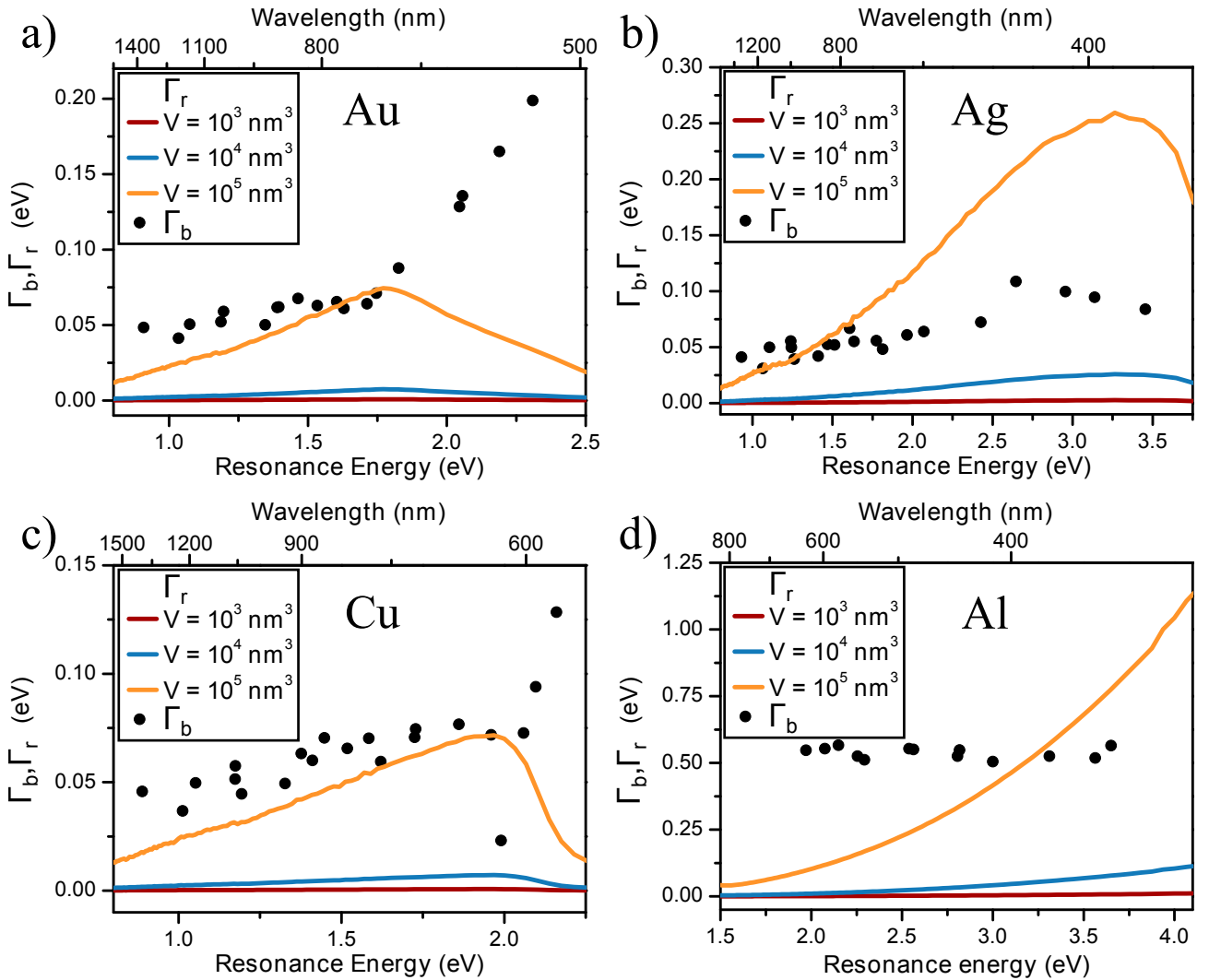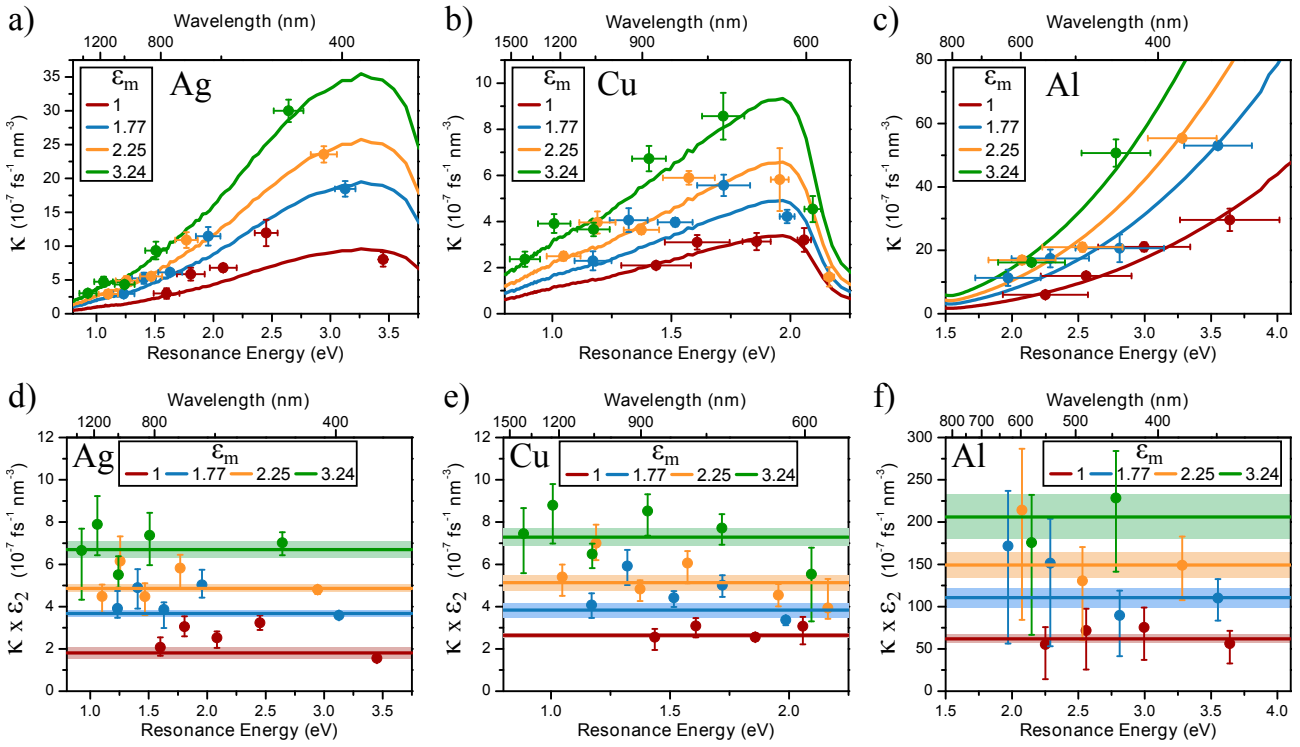Figure 3.12: The procedure followed to determine κ dependencies. a-c) The radiation damping constant κ as a function of energy for various dielectric media. The solid curves are least-square fits to the data points of $\kappa = B/\varepsilon_2$. d-f) Fitting parameter $B = \kappa \times \varepsilon_2^{Au}$ for the four different dielectric media.
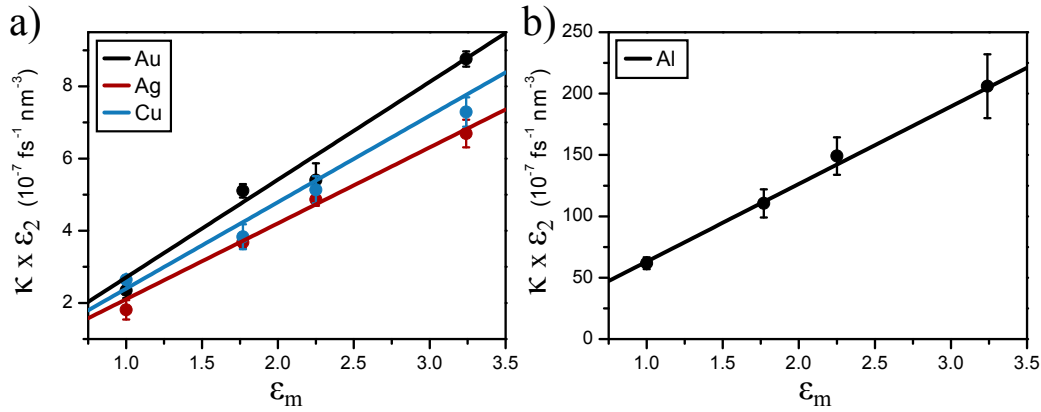

Figure 3.13: $\kappa \times \varepsilon_2$ vs ε_m, showing linear behavior for all metals.

3.3.3 Radiation damping in Au, Ag, Cu & Al nanoparticles

To find out whether Eq. 3.5 holds for different metals, i.e. whether κ_{metal} is a real material constant, we performed the same analysis as before for the other three metals Ag, Cu and Al (see Figures 3.12 and 3.13) and found good agreement with Eq. 3.3 over the energy range that could be analysed (Figure 3.14b-d). This strengthens our result that the dependence of κ on $1/\varepsilon_2$ is fundamentally true for different metals. It needs to be noted that the energy error bars for Al are larger than for the other metals because of the larger red-shifts with increasing volume (Figure 3.2d) and thus the error for κ_{Al} is probably underestimated as it is obtained from the linear fit of $B = \kappa \times \varepsilon_2$ as a function of ε_m (Figure 3.13) which shows a nice linear dependence despite the relatively large energy uncertainties for $\kappa(\omega)$ (Figure 3.12c). It needs to be mentioned that the overlap of the FDTD data and Eq. 3.3 for $\varepsilon_m = 1$ for Ag (Figure 3.14b) is worse because the point at the highest energy dominated the $1/\varepsilon_2$ fit due to its small error (see also Figure 3.12a).

The resulting values for the material radiation damping constant κ_{metal} are summarized in Table 3.1. It can be seen that Au, Ag and Cu exhibit similar κ_{metal}. Thus, radiation damping in such metal NPs at the same resonance energy varies mainly due to the differences in the imaginary part of their dielectric functions. In order to compare radiation damping to bulk damping we calculated Γ_r by Eq. 3.5 for the three different volumes $V_1 = 10^3 \, nm^3$, $V_2 = 10^4 \, nm^3$ and $V_3 = 10^5 \, nm^3$ and compared it to Γ_b as obtained from the linear fits in Figure 3.5. The results are shown in Figure 3.11. For all four metals Γ_r only considerably contributes to the overall damping in the case of the largest volume. Interestingly, this is also
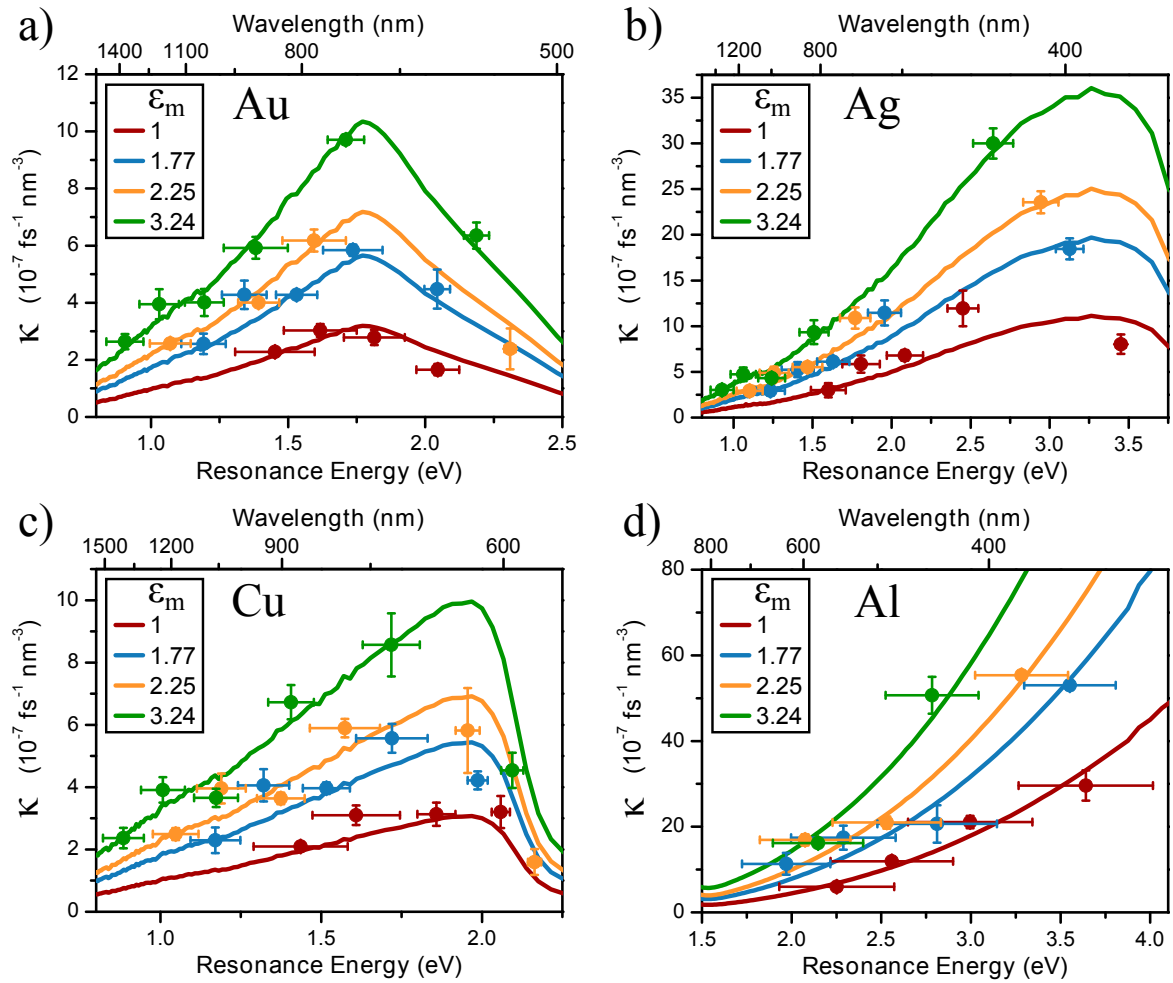
Figure 3.14: κ as a function of energy for different ε_m for a) Au, b) Ag, c) Cu and d) Al. The solid lines are calculated κ values from Eq. 3.3 which fit the by FDTD obtained data points very well.

	Au	Ag	Cu	Al
κ_{metal} ($\times 10^{-7}$ fs^{-1}nm^{-3})	2.71 ± 0.08	2.10 ± 0.04	2.40 ± 0.11	63 ± 1

Table 3.1: The material-dependent radiation damping parameter κ_{metal} for Au, Ag, Cu and Al, obtained from the dielectric functions measured by McPeak et al.[17]

Optimal radius (nm)	$AR = 2$	$AR = 3$	$AR = 4$	$AR = 5$	$AR = 6$
$\varepsilon_m = 1$	18.16	14.33	11.50	10.57	9.69
$\varepsilon_m = 1.77$	14.04	10.40	9.94	9.13	9.77
$\varepsilon_m = 2.25$	11.53	9.31	9.04	9.26	8.86
$\varepsilon_m = 3.24$	9.39	9.03	9.25	8.75	9.57

Table 3.2: Optimal radii in nm for Au NRs of different aspect ratios and for different ε_m calculated with the Au dielectric function found by Mcpeak et al.[17]

true for Al due to the higher bulk damping and because the higher κ_{Al} constant gets partially compensated by the larger ε_2. However, for larger energies radiation damping might also contribute for smaller volumes due to its rapid increase with energy. Nevertheless, our results are in contrast to ref.[59] where it was shown that radiation damping dominates for Al NRs with aspect ratios between 2.5 and 4.5 of volumes around $2 \cdot 10^4$ nm^3 in an energy range of circa 2-4 eV. However their general trend, i.e. increasing radiation damping with increasing energy (despite the slight decrease in volume from $2.6 \cdot 10^4$ nm^3 to $1.4 \cdot 10^4$ nm^3), agrees with our results. The discrepancy in Γ_r strength might stem from the different approaches in determining Γ_r. They determined the line widths obtained by the discrete dipole approximation (DDA) method, analytically calculated Γ_b and Γ_s and subtracted them from the simulated FWHM to obtain Γ_r. Their obtained Γ_b values are small (¡ 0.1 eV) which then leads to higher radiation damping. This deviation to our result ($\Gamma_b \approx 0.55$ eV) probably comes from the large variations between Al dielectric functions measured by different authors.[17] Figure 3.11b) visualizes the strong radiation damping at lower energies for Ag, as measured experimentally by Munechika et al.[44] Figure 3.11 furthermore reveals that Cu is a good alternative to the precious metals Au and Ag, especially in the infrared to visible part of the spectrum.

3.3.4   Optimal widths

With the obtained description of radiation damping and the available experimental results on the electron-surface scattering it is possible to determine the optimal widths of NRs of different aspect ratios in different media. They were determined by calculating the sum of the bulk damping, the electron-surface scattering and radiation damping for various radii, ranging from 5 to 20 nm in steps of 0.01 nm. The radius for which the sum $\Gamma_b + \Gamma_s + \Gamma_r = \Gamma_b(\omega_{res}) + A \frac{v_f}{l_{eff}} + 2\hbar \frac{\kappa_{metal}\varepsilon_m}{\varepsilon_2(\omega_{res})} V$ is lowest is the optimal radius. For a NP of a certain radius the resonance energy, which factors into the bulk damping and radiation damping contribution, was determined via interpolation between resonance energies known for radii used in the FDTD calculations. Since the surface scattering parameter A was mostly determined for Au NPs, we demonstrate this for Au NRs. The electron surface-scattering damping is hereby included as $\Gamma_s = Av_f/l_{eff}$ with $A = 0.3$ as found for Au rods and spheres by various authors.[34,35,38] The effective mean free path of the electrons l_{eff} is calculated using $4V/S$ where V is the volume and S the surface area of the NP.[32,33] Table 3.2 shows the results for aspect ratios ranging from 2 to 6 and ε_m from 1 to 3.24. As can be seen from Table 3.2 the optimal radii are between 8.73 nm and 18.16 nm. For smaller sizes electron-surface scattering dominates the dephasing of the electrons whereas for larger radii radiation damping becomes effective. For these moderate volumes Γ_b dominates the damping, especially at energies above 1.8 eV, as can be seen from Figure 3.11a). For that reason it is beneficial for smaller AR and ε_m, which have a resonance energy above or close to 1.8 eV, to have an increased volume which red-shifts the resonance energy and thus decreases Γ_b. At lower resonance energies, i.e. higher aspect ratios and ε_m, the optimal radii do not change much. The obtained radii around 9 nm for higher AR and ε_m are then simply a trade-off between Γ_s and Γ_r and agree well with experiments that showed that optimal diameters are around 20 nm.[34]

3.4   Conclusions

In conclusion, we systematically studied radiation damping $\Gamma_r = 2\hbar\kappa V$ in metal nanorods and nanospheres by FDTD simulations. Changing the aspect ratio of the NRs allowed us to probe a large range of resonance energies. We found that radiation damping scales with the inverse of the imaginary part ε_2 of the metal dielectric function and is proportional to the surrounding dielectric constant ε_m and can be calculated by $\Gamma_r = 2\hbar\kappa_{metal}\varepsilon_m V/\varepsilon_2$. The proportionality constant κ_{metal} was determined for Au, Ag, Cu and Al and the analytical expression found could reproduce the radiation damping behaviours obtained from FDTD simulations for all four metals and recent measurements on spherical Au NPs[28] and Au NRs[34,35] where κ was determined for limited resonance energy regimes. We furthermore showed that for volumes up to 10^4 nm^3 the overall damping for all four metals is mainly determined by bulk damping as long as surface contributions do

not play a role yet. Our results offer an analytical and intuitive description of radiation damping which can be extended to many different metals and can help to predict optimal sizes for metal NPs for various applications. In the future a similar experimental study could be conducted for the surface-scattering parameter A as it was also proposed to be energy-dependent.[36] Our description of Γ_r helps experimental studies to differentiate between Γ_r and Γ_s.

4 Nanorod samples characterized with extinction spectra

4.1 Introduction

Despite the increased control over Au NR synthesis,[6] samples usually have a rather broad distribution of aspect ratios. This has a big impact on the optical properties of the sample, because NRs with different AR exhibit different plasmon resonance wavelengths and intensities. The common way of determining the aspect ratio distribution is by determining sizes of 100 or more NRs from TEM images. The limited amount of NRs measured often yields statistically incorrect and irreproducible results. While TEM is an invaluable tool for material science and nanotechnology, the imaging of metal NRs for size measurements is costly and slow and so is the analysis afterwards, because the size measurements have to be done by hand. At least for NRs, available software cannot determine the size accurately enough.

However, characterizing samples by optical extinction spectroscopy (OES) is fast, cheap and does not destroy or waste any of the sample. Since polydispersity plays a significant role in ensembles of metal NRs, characterizing metal NRs requires a method that takes inhomogeneous broadening of the extinction spectrum into account. What we need to solve is essentially an inverse scattering problem to determine (geometrical) parameters of the NPs from extinction spectroscopy measurements.[78] Previous studies have done this using Mie-Gans theory[79] or semi-expensive methods like the T-Matrix method.[78,80–82] In contrast to those studies, we will be modelling single particle spectra using shape-corrected[51] and intensity-corrected Mie-Gans theory in order to investigate ensemble spectra. The shape factors found by Prescott & Mulvaney allow us to model spherocylinders, which is the shape that closely resembles experimentally synthesized metal NRs. We apply an intensity correction polynomial that ensures the Mie-Gans spectra have the same intensity as FDTD spectra.

This analysis of experimental ensemble extinction spectra yields useful information. Firstly, we obtain information on the aspect ratio distribution of the NRs in the sample, which is statistically more accurate than TEM as the amount of NRs contributing to the extinction spectroscopy signal is much larger than the typical amount of NRs measured in TEM images. Furthermore, we show that concentrations of the sample can be determined, as an alternative to destructive ICP measurements. Lastly, we employ the extinction spectroscopy method to study the value of the electron-surface scattering parameter A, which is used to calculate the extra damping due to the NP being smaller than the electron mean free path in Equation 2.17, for small NRs and compare our results with single particle measurements.

4.2 Method

Firstly, it is essential to calculate the extinction cross section C_{ext} of a single metal NR correctly. To this end, Mie-Gans theory, as described in chapter 2, was used in combination with shape factors found by Prescott & Mulvaney.[51] By comparing the Mie-Gans spectra to FDTD spectra of equivalent particles with equivalent damping terms (just radiation damping) we observed good agreement, except for the intensity of the plasmon resonance. An intensity correction factor was therefore included for the intensity in the Mie-Gans calculations. To determine this intensity correction, we compared Mie-Gans spectra with FDTD spectra of identical Au NPs and with identical damping terms. We found an intensity correction polynomial C, which is given by $C = 1/(2.95 - 0.38 \times (\omega_{res} + 0.02)^2)$, where ω_{res} is the resonance energy, which correctly describes the intensity correction for a large energy range. Furthermore, surface-scattering and radiation damping are included.

The absorbance A of an ensemble of NRs was measured with FTIR spectroscopy. The relation between the absorbance and C_{ext} of a single NP must be exploited. In the case of a monodisperse ensemble of NRs the absorbance A can be related to the total extinction A_{ext} by equating two definitions of the transmittance

$$\frac{I}{I_{inc}} = 10^{-A} = e^{-A_{ext}l} \qquad (4.1)$$

where the transmittance is the ratio of the transmitted (I) and incident (I_{inc}) light intensity and l the path length of the light through the sample. The extinction cross section C_{ext} of a single NR is related to the the total extinction A_{ext} as $A_{ext} = NC_{ext}$, where N is the amount of NRs per unit volume. So for a monodisperse sample the absorbance can be calculated by

$$A = \frac{lN}{ln10}C_{ext} \qquad (4.2)$$

Here, because on average all orientations of the NRs are encountered by the incident light, $C_{ext} = \frac{1}{3}C_{ext,long} + \frac{2}{3}C_{ext,trans}$, where $C_{ext,long}$ and $C_{ext,trans}$ are the extinction cross sections of the longitudinal and transverse LSPR, respectively. However, experimental samples are not monodisperse. As shown by several authors,[78–82] polydispersity can be included by adding a probability distribution function (PDF) that depends on the geometrical factors influencing the extinction spectrum of a particle, namely the aspect ratio (AR), the width (D) and end cap (e) geometry. With the inclusion of the PDF

$p(AR, D, e)$ the absorbance can be calculated as:

$$A(\lambda, AR, D, e) = \frac{lN_v}{ln10} \int_{AR_{min}}^{AR_{max}} \int_{D_{min}}^{D_{max}} \int_{e_{min}}^{e_{max}} p(AR, D, e)C_{ext}(\lambda, AR, D, e)dARdDde \tag{4.3}$$

In this description the aspect ratio, the diameter, the endcap shape and the PDF are unknown. With all these unknowns, the inverse problem is hard to solve. When the variables AR, D and e are discretized, the size of the matrix becomes too big to give a reliable and stable result. A solution for the problem is given in the following, which follows the method of Xu et al.[78] For NPs within the quasi-static limit, the optical response of the NRs is mainly dominated by the aspect ratio. Most particles of interest for applications are within this regime, where volume effects play a less significant role.[19,83–85] A recent synthesis procedure has shown it is possible to synthesize NPs with monodisperse width and end cap shape.[6] This means the integrals over D and e in Equation 4.3 can be replaced by the mean values of these parameters. To determine a reasonable mean value for the width D, knowledge of the synthesis or TEM images are needed. For the end cap geometry, knowledge of the synthesis procedure is usually enough. The end cap eccentricity e for NRs is usually between 0.7 and 1. By using the mean values for these two parameters the problem can be approximated to:

$$A(\lambda, AR, \overline{D}, \overline{e}) = \frac{lN_v}{ln10} \int_{AR_{min}}^{AR_{max}} p(AR, \overline{D}, \overline{e})C_{ext}(\lambda, AR, \overline{D}, \overline{e})dAR \tag{4.4}$$

Equation 4.4 can now be discretized with respect to only λ and AR. The optimization process will be a lot faster and more stable. The matrix equation that needs to be solved is

$$\boldsymbol{A} = \boldsymbol{CP} \tag{4.5}$$

where $\mathbf{A}$ is a $M \times 1$ vector which consists of the measured absorbance values at different wavelengths λ_m. The $M \times N$ matrix $\mathbf{C}$ contains all the extinction cross sections for different wavelengths λ_m for all discretized aspect ratios AR_n. The $N \times 1$ vector $\mathbf{P}$ is the PDF that needs to be solved for all aspect ratios AR_n. This matrix equation is solved using the method of Xu et al.[78] To find an accurate solution they used a numerical technique called Tikhonov regularization. The regularized least-squared solution $\mathbf{P}_{RLS}$ of Equation 4.5 is given as:

$$\mathbf{P}_{RLS} = min\left[(||\boldsymbol{A} - \boldsymbol{CP}||_2)^2 + \gamma^2(||\boldsymbol{I}(\boldsymbol{P} - \boldsymbol{P*})||_2)^2\right] \tag{4.6}$$

where $||\cdot||_2$ is the Euclidean norm, γ the regularization factor that is part of the solution and $\mathbf{P*}$ an *a priori* assumed solution that is taken as 0. $\mathbf{I}$ is the identity matrix. We can write Equation 4.6 as

$$\boldsymbol{P}_{RLS} = min\left[\frac{1}{2}\boldsymbol{P}^T\boldsymbol{QP} + \boldsymbol{q}^T\boldsymbol{P}\right] \tag{4.7}$$

where $\boldsymbol{Q} = 2(\boldsymbol{C}^T\boldsymbol{C} + \gamma^2\boldsymbol{I}^T\boldsymbol{I})$ is a symmetrical matrix of size $N \times N$, and $\boldsymbol{q} = -2\boldsymbol{C}^T\boldsymbol{A}$ is a $N \times 1$ vector.[78] We use the Nelder-Mead method to find the solution of Equation 4.7. The quality of the solution is determined by the mean square error (mse):

$$mse = \frac{1}{M}\sum_m\left[\frac{\mathbf{A}(\lambda_m) - \mathbf{A}_{cal}(\lambda_m)}{\mathbf{A}(\lambda_m)}\right]^2 \tag{4.8}$$

where $\boldsymbol{A}_{cal} = \boldsymbol{CP}_{RLS}$ is the optimal solution of the absorbance.

There is one main advantage of using Mie-Gans calculations in this scheme compared to T-Matrix calculations, which is that the calculations for the extinction spectra of a single particle per aspect ratio is much faster, compared to the T-matrix method that Xu et al. used.[78] The advantage of the increased speed is that parameters like the diameter D, the end cap eccentricity e, the electron-surface scattering parameter A and the radiation damping parameter κ. This allows for fast and detailed investigation of these parameters. The results are discussed in the following section.

4.3 Results & Discussion

4.3.1 Aspect ratio distribution: comparison to TEM

A way to validate the proposed method is to compare the calculated aspect ratio distribution with aspect ratio measurements from TEM images. Since the end cap of the NRs has a significant influence on the single NR spectra and therefore on the calculated aspect ratio, the end cap eccentricity is first measured from TEM pictures. Since the end cap geometry is similar for various NRs, only 20 measurements were done per sample to obtain the input parameter e. The width of the NRs in a sample was also relatively constant and was determined from TEM images with only 20 measurements per sample. The calculated aspect ratio distribution, using the mean diameter and end cap as input parameters, was compared with the aspect ratio distribution obtained via TEM characterization. This was done for six samples, which are characterized in Table 4.1. The aspect ratio distributions of those samples determined with the extinction spectroscopy method and

Sample	length (nm)	width (nm)	*AR*
JVH-045	70.8 ± 7.8	13.8 ± 1.7	5.2 ± 0.5
MB-AuNR-01	44.9 ± 6.3	12.4 ± 1.8	3.7 ± 0.6
MB-AuNR-02	91.5 ± 7.8	23.0 ± 2.2	4.0 ± 0.5
MB-AuNR-04	88.2 ± 7.4	24.4 ± 2.3	3.6 ± 0.4
MB-AuNR-09A	77.7 ± 8.4	17.1 ± 1.8	4.6 ± 0.6
MB-AuNR-10A	74.7 ± 9.4	14.9 ± 1.4	5.0 ± 0.7

Table 4.1: Characterization of samples that were used to determine the aspect ratio distribution in this section.
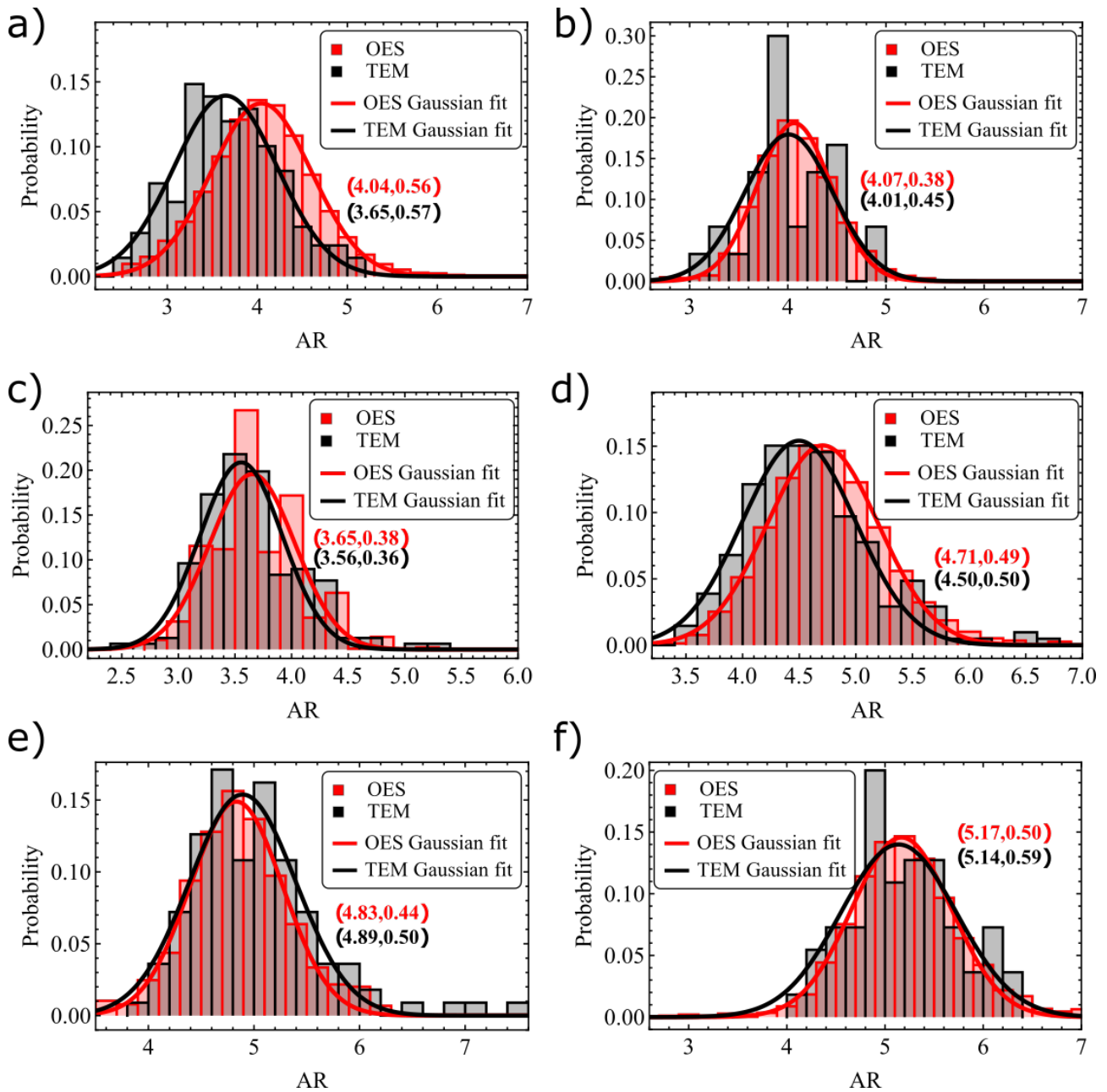
Figure 4.1: a-d) Comparison between the aspect ratio distributions calculated by the optical extinction spectroscopy (OES) method and measured with the TEM method of the following samples: a) MB-AuNR-01, b) MB-AuNR-02, c) MB-AuNR-04, d) MB-AuNR-9A e) MB-AuNR-10A and f) JVH-045. The values in parentheses $(\overline{AR}, \sigma_{AR})$ indicate the mean aspect ratio and the standard deviation of the OES (red) and TEM method (black).

Sample	length (nm)	width (nm)	AR
a	52.5 ± 6.3	11.8 ± 1.8	4.5 ± 0.6
b	42.0 ± 9.5	12.3 ± 2.4	3.5 ± 0.8
c	41.1 ± 6.7	14.3 ± 2.4	2.9 ± 0.5

Table 4.2: Characterization of samples, from Orendorff et al.,[86] that are used to test the concentration calculations in this section.

TEM are shown in Figure 4.1. With the measured mean values taken for the diameter and end cap geometry of the NRs, the extinction spectroscopy and TEM method agree well. It is important to note that only measured values were used as input and no parameters were chosen. This makes the agreement between both methods in both mean aspect ratio and in the standard deviation of the PDF remarkable and validates the use of the extinction spectroscopy method. It is faster, statistically more accurate and allows us to easily investigate unknown parameters, although the end cap eccentricity and width of approximately 20 particles needs to be determined from TEM, unless it is well known from the synthesis protocol what diameters and end caps can be expected. In the next section, we show that the extinction spectroscopy method can also be used to determine the concentration of the sample. It furthermore allows for easy and fast investigation of damping parameters, as shown in section 4.3.3.

4.3.2 Molar concentration of Au in metal nanorod samples: comparison to ICP

Another value that can be calculated using the extinction spectroscopy method is the concentration of the sample, knowledge of which would normally require time-consuming inductively coupled plasma mass spectrometry (ICP-MS) measurements, that destroy (part of) the sample. ICP measurements also require very large amounts of sample and it is not always easy to synthesize NPs in such big quantities. In order to test if the extinction spectroscopy method gives the correct concentration, samples of which both experimental ensemble extinction spectra and ICP measurements are available, are tested.

Firstly, the calculation used for determining the concentration from the extinction spectrum is given. The mean square error of the fit is minimized to obtain the best possible fit, with a parameter c_f that is determined from this minimization:[78]

$$min\,[mse] = min\left[\frac{c_f}{M}\sum_m\left[\frac{\mathbf{A}(\lambda_m)-\mathbf{A}_{cal}(\lambda_m)}{\mathbf{A}(\lambda_m)}\right]^2\right]$$ (4.9)

This parameter c_f is related to the concentration of a certain metal as:[78]

$$c = \frac{c_f V \rho}{M}$$ (4.10)

where c is the concentration in mol/L, V the average volume of the metal NP, ρ the density of the metal in g/L and M the molar mass of the metal in g/mol. The NP concentration c_{NP} in particles/L can be calculated as:

$$c_{NP} = N_A cnV$$ (4.11)

where c is the concentration, N_A the Avogadro constant, n the number density of metal atoms in a volume and V the average volume of the metal NP. The extinction coefficient that is often used in literature to compare the quality of samples of plasmonic NPs can be calculated as:[86, 87]

$$\varepsilon_{ext} = \frac{A}{lcnV}$$ (4.12)

In order to calculate the concentration with the extinction spectroscopy method, we use mean values for the diameter and endcap geometry determined by TEM as input values for the code. Since damping parameters have a big influence on the intensity of the localized surface plasmon resonance of a single particle and therefore on the calculated concentration of the sample, it is important to use good values for both radiation damping and electron-surface scattering. For the radiation damping, the relation $\Gamma_{rad} = 2\hbar\frac{\kappa_{metal}\varepsilon_m}{\varepsilon_2}V$, previously determined in chapter 3, is used. For the electron-surface scattering parameter A, a value of 0.29 was taken, which is close to most values reported in literature.[28, 34–36] The code calculates the aspect ratio distribution and from that the concentration as described above.

Samples from Orendorff et al.,[86] characterized in Table 4.2, were used to calculate the concentration. In their work, they reported both the ensemble extinction spectra and the ICP measured Au concentrations of their samples. By digitizing the ensemble extinction spectra with GetData Graph Digitizer and using them as input for the extinction spectroscopy code, a concentration was calculated. Both the ICP measured Au concentrations and the Au concentrations calculated with the extinction spectroscopy code for various samples used by Orendorff et al.[86] are reported in Table 4.3. The code was run for aspect ratios between 1.6 and 7.6 with $\Delta AR = 0.2$. The wavelength range was probed between 550 nm (600 nm

Concentration (mM)	a	b	c
ICP	0.073 ± 0.005	0.071 ± 0.006	0.075 ± 0.004
Extinction spectroscopy	0.074	0.077	0.059

Table 4.3: Concentration measured by ICP and calculated via the extinction spectroscopy code of samples from Orendorff et al.[86] in mM.

for sample a) which has higher aspect ratios) and 1200 nm in steps of 10 nm. This ensured NRs of all aspect ratios were included in the calculation for the concentration. For two of the three samples the agreement is satisfactory. However, the concentration calculated with the extinction spectroscopy method for sample c) is significantly lower than the ICP measured concentration. This may indicate that the code calculates the concentration less well for lower aspect ratios. A possible explanation for the significantly deviating concentration is that the amount of nanospheres is more significant in this sample. The OES method does not determine the concentration of Au that is represented in spheres.

4.3.3   Electron-surface scattering parameter

In order to investigate the electron-surface scattering parameter A we use samples with small diameters ($D < 18$ nm), to maximize the influence of the electron scattering off a surface and to minimize the effect of radiation damping. For the small influence of radiation damping, we use the relation from chapter 3: $\Gamma_{rad} = 2\hbar \frac{\kappa_{metal}\varepsilon_m}{\varepsilon_2} V$. The samples used for this section are characterized in Table 4.4. As diameter and end cap geometry we use values measured from TEM images. By evaluating the extinction spectroscopy code for different A values, we obtain different values for the mean square error (mse) of the fit as defined in Eq. 4.8. The lower the mse, the better the fit so it gives an indication of when the right A value is used. The code was run for aspect ratios between 2.2 and 7.6 with $\Delta AR = 0.2$. The wavelength range explored was between 600 and 1200 nm in steps of 10 nm. The five samples characterized in Table 4.4 were tested for different values of A. The mean square errors of the fit as a function of A for two of those samples are reported in Figure 4.2. Table 4.5 gives the surface-scattering parameter A of each sample for which the mse is lowest.

Sample	length (nm)	width (nm)	AR
JVH-045	70.8 ± 7.8	13.8 ± 1.7	5.2 ± 0.5
MB-AuNR-01	44.9 ± 6.3	12.4 ± 1.8	3.7 ± 0.6
MB-AuNR-09A	77.7 ± 8.4	17.1 ± 1.8	4.6 ± 0.6
JVH-LA-004-1-s	28.9 ± 4.5	7.2 ± 1.0	4.0
JVH-LA-005-2	27.7 ± 4.7	8.6 ± 1.4	3.2

Table 4.4: Characterization of samples that are used to determine the electron-surface scattering parameter in this section.

The A factors with the lowest mse are in between 0.2 and 0.4 for all samples. The errors for A are obtained by estimating, via interpolation, for which value of A, the mse is 1.5 times the lowest mse value. We believe a reliable value for the surface-scattering parameter A in the investigated energy range is given by the weighted mean value of these values:

$$A = 0.30 \pm 0.02 \tag{4.13}$$

This value for A is in good agreement with single particle studies.[34–36] Hu et al. determined $A = 0.30 \pm 0.03$ for NRs of aspect ratio 3,[35] where Novo et al. obtained $A = 0.27$ for Au NRs of aspect ratio 2 to 4.[34] Frank Hubenthal found that
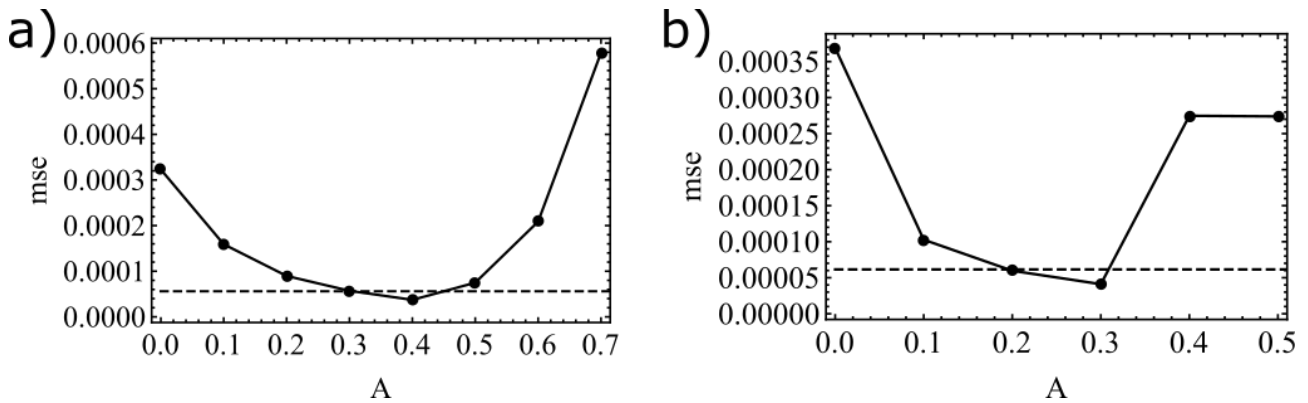

Figure 4.2: Mean square error (mse) of the ensemble spectrum fit as a function of the surface-scattering parameter A for a) JVH-LA-004-1-s and b) JVH-045. The dashed line indicates the value corresponding to 1.5 times the lowest mse, which is used to estimate the error in the determination of A.

Sample	$\overline{AR}$	ω_{res} (eV)	$\overline{A}$
JVH-045	5.2	1.32	0.3
MB-AuNR-09A	4.6	1.37	0.2
JVH-LA-004-1-s	4.0	1.49	0.4
MB-AuNR-01	3.7	1.51	0.3
JVH-005-2	3.2	1.61	0.4

Table 4.5: Electron-surface scattering parameter A with the lowest fit mse for various samples.
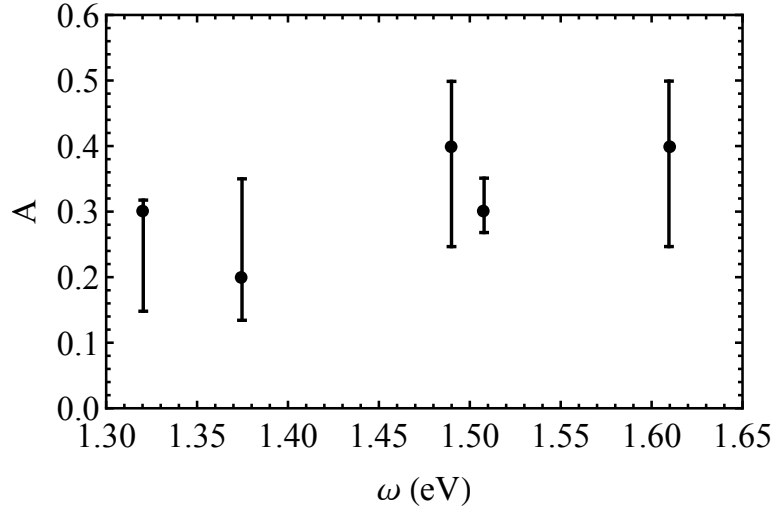
Figure 4.3: Found values for the electron-surface scattering parameter A plotted against the resonance energy of that particular sample. The errors are estimated by interpolation between data points and checking for which A the mean square error is 1.5 times as high as the lowest mse.

the surface-scattering parameter A depends on resonance energy of the LSPR, where A was found to be between 0.1 and 0.4 for resonance energies from 1.6 to 2.3 eV.[36] It was proposed that interband transitions play a role in the behaviour of surface-scattering, similar to what we obtained for radiation damping in chapter 3. The values that we obtained for A (Figure 4.3) do not show a clear dependence on energy, which is likely due to the limited accuracy of this method in determining A and because interband transitions play no role in this energy range. It is remarkable that we extracted A this accurately at all from just an ensemble measurement, where inhomogeneous broadening effects are present. Xu et al.[78] also used their OES code to investigate different values of A factors. They concluded that the mse increased beyond their threshold for $A > 0.6$. They did not investigate A further, presumably due to their T-Matrix approach to calculating single particle spectra, which is time-consuming. The good agreement between our results and single particle dark-field scattering results for the electron-surface scattering parameter A shows the good functionality of our method to obtain damping parameters.

4.4   Conclusions

It has been shown that the extinction spectroscopy code described in this chapter is a powerful tool for quick analysis of ensembles of plasmonic NRs. The calculated aspect ratio distributions agree well with TEM analysis, when reasonable mean values for the diameter and end cap eccentricity are provided. Furthermore, concentrations can be extracted quickly, which is an improvement over experimental methods like ICP, which are time-consuming and/or destructive. Additionally, it enables us to investigate individual damping parameters from ensemble measurements that are inhomogeneously broadened. The obtained electron-surface scattering parameter $A = 0.30 \pm 0.02$ agrees well with values reported from single particle measurements.[34–36]

5 Alloying of Au-Ag nanoparticles

5.1 Introduction

Ag has the best plasmonic properties of all metals due to low damping of the plasmon resonance over a large energy region. However, Ag has a relatively poor chemical stability compared to Au and is therefore not often used for applications. Growing a Ag shell around Au NPs improves the plasmonic properties, but the usefulness of these NPs in applications is still hindered by the instability of the Ag shell. By alloying the Au atoms from the core and the Ag atoms from the shell, the chemical stability can be significantly improved, as has been shown for nanospheres[88] and nanorods.[25]

Alloyed metal NPs are interesting for several reasons. Firstly, the composition allows for extra tunability of the plasmon resonance. Secondly, alloying can lead to increased thermal stability of the NPs,[23] which could be particularly important for NRs in photothermal applications. Alloyed Au-Ag NPs are also interesting for catalysis. A Au-Ag alloyed NP, with both Au and Ag atoms as active sites for catalysis, was shown to be more catalytically active than a monometallic Au or Ag NP for CO conversion.[23] The catalysis of such metal NPs can be enhanced even further by irradiating it with light, as local field enhancements near the particle's surface due to the excited LSPR can aid the catalysis.[24]

The effect of important parameters on the alloying process of anisotropic bimetallic NPs has not yet been studied. In this chapter, the influence of quantities like size, aspect ratio and composition on the alloying process of Au-Ag core-shell NRs coated in mesoporous silica is investigated. For anisotropic NPs, two processes take place when sample of Au-Ag core-shell NRs are heated at sufficiently high temperatures: particle deformation and alloying. Particle deformation is due to kinetic and thermodynamic driving forces that rearrange surface atoms to minimize the surface free energy. This process ceases to happen when thermodynamic equilibrium has been reached. At high temperatures, the NRs therefore lose their anisotropy and deform towards spherical NPs. Alloying of Au-Ag core-shell NPs is a kinetic process and is therefore significantly sped up at elevated temperatures. The NPs used in this chapter are coated with a mesoporous silica shell, as described in section 5.3.1. The NRs coated with mesoporous silica do not deform as much as uncoated NRs when thermally heated. Petrova et al. showed that bare Au NRs were completely deformed to a spherical shape at 250 °C.[89] This makes it impossible to alloy uncoated Au-Ag core-shell NRs, while retaining the elongated shape. Albrecht and Van der Hoeven et al. alloyed Au-Ag NRs coated in a mesoporous silica shell while preserving the NR shape.[25]

We briefly discuss previous experiments on the alloying of Au-Ag core-shell NPs. Shibata et al. alloyed Au-Ag spherical NPs with a 2.5 nm Au core and 3 and 5 atomic layers of Ag at room temperature.[90] They monitored the ensemble extinction spectrum via UV-Vis spectroscopy in order to determine the time needed for alloying. The NPs with 3 atomic layers of Ag took 3 days to alloy, while those with 5 atomic layers of Ag took 4 days to alloy, indicating that the total particle volume has an effect on the alloying process at these small volumes. Even more interesting behaviour is found when comparing studies of alloying for differently shaped particles of similar volumes. Gao et al. recently found that a temperature of 930 °C was needed to fully alloy nanospheres with sizes around 15 nm.[88] However, Albrecht and Van der Hoeven found that nanorods with volumes 6.6 times higher than the nanospheres of Gao et al. could be fully alloyed at 450 °C.[25] This significantly reduced alloying temperature was ascribed to the out-of equilibrium shape of the NRs.

This chapter first describes the synthesis of Au-Ag core-shell NRs. Furthermore, this chapter contains three different heating experiments. Firstly, in order to study the influence of size, aspect ratio and Au/Ag ratio on alloying, we conducted in-situ measurements of the alloying process by extinction spectroscopy measurements. Here we make use of our previously gained knowledge on the plasmon resonance of these types of NPs. Secondly, the alloying process upon heating of spherical Au-Ag core-shell NPs and NRs with aspect ratio 2.9 with the same volume and Au/Ag ratio was followed in-situ in an electron microscope and analyzed via transmission electron microscopy (TEM), high-angle annular dark-field scanning transmission electron microscopy (HAADF-STEM) and energy-dispersive x-ray spectroscopy (EDX). Lastly, we studied if it is possible to alloy Au-Ag core-shell NRs by using femtosecond laser pulses.

5.2 Theory

Alloying of Au-Ag core-shell NPs is mediated through the diffusion of Ag atoms into the Au core and Au atoms into the shell until a full alloy is formed. The mechanism that facilitates the diffusion in Au-Ag NPs is vacancy diffusion, because Au and Ag have close lattice constants, differing by only 0.71 pm, meaning they form a solid solution. In order for an atom to migrate via vacancy diffusion it jumps from its current lattice site to an empty lattice site. The probability of an atom to move is therefore the product of the probability of having a vacancy in an adjacent lattice site and the probability of the atom having sufficient energy to jump to that empty lattice site. Sufficient energy is required because bonds with the atom's neighbours need to be broken, after which energy is needed to move the atom to the position of the vacancy. The energies for breaking the bonds and moving the atom are together called the activation energy E_A. The activation energy is more often reached at elevated temperatures, as the thermal energy of the atom is higher. The temperature-dependent

diffusion coefficient D is then described by the Arrhenius equation:

$$D = D_0 e^{-E_A/k_B T} \tag{5.1}$$

where D_0 is the frequency factor, E_A the activation energy, k_B the boltzmann factor and T the temperature. As seen in Equation 5.1, several factors play a role in the diffusion rate. Firstly, the temperature influences the diffusion rate exponentionally. Furthermore, the lower the activation energy, the higher the diffusion coefficient, which means the diffusion rate increases. The activation energy E_A and frequency factor D_0 are affected by which atom species diffuses into which host species. In our case, Au and Ag atoms are diffusing into either a Au, Ag or a Au-Ag alloy environment. Lastly, the structure around the diffusing atom has a large impact. It matters greatly whether the atom has to diffuse through a perfect crystal, through a grain boundary or over a surface. Equation 5.1 shows us why we need elevated temperatures in order to alloy Au-Ag NPs, for which the activation energies for diffusion are similar to bulk activation energies. An atom's average thermal energy at room temperature ($k_B T = 0.026\,\text{eV}$) is much lower than the activation energy for bulk Au, Ag and their alloys, namely $1.76 - 2.10\,\text{eV}$.[91] Therefore, the chance of the required activation energy being at the disposal of one atom is low and diffusion of atoms and therefore the alloying process is slow.

As we have seen, the rate of diffusion depends on many factors like size, shape, vacancy concentration and composition. We briefly discuss the available literature on the effects of these factors on the diffusion of Au and Ag. Dick et al.[92] looked at the size-dependent self-diffusion of Au atoms in silica-encapsulated spherical Au NPs. They determined the melting point of NPs with sizes between 1.5 and 20 nm using differential thermal analysis (DTA) coupled to thermal gravimetric analysis (TGA) techniques. They discussed the implications of their findings on the self-diffusion within these NPs. They argued that the dependence of the diffusion rate on temperature can be described as

$$D(r) = D_m e^{-E_A(T^{-1} - T_m(r)^{-1})} \tag{5.2}$$

where D(r) is the size-dependent diffusion coefficient, D_m the diffusion coefficient of the bulk material at the melting temperature and T_m(r) the size-dependent melting temperature. They found that the melting temperature started to decrease significantly below sizes of 20 nm. Below those sizes the diffusion coefficient started to increase exponentially. They concluded that small bimetallic core-shell NPs could alloy at room temperature over a few days. Shibata et al.[90] observed this experimentally, although the size-dependent diffusion coefficient found by Dick et al.[92] was not sufficient to explain their observations. Therefore, they proposed the occurancy of vacancies at the interface of the initial core-shell configuration. Using Molecular Dynamics (MD) simulations they showed that if a few percent of the interface sites were vacancies, their experimental alloying times could be explained.

The composition of the NP can also have an effect on the diffusion. The diffusion of Ag and Au atoms in Au-Ag alloys of several compositions and their respective pure metals was measured in bulk by Mallard et al.[91] by using tracer atoms. Both Au and Ag tracers were used. Their data accurately obeyed the Arrhenius equation, which allowed them to extract the temperature-independent frequency factors and activation energies. They found that both Au and Ag tracers diffused more quickly in bulk material which contained relatively more Au than Ag. The activation energy was found to decrease with Au molar fraction. The activation energy for a Au tracer diffusing in pure Ag was approximately 20% higher than a Ag tracer diffusing in bulk Au. These observations imply that Ag atoms from the shell diffuse more quickly into the Au core than the other way around.

The influence of the shape of the NP on the alloying process has not yet been investigated experimentally in literature, because, to the best of our knowledge, solely alloyed nanospheres have been synthesized by thermal treatment until Albrecht and Van der Hoeven synthesized Au-Ag alloyed NRs.[25] Thermal and photothermal reshaping of Au NRs has been observed to depend on shape.[89,93] Thus it seems likely that atom diffusion facilitating alloying also depends on shape.

5.3 Methods

5.3.1 Core-shell nanorods: synthesis & characterization

Au NRs in a mesoporous silica shell (AuNRs@meso-SiO$_2$) were used to make Au-Ag core-shell NRs (AuNRs-Ag@meso-SiO$_2$). The mesoporous silica shell stabilizes the NRs, both colloidally and thermally against deformation at elevated temperatures. Due to the porosity of the silica shell, the metal NR surface is still accessible for catalysis and sensing applications. Firstly, the Au NRs were synthesized via a seeded growth method using binary surfactant mixtures, as reported by the group of Murray.[6] These NRs were then coated with a mesoporous silica shell as described by Gorelikov and coworkers.[94] The used AuNRs@meso-SiO$_2$ NRs were provided by Jessi van der Hoeven. In the method section of this chapter, the last two steps in synthesizing AuNRs-Ag@meso-SiO$_2$,[95] as well as the characterization of the NPs via electron microscopy and extinction spectroscopy will be explained. We will then discuss the results of the characterization for NPs that will be used for alloying experiments, as well as compare the ensemble extinction spectra of those core-shell
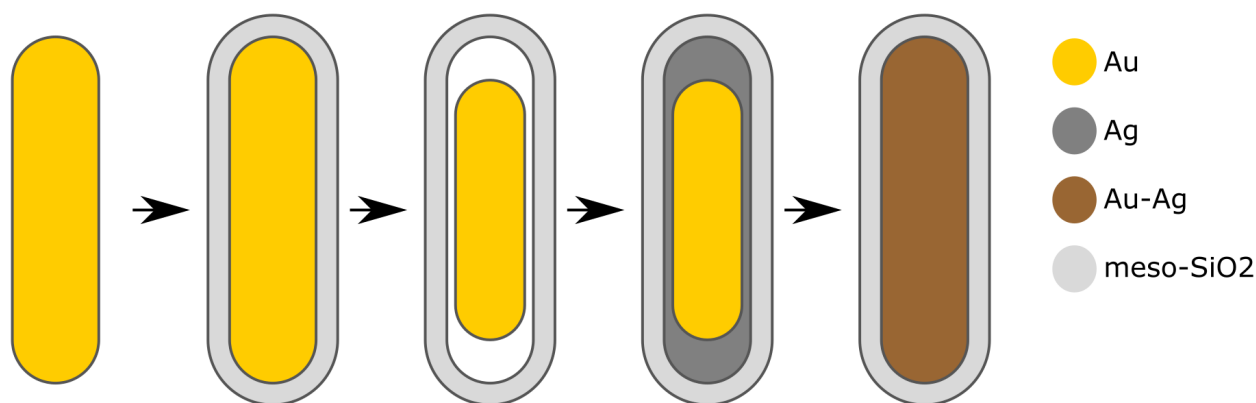
Figure 5.1: Visual representation of the synthesis of the silica-coated Au-Ag NRs. First, a bare NR is synthesized and subsequently coated with mesoporous silica. Some of the gold is etched away to make space for the Ag deposition. The last step is the alloying of the Au-Ag core-shell NP.

NPs with single particle spectra calculated with Mie-Gans theory.

Two more steps are to be done in order to make AuNRs-Ag@meso-SiO$_2$: etching and Ag deposition. It was shown by Deng et al.[95] that AuNRs@meso-SiO$_2$ can be etched and that a different metal can be deposited on the Au NR. The method of Deng et al. will be used (with some modifications) for the described synthesis. Figurre 5.1 shows the complete synthesis of silica-coated Au-Ag NRs.

The provided AuNRs@meso-SiO$_2$ were oxidatively etched to create space in the mesoporous silica shell for Ag deposition. The AuNRs@meso-SiO$_2$ were dispersed in methanol and diluted until the Absorbance of the sample in a 1 cm cuvette equalled 3, giving an indication of the concentration. For every sample, around 10 mL dispersion was used. In this description, we use a 10 mL Au NRs dispersion, but the procedure can be scaled up to volumes larger than 200 mL. A 40 mL vial (with stirring bar) with a 10 mL solution of Au NRs with mesoporous silica shell in methanol was placed in a 60 °C oil bath on a stirring plate. After waiting a few minutes until the dispersion had the required temperature, the etching procedure could be started. This was done by adding 0.2 mL concentrated HCl (37% in water, Sigma-Aldrich) and 0.2 mL H_2O_2 (30% in water, Sigma-Aldrich) in methanol (200-500x diluted, depending on etching speed) to the solution. The vial was closed by a cap to prevent HCl evaporation. The solution was stirred in a 60 °C oil bath. The temperature was kept constant during the etching procedure. Extinction spectra were used to check how much gold had been etched away. This was done by taking samples from the etching solution and diluting it with an equal volume of cold methanol to quench the etching process. When the desired amount of etching had been done, the etching solution was diluted 2 times with room-temperature or cooler methanol. The dispersion was then washed once with methanol and twice with ethanol, where the centrifuge was operated at 9000 rcf for 10 minutes each time. The resultant etched AuNRs@meso-SiO$_2$ were stored in ethanol at room temperature.

For the Ag deposition the etched AuNRs@meso-SiO$_2$ need to be dispersed in water and diluted until the Absorbance measured in a 1 cm cuvette is approximately 2. All the water used was ultrapure water (Millipore Milli-Q grade) with a resistivity of 18.2 MΩ. Solutions of AgNO$_3$ ($\geq$ 99%, Sigma-Aldrich) and L-ascorbic acid (BioXtra, $\geq$ 99%, Sigma-Aldrich) in water were prepared. Depending on the desired amount of Ag for the deposition, the molar concentration of the AgNO$_3$ solution was 1-4 mM. The molarity of the ascorbic acid solution was 4 times higher than that of the AgNO$_3$ solution. The description that follows is based on the use of 1 mL etched AuNRS@meso-SiO$_2$ dispersion, but as long as the volume of the initial dispersion does not deviate greatly from 1 mL the other named volumes can be scaled accordingly. Before the Ag deposition process was started, a 4 mL vial (with stirring bar) with 1 mL of the etched AuNRs@meso-SiO$_2$ dispersed in water was placed in an ice bath. This slows down the Ag deposition to get more monodisperse NPs. After a few minutes the Ag deposition was started. While stirring, first 0.1 mL of the AgNO$_3$ solution and then 0.1 mL of the ascorbic acid solution was added. Even in an ice bath, the reaction happened quickly. After 10 minutes the Ag deposition was completed. The solution was washed once in water and twice in ethanol, with centrifuge speeds of 9000 rcf and 10 minutes of centrifuging for every washing step. The AuNRs-Ag@meso-SiO$_2$ in ethanol dispersion was stored in a refrigerator to prevent dissolving of the Ag shell ($\geq$ 6 months).

We will now discuss the two methods used to characterize these particles. Firstly, extinction spectra were measured using a FTIR spectrometer (Bruker Vertex 70) in order to determine the optical properties of an ensemble of NRs. For these measurements in a 1 cm cuvette, we used a near-infrared source, a quartz beamsplitter and a room-temperature Si-diode detector, which allowed us to measure in the visible regime as well. It needs to be mentioned that the Si-diode

detector gives unreliable results for wavelengths below 500 nm. Secondly, bright-field transmission electron microscopy (BF-TEM) images were acquired with a Fei Tecnai-12 operating at 120 kV and the resultant images were used for geometrical determinations. The TEM grids were prepared by evaporating a 5 μL droplet of NRs in ethanol. The dropcasted solution had an absorbance of approximately 8, which is indicative for the concentration.

5.3.2 In-situ heating measurements with extinction spectroscopy

The extinction spectroscopy measurements were done on a microscope stage (Bruker Hyperion) of a FTIR (Bruker Vertex 70). A temperature controlled IR stage from Linkam Scientific Instruments was used, more specifically the horizontal FTIR600, in the following referred to as the Linkam cell. It was connected to a nitrogen source, allowing a nitrogen flow through the chamber of the Linkam cell. The temperature of the Linkam cell could be varied from room temperature to 600 °C in steps of 0.1 °C. The Linkam cell was mounted on the upright microscope and kept in place via clamps. It was important to have the Linkam cell aligned with the microscope to obtain a decent amount of signal. For x and y this was done by slowly pushing the Linkam cell across the microscope and optimizing the signal. The stage upon which it was mounted could then be adjusted for height to get the best signal possible. We used a near-infrared source, a quartz beamsplitter and a Si-diode/GaP-diode detector, which enabled us to measure in the visible and near-infrared regime. Measurements were conducted via the left exit channel and with an aperture width of 3 mm. Data were acquired from 550 to 1200 nm. In order to have the best signal-to-noise ratio, 120 scans were done per measurements with a scanner velocity of 2.5 kHz.

In the following the method for a measurement for a single sample is explained. The Au-Ag core-shell NPs in ethanol were stored in a fridge in order to maintain their stability, as discussed previously. The sample was dropcasted on a glass slide using a pipette. After dropcasting 5 μl, the droplet was given time to evaporate. This was repeated approximately 5 times, until there was enough sample on the glass slide to give enough signal in the FTIR. A vacuum tweezer was used to place the dried sample inside the Linkam cell, in order to keep the glass clean. Firstly, a background measurement was conducted. Therefore, the bare glass was placed in the cell. A metallic ring is placed upon the glass slide to keep it in place. The Linkam cell is then closed using a lid with an optically transparent BaF$_2$ window. A nitrogen flow is sent through the cell, as the alloying is also performed under nitrogen. We waited 10 minutes before the background measurement was taken, which should be sufficient time to fill the small volume of the Linkam cell with nitrogen. After the measurement, the lid is the unscrewed and the metallic ring is taken off the glass slide. The part of the glass slide which contained the most sample is now put in the Linkam cell. After this, the metallic ring is placed back upon the glass slide and the lid in screwed back on. The nitrogen flow is given time to fill the chamber of the cell with nitrogen once again. This time period is normally taken to be twenty minutes, since it is really important that the sample is only heated while under nitrogen atmosphere, as it was seen that Ag atoms diffuses out of the NP when heated under air.[25] The sample was heated via the internal pure silver heating block inside the Linkam cell, upon which the glass slide lies. The ramp and final temperature can be controlled via the Linkam TP94 device. A temperature ramp of 10 °C per minute was used. This ensured that the temperature increase was sufficient to make sure that most alloying is yet to happen when the maximum temperature is reached. When the maximum temperature is reached a repeated measurement is started. Spectra are measured a certain time apart. The first hour a measurement was taken every 5 to 10 minutes. Beyond the first hour, measurements were being taken every half hour to an hour, depending on the temperature of the measurement. We used different maximum temperatures per measurements, between 225 and 300 °C. For these temperatures the alloying process takes between six hours and several days. After the measurement the Linkam cell was cooled down at 10 °C per minute. When room temperature was reached, the glass with the sample was taken out and TEM grids were prepared. This was done by putting a small droplet (5 μl) of ethanol on the sample and carefully stroking the TEM grid over the droplet, in order for some NRs to stick to the polymer film of the grid.

All the spectra that were collected were subsequently fitted to Gaussians, to filter out the noise, as seen in Figure 5.2. Since the noise is not equal across the whole frequency range, frequency points at higher frequencies than the frequency of the peak are excluded in order to improve the reliability of the Gaussian fit. The Gaussian fitting procedure allowed for retrieval of the peak position. The change in peak position (compared to the first spectrum taken at maximum temperature) is then plotted versus the time the sample has been heated at the maximum temperature. With Mie-Gans calculations it is possible to predict the peak position change during the alloying process. The alloying process is then assumed via a very simple model. For a 50/50 Au/Ag core-shell NR ($AR = 3$), the Au core is half the volume of the total particle. In this model, the core size is kept the same throughout the alloying process, but the Au molar fraction of the core is decreased, while that of the shell is increased. In other words, Ag atoms are diffusing into the core and Au atoms are diffusing into the shell, without the shapes or volumes of the core and shell changing. Calculating the peak positions of this particle during alloying with this model shows a blue-shift in the peak position, as in Figure 5.3. The analysis of the experimental spectra was complicated by the deformation of the NRs to a more spherical shape. This aspect ratio loss for the NPs coated with mesoporous silica is much less than uncoated NRs, but some deformation still takes place. As we have seen in chapter 2, a lower aspect ratio NR will result in a LSPR peak position that is blue-shifted with respect to the higher aspect ratio NR. The importance of distinguishing these two causes for a blue-shift, namely alloying and deformation, is clear if we
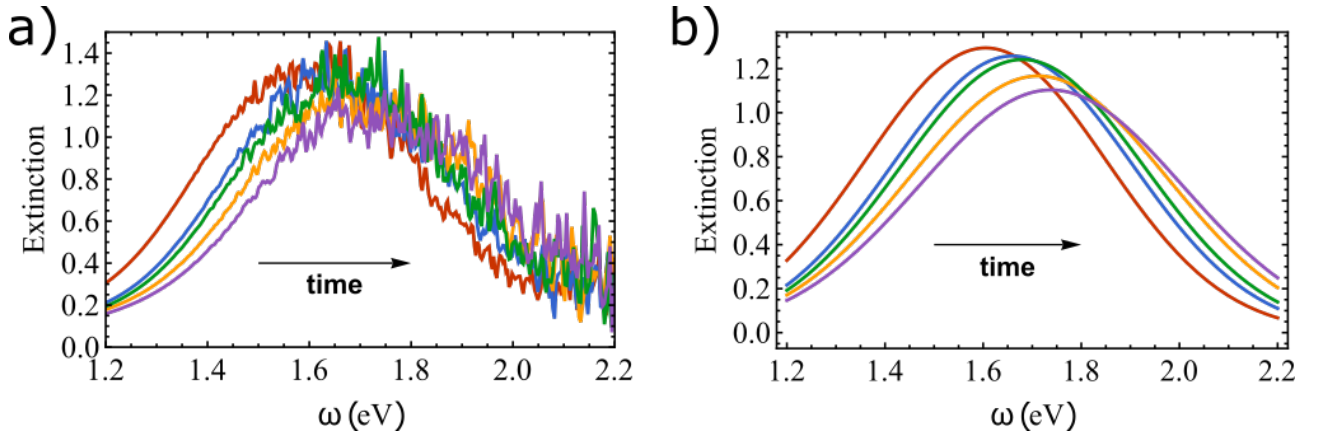
Figure 5.2: a) Several extinction spectra during thermal heating of an ensemble of NRs (sample TW010a2, $AR = 3.7 \pm 0.7$, $V = (2.2 \pm 0.8) \cdot 10^4$ nm^3, $Au_{43}Ag_{57}$) at $T = 245\,^\circ$C. b) The Gaussian fits to the spectra in a).

want to study one of the two, in this case the alloying process. This distinction can be made because the processes happen at different time scales. The alloying process for the temperatures between 225 and 300 $^\circ$C takes between six hours and several days, while deformation for Au NRs in mesoporous silica happens in about an hour.[96] It is therefore possible to fit the measured peak positions to a bi-exponentially decaying function from which time constants can be extracted. The used function to fit the peak position shift $\Delta\lambda$ is

$$\Delta\lambda = A + Be^{-t/\tau_{deform}} + Ce^{-t/\tau_{alloy}} \tag{5.3}$$

where A, B and C are fit constants and τ_{deform} and τ_{alloy} represent the time needed for the shape deformation and the alloying process respectively. The time constants τ_{deform} and τ_{alloy} indicate the time for which 63.2% of the peak shift associated with the process happened. By choosing suitable heating temperatures we can decouple shape deformation and alloying, as demonstrated in Figure 5.4. We can then use the time constant τ_{alloy} as an indication of how long the alloying process takes at a certain temperature. By employing this method for different temperatures for the same sample, the dependence of the alloying time on temperature can be extracted. We can define a diffusion coefficient D of the atoms in the particle migrating in three dimensions as[90]

$$D = \frac{r^2}{6t} \tag{5.4}$$

where r is the particle radius and t is the timescale for which an atom diffuses over the radius of the particle, which is proportional to τ_{alloy}. We use $t = \tau_{alloy}$ to calculate the diffusion coefficient. Because τ_{alloy} only represents the time for which 63.2% of the alloying has occured, the actual time for alloying t could be higher, meaning our calculated diffusion coefficients D could be overestimated. The diffusion coefficients D for different temperatures can be fitted using the Arrhenius equation

$$D = D_0 e^{-E_A/k_B T} \tag{5.5}$$

from which both the activation energy E_A and the frequency factor D_0 can be extracted including errors. An eventual overestimation of all diffusion coefficients D does not influence the activation energy. This procedure allows us to estimate how long it takes for certain shapes and sizes of core-shell NRs to alloy at low temperatures.
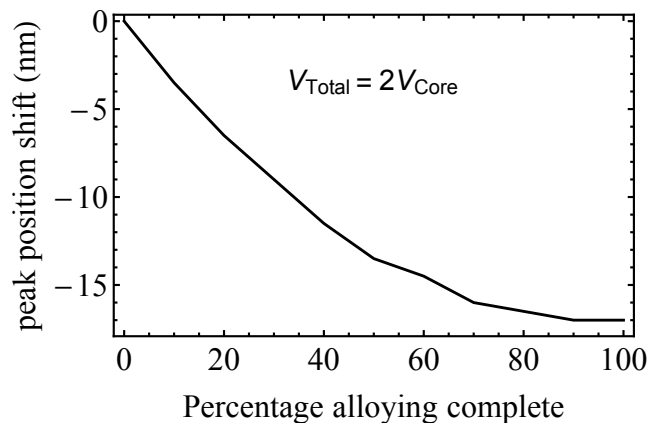

Figure 5.3: Predicted blue-shift of the plasmon resonance peak position when a 50/50 Au-Ag core-shell NR is alloying, calculated with Mie-Gans theory.
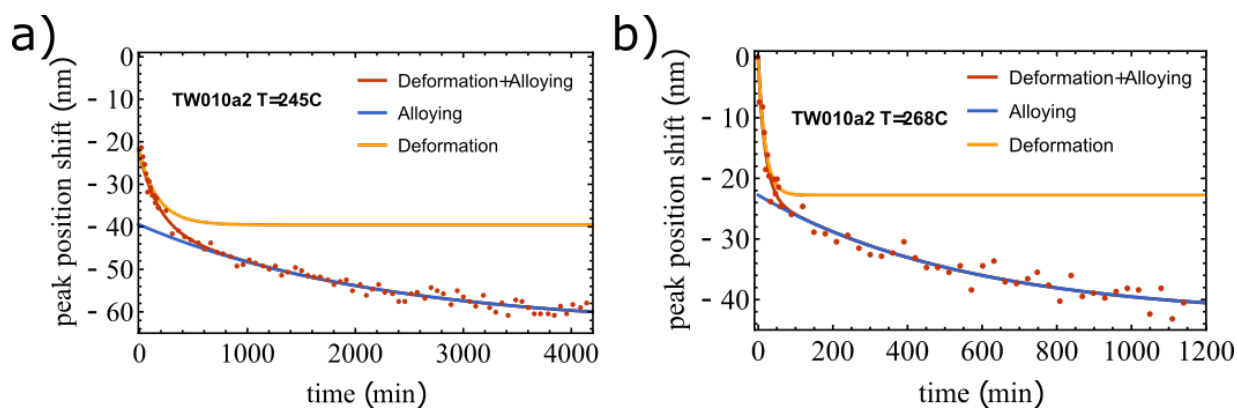
Figure 5.4: Peak shift of an ensemble of NRs (sample TW010a2, $AR = 3.7 \pm 0.7$, $V = (2.2 \pm 0.8) \cdot 10^4$ nm^3, $Au_{43}Ag_{57}$) during thermal heating at a) $T_{max} = 245\,°C$ and b) $T_{max} = 268\,°C$.

5.3.3 In-situ heating measurements in an electron microscope

In order to study the shape-dependence of the alloying process, we synthesized Au-Ag spheres and rods of the same composition and volume via the same procedure as described previously. The etching and Ag coating procedures for the Au-Ag spheres was the same as for the rods. The silica coated Au NRs were supplied by Jessi van der Hoeven, synthesized via the seeded growth method of Ye et al.[6] The Au nanospheres were synthesized by Naomi du Pree, via the the seeded growth method of Jana et al.[97] Both rods and spheres were silica coated via the method of Gorelikov and coworkers.[94] The sizes of both Au core and Ag shell of the NRs were characterized by TEM images, while HAADF-STEM images were used for spheres. By employing in-situ heating experiments in the electron microscope, we aimed to resolve if the alloying temperature for NPs of the same size and composition depends on the shape of the NP. The in-situ heating experiments were performed on a FEI Talos F200x operated at 200 kV, using a heating holder from DENSsolutions. The dispersion containing spheres was dropcasted on the Nano-Chip XT ($T_{max} = 1300\,°C$) and the dispersion with NRs was dropcasted on the Nano-Chip ST ($T_{max} = 800\,°C$). A heating chip was mounted on the heating holder, which could be inserted in the electron microscope. Once a suitable spot for EDX was located via BF-TEM and HAADF-STEM, the heating holder was connected to the heating control box. After an EDX measurement at room temperature, the temperature was increased by incremental steps of 50 °C. The temperature increase happened nearly instantaneously ($< 1\,s$). We kept the temperature constant for approximately 5 minutes after each temperature increase and looked with HAADF-STEM to check whether the core-shell structure was still intact. When we saw the core-shell contrast changing we performed an EDX measurement. Each EDX map was accumulated for 5 minutes. Thus each EDX measurement increased the duration for which the sample was heated at that temperature by 5 minutes. We performed EDX measurements at room temperature, 350 °C and 400 °C for both spheres and rods. After we observed complete alloying for the NPs in our chosen spot, we performed another EDX measurement on a different spot, to exclude any influence of the electron beam on the alloying process. The sample was then cooled down with temperature steps of 50 °C, with times below one minute between temperature changes. Another EDX measurement was taken when the sample was back at room temperature. The EDX maps were quantified via the Cliff-Lorimer method.

5.3.4 Laser heating

To look at single particle heating with a laser, we use a Leica SP8 confocal setup (63x/1.4NA oil-immersion confocal Leica objective). The setup is equipped with both a Coherent Chameleon II Ti:Sapphire laser (80 MHz repetition rate, 140 fs pulse length) and a fiber-based white light laser. We use a TECNAI-12 transmission electron microscope to characterize the NPs before and after laser irradiation. Finder grids were used. A droplet of the NP dispersion was dropcasted on a TEM finder grid and dried. Suitable areas of around $10 \times 10\,\mu m$ were located in the electron microscope. An overview image was taken in order to be able to locate that area again. Single NPs in that area were then imaged more closely in order to determine its core-shell structure before laser irradiation. After TEM imaging, the grid was placed on a microscopy slide. A droplet of glycerol was put on top of the grid to minimize the scattering of the silica shell (refractive index of 1.45). The refractive index of glycerol is also close to that of the microscopy glass and immersion oil (refractive index of 1.51). A 0.1 mm thick cover glass was placed on top of the grid. This sample system was then placed in the confocal setup. We used the white light laser at 480 nm in reflection mode (collected between 470 and 490 nm) to find back the spot we chose in the electron microscope and to focus onto the right z-plane. This was done by maximizing the signal collected from the height of the polymer film of the TEM grid. We used the Ti:Sapphire laser at 860 nm, close to the plasmon resonance of the used sample, and scanned through z for 4 μm higher and lower than the focal plane. This was done to ensure that all NRs were excited by the laser. The x-y area used was around $10 \times 10\,\mu m$. The total time the of laser illumination was around one minute, ensuring enough laser pulses hit the sample. After laser irradiation the TEM grid was removed from the glass slide. The grid was dried in a vacuum chamber overnight in order to remove the glycerol. The irradiated spot

was imaged again in the TEM. This allowed us to compare the same particle before and after laser irradiation.

5.4 Results & Discussion

5.4.1 Core-shell nanorods: synthesis & characterization

Three samples of silica-coated Au-Ag core-shell NRs that were used for alloying are characterized here. They demonstrate that different core and shell sizes can be synthesized by using the protocol in the methods section. We will look at the TEM images and extinction spectra of these samples.

First, a selection of BF-TEM images taken is shown in Figure 5.5. They are used to determine the width, length, aspect ratio and volume of both the Au core and the Ag shell. The Au core and Ag shell can be distinguished due to a difference in mass-thickness contrast. This is because Au has an atomic mass of 197 amu, compared to 108 amu for Ag. The intensity in a BF-TEM image due to mass-thickness contrast is given by $I = I_0 e^{\sigma t}$, where t is the thickness and σ the material-dependent scattering cross-section, which depends on the mass of the material. The contrast between the Au core and Ag shell would have been more clear in HAADF-STEM mode, as Z-contrast depends on the atomic number Z (79 for Au and 47 for Ag) and the intensity scales with Z^2. However, independent imaging on more advanced electron microscopes was beyond the scope of this master thesis. It is important that the geometrical characterization from BF-TEM images is done by only measuring NPs that have a clear core-shell structure. Knowledge of other forms of contrast formation, mainly diffraction contrast due to crystal structure orientation, and imperfect imaging, for example due to objective aperture placement, helps to determine which imaged particles have clear core-shell structures and which particles look different due to imaging artifacts. The width and length of both the core and the total particle were measured for 50-100 particles for each sample. The mean and standard deviation of geometrical quantities for samples TW009a2, TW010a2 and TW010a4 are given in Table 5.1, 5.2 and 5.3, respectively. The standard deviation is not due to errors in the measuring of width and length, but rather because of polydispersity in the sample. The Au/Ag ratios of these samples were 75/25, 43/57 and 33/67 respectively.

TW009a2	d (nm)	σ_d (nm)	l (nm)	σ_l (nm)	V (10^3 nm^3)	σ_V (10^3 nm^3)	AR	σ_{AR}
core	16.3	2.1	50.9	11.9	9.9	4.0	3.1	0.7
total	17.8	2.2	54.0	12.3	12.7	5.6	3.1	0.5

Table 5.1: Mean geometrical parameters and their standard deviation determined for sample TW009a2 by measuring length and width for individual NPs in TEM images. The amount of NPs measured was 145.

TW010a2	d (nm)	σ_d (nm)	l (nm)	σ_l (nm)	V (10^3 nm^3)	σ_V (10^3 nm^3)	AR	σ_{AR}
core	13.7	1.7	68.7	14.8	9.7	3.7	5.1	1.1
total	20.1	2.3	74.9	15.0	22.3	8.1	3.7	0.7

Table 5.2: Mean geometrical parameters and their standard deviation determined for sample TW010a2 by measuring length and width for individual NPs in TEM images. The amount of NPs measured was 48.

TW010a4	d (nm)	σ_d (nm)	l (nm)	σ_l (nm)	V (10^3 nm^3)	σ_V (10^3 nm^3)	AR	σ_{AR}
core	13.5	1.8	72.7	16.5	10.8	4.3	5.4	1.4
total	22.7	3.3	79.9	16.1	30.5	13.5	3.6	0.7

Table 5.3: Mean geometrical parameters and their standard deviation determined for sample TW010a4 by measuring length and width for individual NPs in TEM images. The amount of NPs measured was 45.

It is not just the geometrical parameters that are interesting for these samples. The ensemble extinction spectrum was used to characterize the optical properties of the sample. It also allows us to test the Mie-Gans modelling of core-shell NPs. We do this by calculating the extinction cross section of a single core-shell particle, in a silica shell with 63% porosity,[98] for each sample with the mean parameters given in Table 5.1, 5.2 and 5.3. The measured ensemble spectra and the by Mie-Gans theory calculated single particle spectra are given in Figure 5.6. The porosity of the silica shell was included in the dielectric environment by calculating the dielectric constant of the medium via Equation 2.33 given in chapter 2. The samples of the measured ensemble spectra are 2 times diluted compared to the core AuNRs@mesoSiO$_2$ before Ag deposition which had an Absorbance of 2. Therefore, the initial core dispersion had an Absorbance of 1. For sample TW009a2, the Absorbance is 1.3 and has thus increased by a factor 1.3. This is explained by the volume increase due to Ag deposition, which is also a factor 1.3, since, besides size-dependent damping effects like radiation damping, the plasmon resonance intensity scales linearly with volume. The aspect ratio and the polydispersity of the cores and the
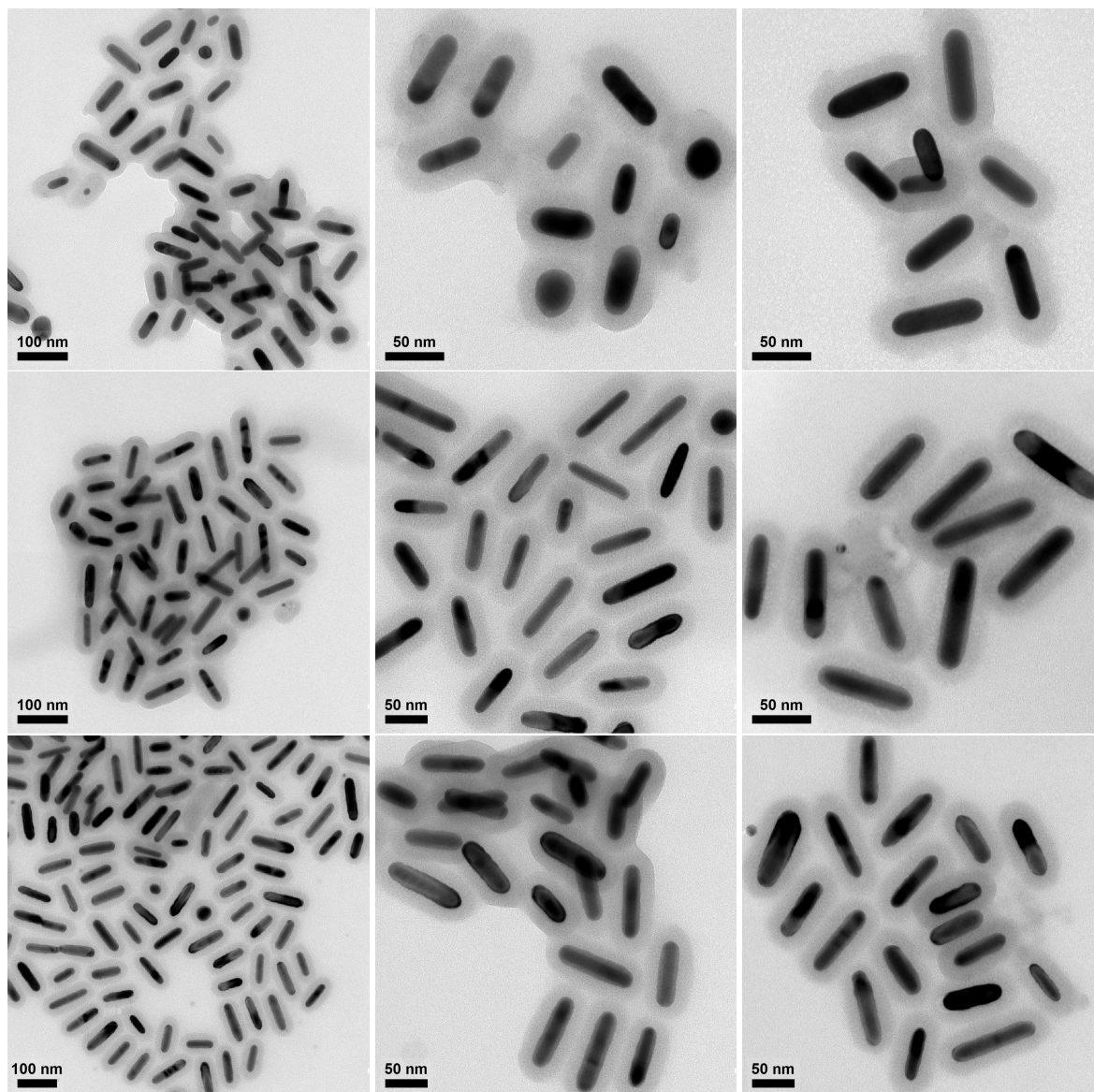
Figure 5.5: BF-TEM images of sample TW009a2 (top row), TW010a2 (middle row) and TW010a4 (bottom row). TEM images were taken on the FEI Tecnai-12. The somewhat large circular objects in the figures are most likely spheres, as the synthesis produces a few spheres as well.

total particle hardly differ. This means the only parameters affecting the change in Absorbance are the volume and the composition of the NRs. Because the difference in Absorbance between the Au core NRs solution and Au-Ag core-shell NRs solution can be explained by the increase in volume of the particles, it is likely that the properties of the Au-Ag core-shell NRs are not significantly better than a Au NR of the same volume. This is not trivial as Ag has better plasmonic properties than Au in the wavelength regime of the plasmon resonance. The better properties of Ag are likely cancelled out by the collective electron oscillation undergoing dephasing by scattering of the interface between the Au core and Ag shell. This mechanism was also proposed to explain the larger homogeneous broadening of single Au-Ag core-shell NR spectra compared to Au NR spectra in dark-field scattering experiments by Liu et al.[33] For the samples TW010a2 and TW010a4, the Absorbance increased with a factor 1.5 and 2 compared to the core spectra, respectively. For both these samples, the increase in extinction is less than the average increase in volume. This is mostly caused by a decrease in aspect ratio, which lowers the plasmon resonance intensity, as shown in chapter 2.

The by Mie-Gans theory calculated single NR spectra and the measured ensemble spectra show good agreement in terms of peak position (Figure 5.6). Calculations and measurements are in good agreement on peak positions. The most obvious difference between the calculated and measured spectra are the relative peak intensities. For sample TW009a2, the measured ensemble spectrum has a much higher relative peak intensity compared to the other two samples than the calculated single particle spectrum of TW009a2. For example, the peak intensity of the measured extinction spectrum for sample TW009a2 is 0.86 times the intensity of sample TW010a2, whereas for the calculated single particle spectra the peak intensity for TW009a2 is only 0.37 times that of TW010a2. This is due to the fact that the aspect ratio polydispersity for TW009a2 is lower than for the other two samples. The sum of all the single particle spectra making the ensemble spectrum is thus more concentrated in a small wavelength regime for sample TW009a2 than for the other two. This leads to a higher relative peak intensity in the ensemble spectrum. This shows the importance of the aspect ratio polydispersity in ensemble spectra, as discussed in chapter 4.
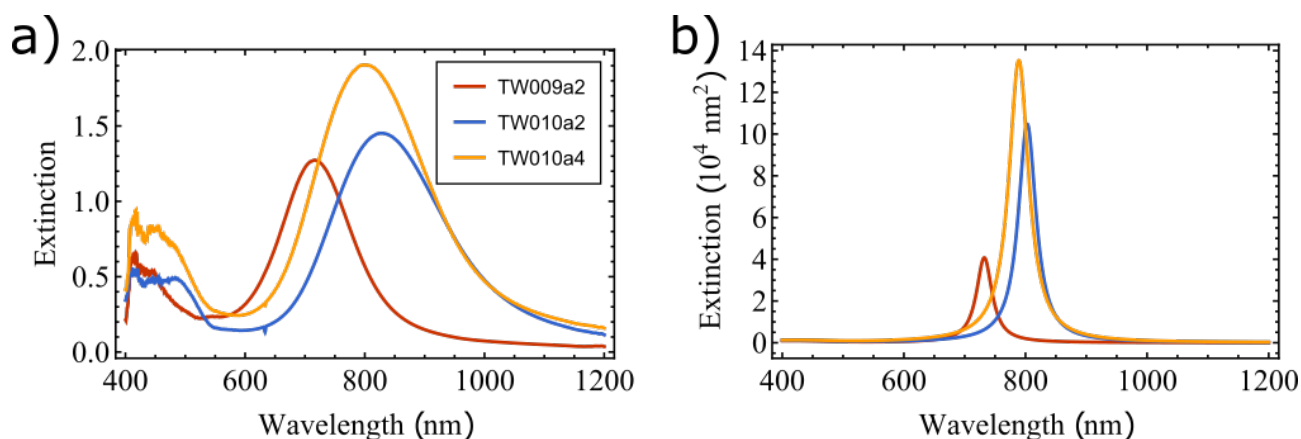

Figure 5.6: Extinction spectra for three different silica-coated core-shell NR samples in water. a) The measured spectra and b) calculated spectra for one NR with the mean properties show good qualitative agreement in relative peak position. The measured ensemble spectra were measured using and FTIR and the calculated single particle spectra were calculated using Mie-Gans theory.

5.4.2 In-situ heating measurements with extinction spectroscopy

The alloying process was followed in-situ with extinction spectroscopy by using the knowledge of the theoretical peak shift of the plasmon resonance of NPs with the same composition that change from a core-shell structure to a fully alloyed structure. The plasmon resonances of these NPs can easily and quickly be calculated by Mie-Gans calculations. The peak shifts towards the blue part of the spectrum when the core-shell NP changes towards an alloyed NP (Figure 5.3). Therefore, in-situ extinction spectroscopy measurements are performed to follow the alloying process.

A first important check is to determine whether core-shell NRs alloy at the temperatures employed here. We compare TEM images of NRs of average aspect ratio 3.78 and a 43/57 Au/Ag ratio before and after elevated temperature in the Linkam cell. The sample was heated in the Linkam cell for 16 hours at $T = 300°C$ and from Figure 5.7 it is clear that the core-shell structure was a lot more vague even for the NPs that were not completely alloyed. This first result shows it is possible to alloy at these temperatures as long as the sample is at elevated temperature for a long time period. This is remarkable, since Gao et al. found that they required a temperature of $930°C$ to fully alloy Au-Ag nanospheres that have 3 to 4 times smaller volumes.[88] The reduced alloying could be ascribed a shape effect, which we study in more detail later. Figure 5.7 also confirms that the aspect ratio decreases only slightly. For this particular sample the average aspect ratio decreased from 3.78 to 3.48. Before heating the aspect ratios of 120 particles were measured, whereas this was done for 60 particles after heating, since less particles were deposited on the TEM grid due to difficulties in redispersing them.
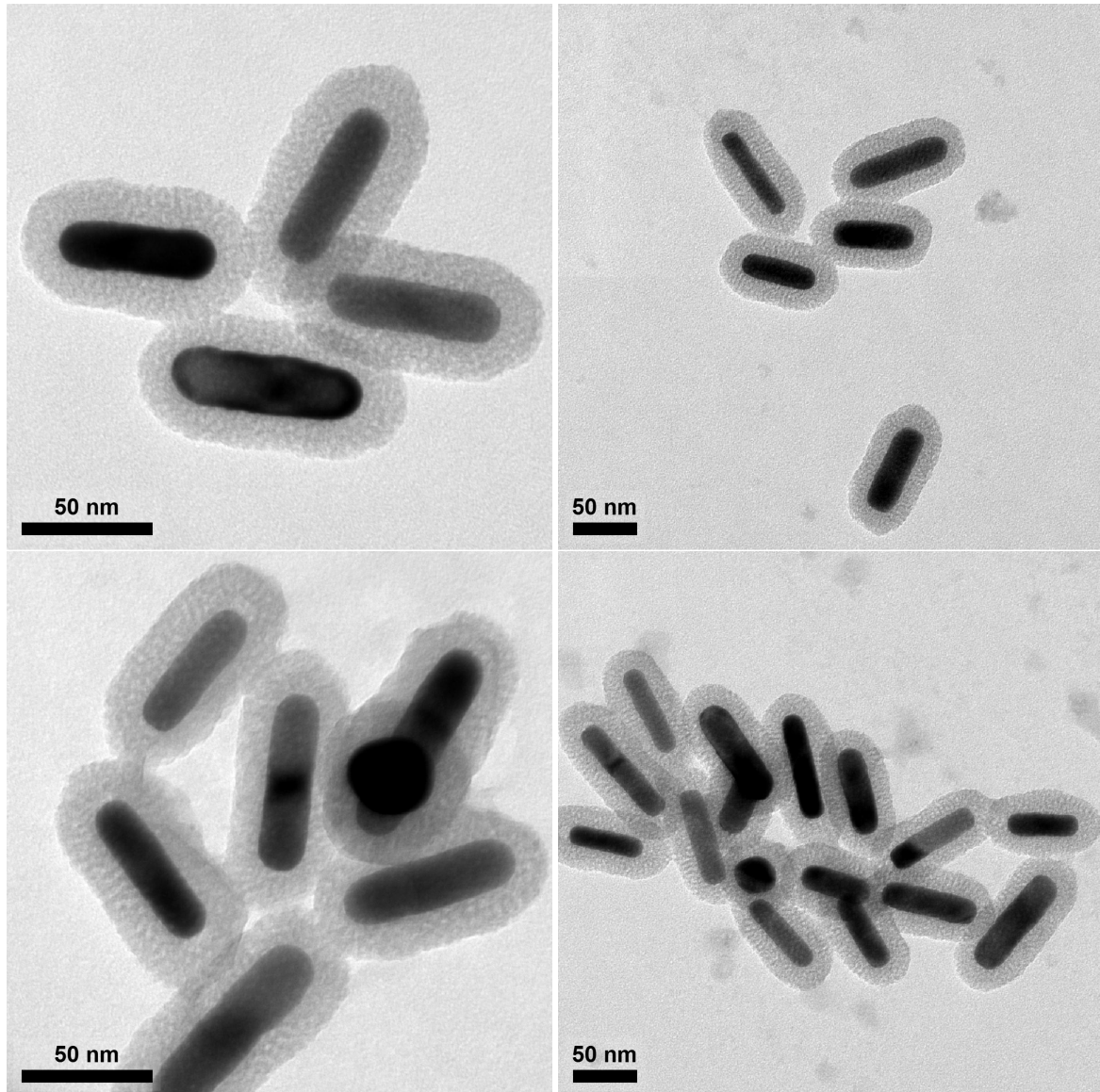
Figure 5.7: Transmission electron microscopy images taken on the TECNAI-12, showing a less clear core-shell structure for NRs of a 50/50 Au/Ag ratio (sample TW010a2) after heating at $T = 300\,^{\circ}C$ for 16 hours.

As we established that it is possible to alloy the NRs at relatively low temperatures we used the analysis described in section 5.3.2 to link peak position shifts in the FTIR measurements to typical alloying times. We extracted diffusion coefficients for three different samples and use the Arrhenius equation to obtain activation energies for atoms in the alloying process.

We investigated three different samples, namely TW009a2, TW010a2 and TW010a4, which are characterized in Table 5.4. The three samples have different average aspect ratios, various Au/Ag ratios and slightly different volumes. The extracted activation energies are also given for each sample. The diffusion coefficients and Arrhenius fit for TW009a2, TW010a2 and TW010a4 are shown in Figure 5.8, 5.9 and 5.10, respectively. It needs to be mentioned that the spectra for the sample with the lowest AR NRs, TW009a2, are generally more noisy due to the detector limit, which makes the Gaussian fits to these spectra less reliable. This results in high errors for the diffusion coefficients in Figure 5.8. Both the activation energy E_A and the frequency factor D_0 can be acquired from the least-square Arrhenius fit to the data in Figures 5.8, 5.9 and 5.10. The error for the frequency factor, however, is large, namely of the order of the frequency factor itself, so nothing meaningful can be concluded from it, in contrast to the activation energy.

sample	$\overline{AR}$	$\overline{D}$ (nm)	$\overline{V}$ (10^4 nm^3)	Au_xAg_y	E_A (eV)
TW009a2	2.7	23.7	2.5	$Au_{75}Ag_{25}$	0.9 ± 0.1
TW010a2	3.4	19.9	1.9	$Au_{43}Ag_{57}$	0.6 ± 0.1
TW010a4	3.2	23.0	2.7	$Au_{33}Ag_{67}$	0.7 ± 0.1

Table 5.4: Investigated samples and their corresponding average aspect ratio after heating $\overline{AR}$, average width after heating $\overline{D}$, average volume after heating $\overline{V}$, Au/Ag ratio Au_xAg_y and activation energy E_A.
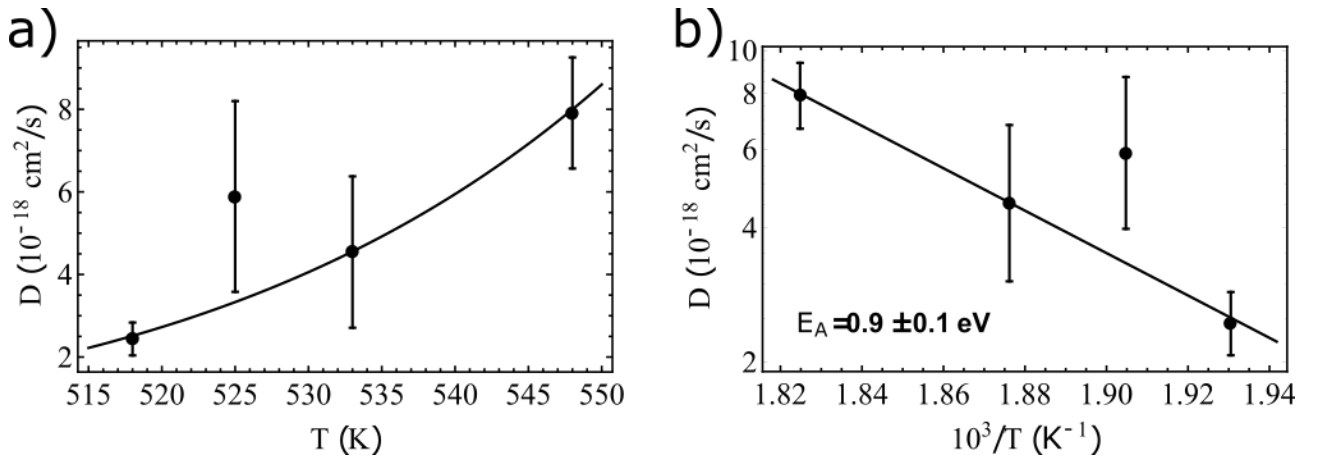

Figure 5.8: Diffusion coefficients D of sample TW009a2 for four different temperatures related via the Arrhenius equation shown in a) a regular plot and b) an Arrhenius plot. The least-square fit of the Arrhenius equation for these points is shown as the black line. The slope of the line in the Arrhenius plot corresponds to the activation energy E_A.
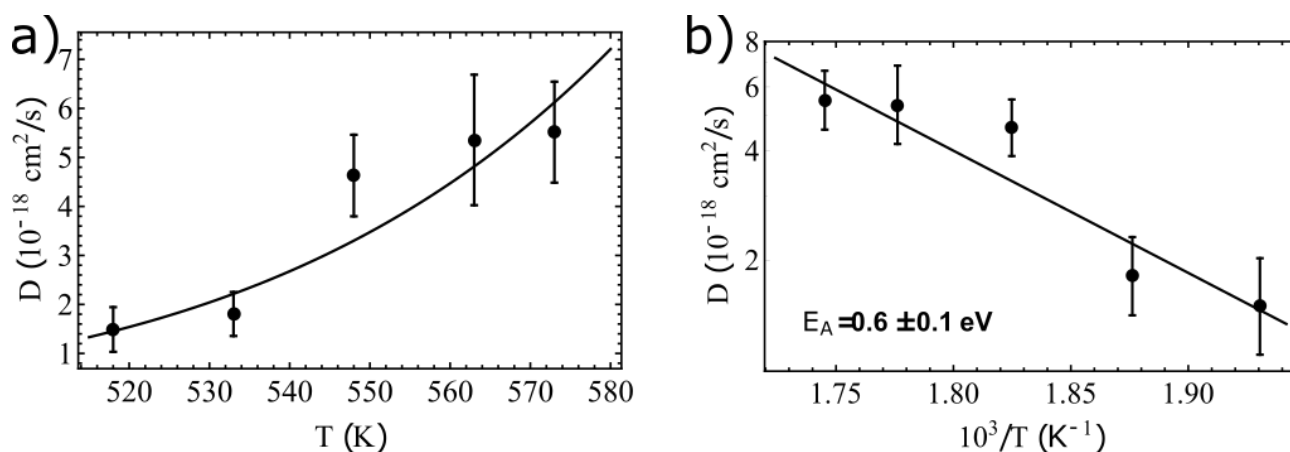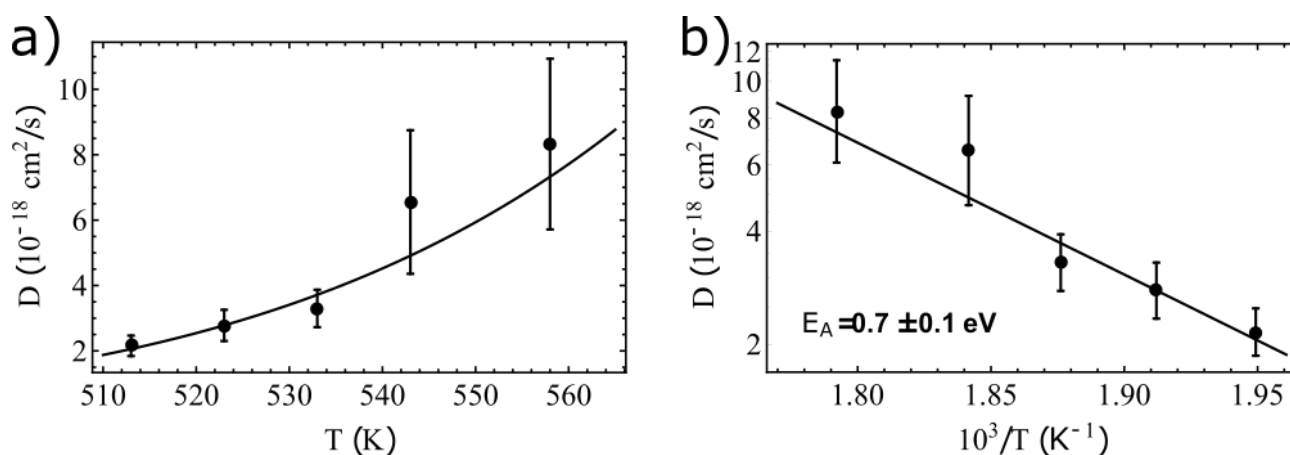
Figure 5.9: Diffusion coefficients D of sample TW010a2 for five different temperatures related via the Arrhenius equation shown in a) a regular plot and b) an Arrhenius plot. The least-square fit of the Arrhenius equation for these points is shown as the black line. The slope of the line in the Arrhenius plot corresponds to the activation energy E_A.

Figure 5.10: Diffusion coefficients D of sample TW010a4 for five different temperatures related via the Arrhenius equation shown in a) a regular plot and b) an Arrhenius plot. The least-square fit of the Arrhenius equation for these points is shown as the black line. The slope of the line in the Arrhenius plot corresponds to the activation energy E_A.

In the following we will discuss the influence of parameters such as Au/Ag ratio, size and shape on the activation energy by analyzing the results for the three samples characterized in Table 5.4. Unfortunately, the vacancy concentration on the interface between the Au core and Ag shell could not be investigated. The core-shell NPs are all synthesized in the same way, so the vacancy concentration should be relatively similar. However, small deviations in composition, size and shape may induce vacancy concentration differences, particularly due to different interface curvatures. To study the influence of vacancies on the alloying process is beyond the scope of this thesis. Molecular dynamics simulations could be employed to study the influence of vacancies on the activation energy.

Firstly, we investigate the influence of volume on the activation energy. As shown in Table 5.4, the three samples have very similar volumes, roughly equivalent to the volume of a sphere with a diameter of 35 nm. The volumes are much larger than the typical volumes for which the melting point of nanostructures becomes size dependent.[92, 99–102] For Au-Ag alloys, the nanophase diagram was shown to be only mildly size-dependent for spherical NPs with diameters of 35 nm.[100] Dick et al. showed that the diffusion coefficients were size-dependent for Au spheres with diameters below 20 nm.[92] The widths of the NRs of the samples used, as shown in Table 5.4, are above 20 nm. We therefore conclude that the small differences in volume for the NPs in our samples are insufficient to explain the differences in activation energy.

To determine the influence of aspect ratio and Au/Ag ratio on the activation energy, we plot the activation energy versus both the aspect ratio and Au/Ag ratio in Figure 5.11. The sample with the lowest aspect ratio and highest fraction of Au atoms has the highest activation energy. We can estimate an upper limit for the influence of the Au/Ag ratio on the activation energy by calculating the bulk activation energies for the Au/Ag ratios of our NPs and compare them. We do this for the extreme case in which we assume that Ag atoms only diffuse into a Au atom environment and vice versa. This gives an upper limit for the influence of the composition on the activation energy, as values for the activation energies for diffusion of Au and Ag atoms in bulk alloy compositions are more similar than Au diffusing in Ag and vice versa.[91]
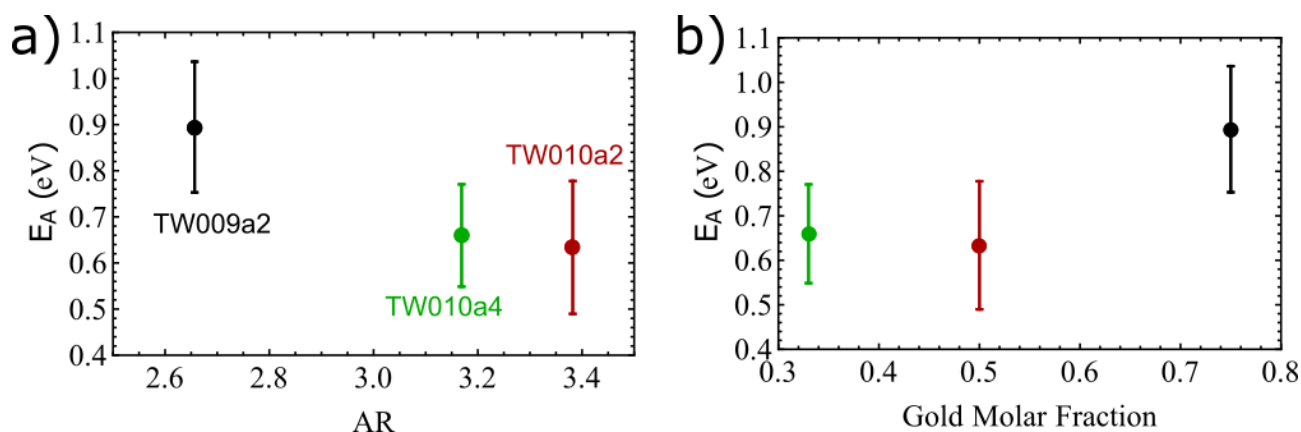
Figure 5.11: Activation energy E_A for three different samples as determined from Figures 5.8, 5.9 and 5.10. The activation energies E_A are plotted as function of a) aspect ratio and b) gold molar fraction.

We estimate the bulk activation energies as $E_A \approx x_{Au}E_{A,Au-Ag} + x_{Ag}E_{A,Ag-Au}$, where $E_{A,Au-Ag}$ is the activation energy for a Au atom diffusing into an environment with Ag atoms and $E_{A,Ag-Au}$ the activation energy for a Ag atom diffusing into Au. For the composition $Au_{33}Ag_{67}$, the in this way calculated bulk activation is 6% higher than the bulk activation energy calculated for the composition $Au_{75}Ag_{25}$. Because the errors for the activation energies in Figure 5.11 are large, the influence of the composition cannot be excluded, but the theoretical upper limit of the influence of the composition on the activation energy is minor.

This leaves the shape of the particle, presented as an aspect ratio difference in Figure 5.11, as the cause for the higher activation energy of the sample with low aspect ratio NRs. There are various other ways the shape can have an influence on the activation energy. For example, the aspect ratio of the initial core could influence the diffusion process. Differences in shape also lead to different interface areas and interface to volume ratios which could speed up the alloying process. However, with so few points it is hard to deduce any effect of the shape on activation energy. We hypothesize that larger interface areas and a higher Au ratio do have a minor influence the activation energy, but the exact nature of these dependencies cannot be extracted from the data. In any case, no large influence of shape on the activation energy was observed.

5.4.3   In-situ heating measurements in the electron microscope

The samples of spheres and rods used in this experiment are characterized in Table 5.5 and 5.6, respectively. Figure 5.12 and 5.13 show EDX maps for the nanospheres and nanorods, respectively, at several stages during the heating process in the electron microscope. It was observed that the onset of the alloying process was at T=350 °C for both the nanospheres and the nanorods. For both spheres and rods, the core still consisted mainly of Au, but the core-shell structure became less pronounced. As we saw in section 5.4.2, the heating time is important in the alloying process. This found onset for alloying is therefore no strict threshold, but rather the first temperature for which we observed a change in the core-shell structure within the five minutes that we measured. When the temperature was increased to 400 °C, the nanospheres and the nanorods were both alloyed, as the EDX maps showed that the Au and Ag was homogeneously distributed throughout the NPs. No difference in alloying temperature was thus observed for nanospheres and nanorods of similar volume and Au/Ag ratio. To determine whether the NPs remained alloyed when the temperature was returned to room temperature, a final EDX measurement was done. Figures 5.12 and 5.13 show that the metals were still homogeneously distributed within the NPs at room temperature, indicating the stability of the alloy.

In order to exclude any influence of the electron beam on the alloying process, we visualized a previously unexposed area for comparison for both spheres and rods in Figure 5.14. The particles in this area were also alloyed, which means the electron beam did not promote the alloying of the particles. It needs to be noted that for the NRs, we only checked an unexposed spot at 500 °C, which was 100 °C above the alloying temperature observed in the initial spot.

NDP-003-A2 (spheres)	D (nm)	V (10^3 nm^3)	S/V (nm^{-1})
core	18.3 ± 2.1	3.3 ± 1.1	0.33 ± 0.04
total	25.2 ± 2.6	8.6 ± 2.3	0.24 ± 0.02

Table 5.5: Characterization of the spheres used in this experiment. The table gives the diameter D, volume V and surface-to-volume ratio S/V for both the Au cores and the total core-shell NPs.
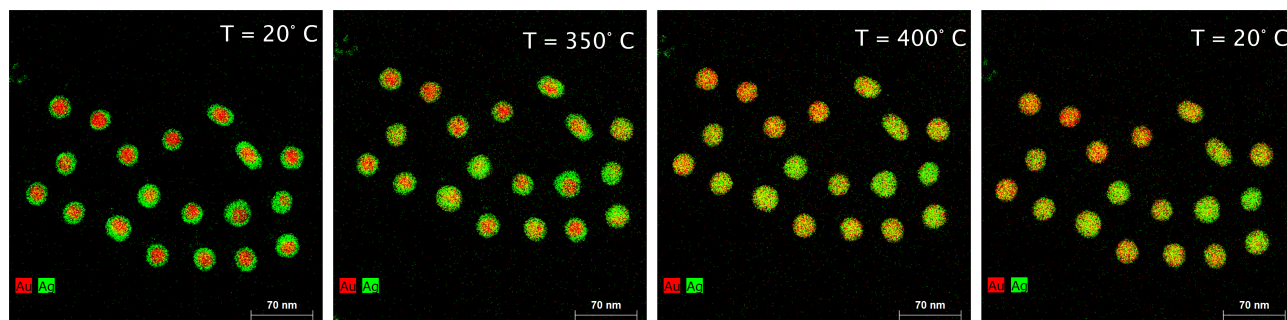
Figure 5.12: EDX maps during in-situ heating of silica coated Au-Ag nanospheres. The intensity EDX maps show the metal distribution of Ag (green) and Au (red) at different temperatures. The final EDX map shows the metal distribution after the temperature was decreased to room temperature.
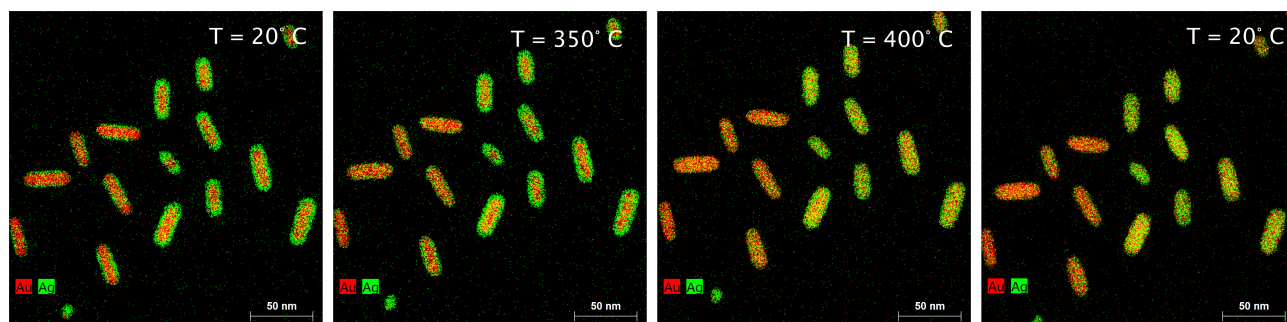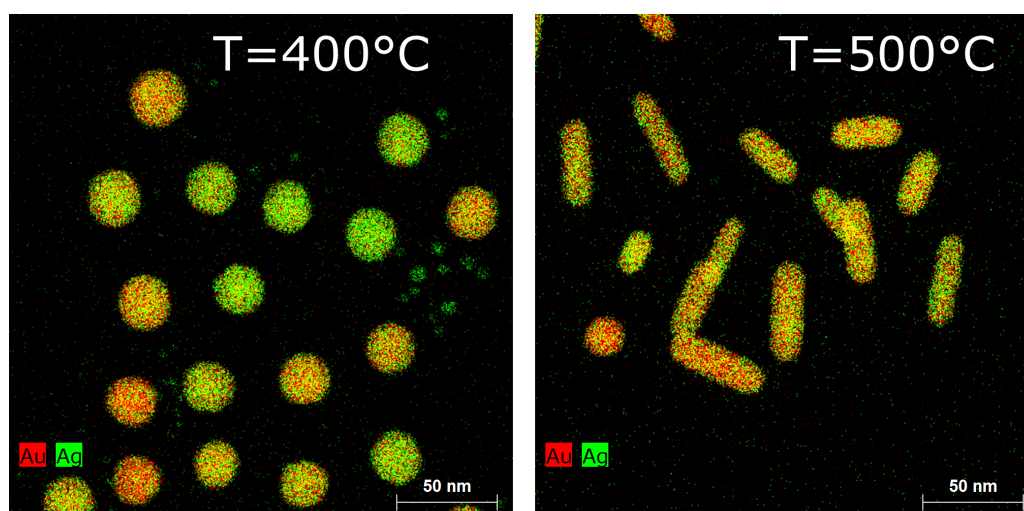

Figure 5.13: EDX maps during in-situ heating of silica coated Au-Ag NRs. The intensity EDX maps show the metal distribution of Ag (green) and Au (red) at different temperatures. The final EDX map shows the metal distribution after the temperature was decreased to room temperature.

Figure 5.14: EDX maps for spheres and rods at spots that were not exposed to the electron beam prior to this measurement. The intensity EDX maps show the metal distribution of Ag (green) and Au (red).

JVH-022-A2 (rods)	D (nm)	V (10^3 nm^3)	AR	S/V (nm^{-1})
core	10.8 ± 1.7	3.4 ± 1.4	3.6 ± 0.8	0.42 ± 0.06
total	16.5 ± 0.6	7.4 ± 3.6	2.9 ± 0.9	0.31 ± 0.05

Table 5.6: Characterization of the NRs used in this experiment. The table gives the diameter D, volume V, aspect ratio AR and surface-to-volume ratio S/V for both the Au cores and the total core-shell NPs.

Au$_x$Ag$_y$	T=20 °C	T=400 °C
spheres	Au$_{25}$Ag$_{75}$	Au$_{27}$Ag$_{73}$
rods	Au$_{36}$Ag$_{64}$	Au$_{36}$Ag$_{64}$

Table 5.7: The obtained atomic Au/Ag ratios Au$_x$Ag$_y$ for the EDX maps at room temperature and 400 °C for both spheres and rods.

The intensity maps before heating and at 400 °C for both spheres and rods were quantified by using the Cliff-Lorimer method. Only Au and Ag were used for the quantification while the other elements were used for deconvolution only. The quantified EDX maps are shown as atomic percentage EDX maps in Figures 5.15a) and 5.16a). The obtained atomic Au/Ag ratios averaged over all particles within the EDX map are presented in Table 5.7. The obtained Au/Ag ratios for spheres and rods remain constant at elevated temperature as expected.

The quantified EDX maps were used to extract line scans to quantify the positions of Au and Ag atoms within a particular particle. The line scans at room temperature and 400 °C for a sphere are shown in Figure 5.15b). It can be seen that at room temperature Ag is more prominent in the outer regions of the particle. At 400 °C the Ag and Au can both be found in all regions of the particle, which indicates an alloy structure. The line scans for a NR at room temperature and 400 °C are shown in Figure 5.16b-c). Both over the length and width of the studied particle the structure is easy to see. Before heating, there is a clear core-shell structure, while at 400 °C the particle is alloyed.
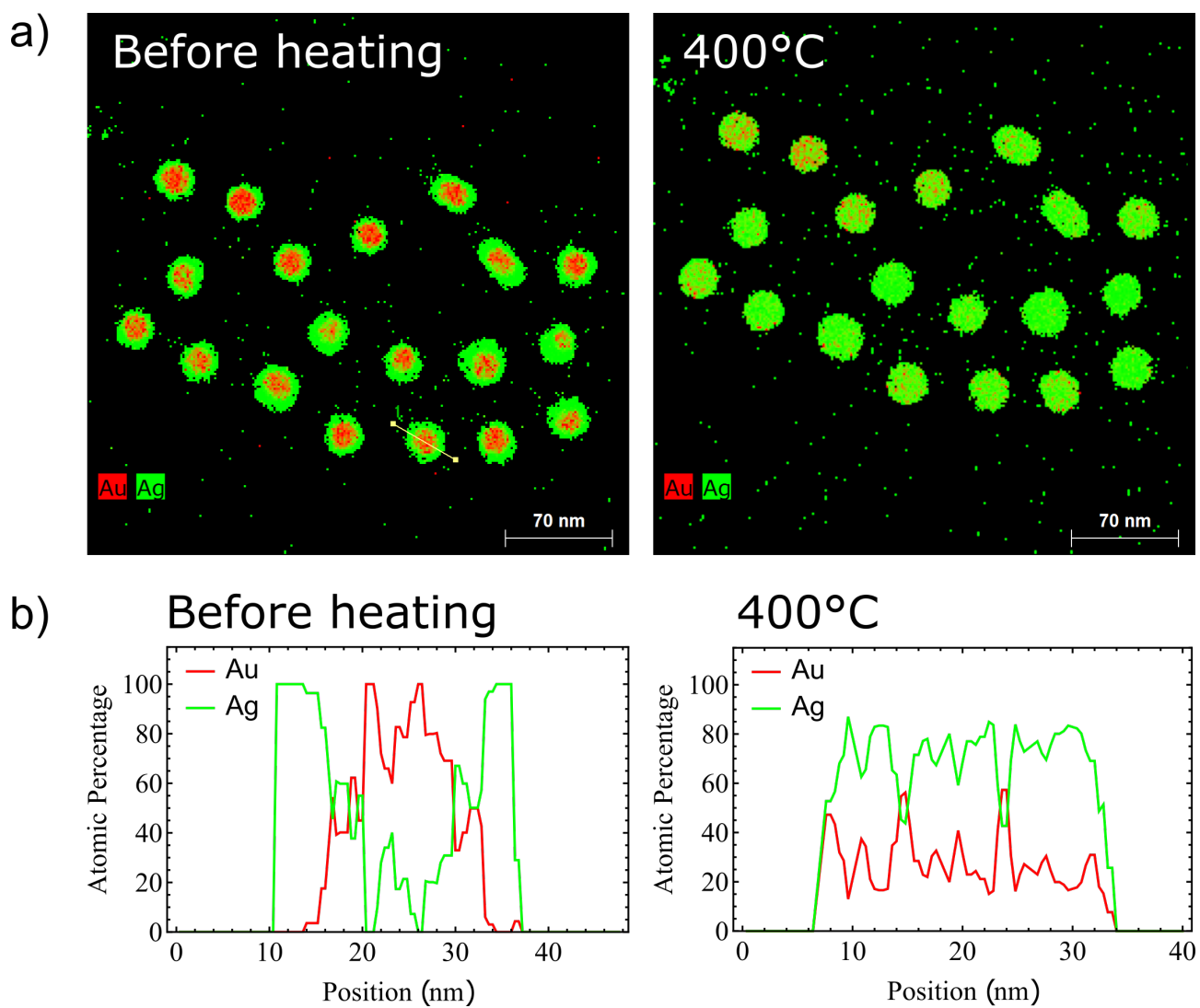
The difference in alloying temperature observed for spheres by Gao et al.[88] and rods by Albrecht and Van der Hoeven[25] was the motivation for this study. We therefore compare our results to theirs. The onset for alloying and final alloying temperature for spheres was found to be significantly lower than the temperature reported by Gao and coworkers.[88] Their spheres had volumes that were 1.5 times lower than the volumes of our spheres. A smaller particle size is expected to lower the alloying temperature, so size effects can be excluded. A possible explanation is the different method of defining the NP to be alloyed. Gao et al. used a wet-chemical procedure wherein the spheres were exposed to an etching solution of hydrogen peroxide and ammonia for a long time. The aqueous etchant-solution was composed of H$_2$O$_2$ (0.5 M), NH$_3$·H$_2$O (0.4 M), and PVP (surfactant, 0.5 wt%, M$_w$ = 10000). At 930 °C the decrease in intensity in the extinction spectrum was 18% within the first 24 hours, with no additional decrease in the next 20 hours, which they took as an indication of a fully alloyed nanosphere. This is in contrast to our spectroscopic technique, which provides information on the atomic distribution but lacks any information on chemical stability.

However, the alloy temperature we found for NRs does agree well with results from Albrecht and Van der Hoeven[25] who performed both our spectroscopic technique and exposure to an aqueous etching solution (1.7 vol% H$_2$O$_2$ and 0.9 vol% NH$_3$ solution) for two hours as analysis techniques on alloyed NRs. The NRs used in their in-situ heating experiment with similar time scales per temperature were found to have a higher alloying temperature of 450 °C, which is likely due to the larger volume of their NRs ($V = 3.7 \cdot 10^4$ nm^3, $AR = 3.0$), compared to our NRs ($V = 0.7 \cdot 10^4$ nm^3, $AR = 2.9$). Our NRs have diameters of approximately 16.5 nm, whereas the NRs of Albrecht and Van der Hoeven have widths of 27 nm.[25] Volume effects begin to influence the diffusion coefficient below sizes of 20 nm diameter for Au spheres.[92] The size-dependent diffusion coefficients and the larger distances that atoms in larger particles need to cover to alloy fully, makes it reasonable that they find a slightly higher alloying temperature for their NRs.

5.4.4   Laser heating

We showed that it is possible to alloy Au-Ag core-shell NPs by thermal heating in the previous two sections. Hodak et al.[103] alloyed Au-Ag core-shell nanospheres by using lasers with 5 ns and 30 ps pulses. In this section we heat Au-Ag core-shell NRs stabilized with a mesoporous silica layer using femtosecond laser pulses. The laser excites the LSPR of the NR. The excited electrons lose part of this energy via electron-phonon scattering. The typical electron-phonon coupling time for Au and Ag NPs of our size is around 1 ps.[104] The loss of energy via electron-phonon scattering heats up the particle,[105] which should enable the diffusion of Au and Ag atoms in order to form an alloy. This heat then diffuses into the medium, which is expected to happen on a 100-200 ps timescale,[103] or longer depending on the medium[105].

We used sample TW010a2 characterized in Table 5.2 to do the experiment. A laser fluence of 8.1 mJ/cm^2 was used. Figure 5.17 shows NPs before and after laser irradiation. We observed a loss of volume after we applied laser power to the sample. The volumes before and after laser irradiation are estimated from the length and widths of the particles in

Figure 5.15: a) Quantified EDX maps for spherical NPs. b) Line scans over the diameter of a spherical NP at room temperature (left) and 400 °C (right).
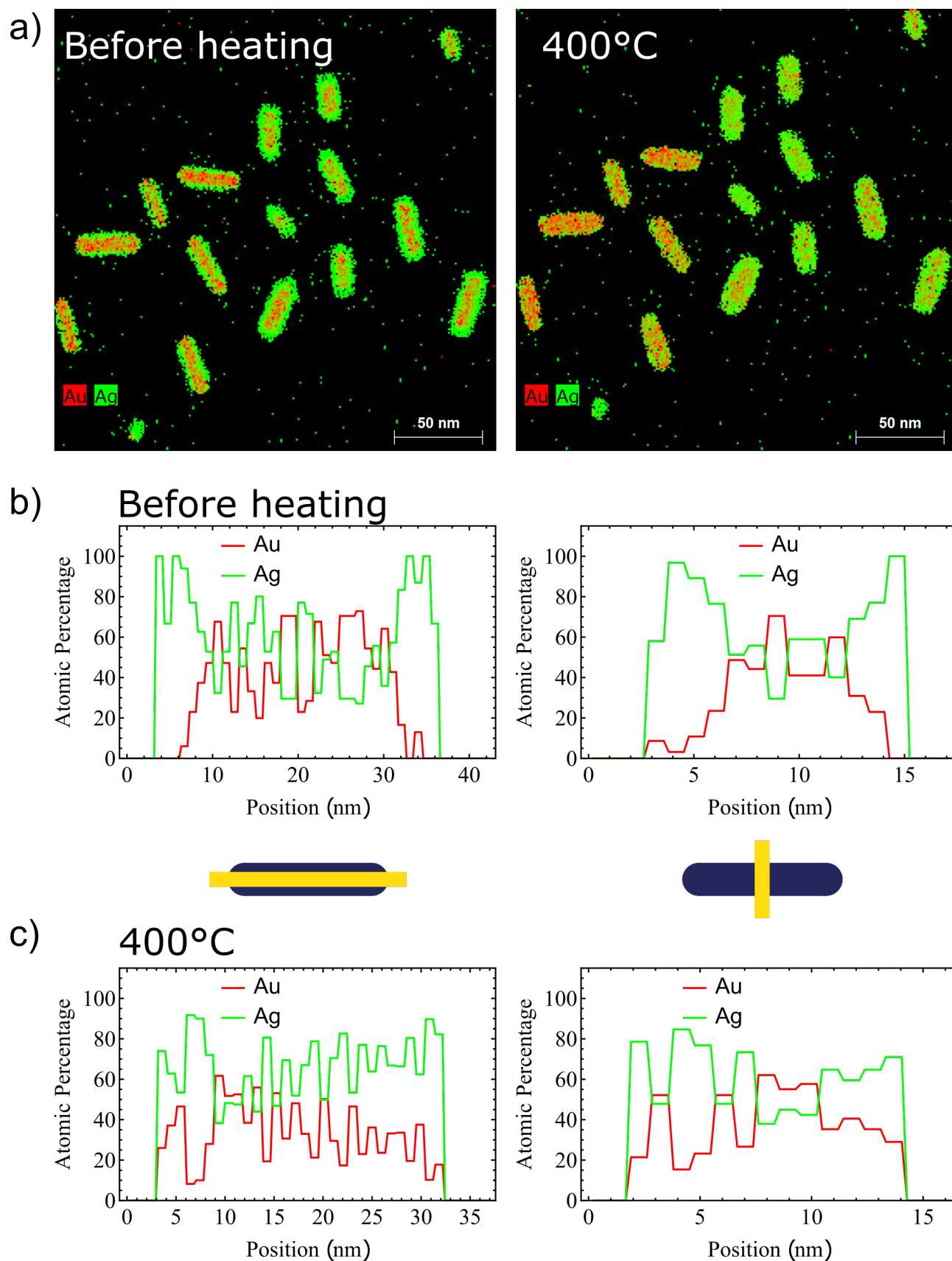
Figure 5.16: a) Quantified EDX maps for NRs at room temperature and 400 °C. b) Line scans over the length and width of a NR at room temperature. c) Line scans over the length and width of a NR at 400 °C.
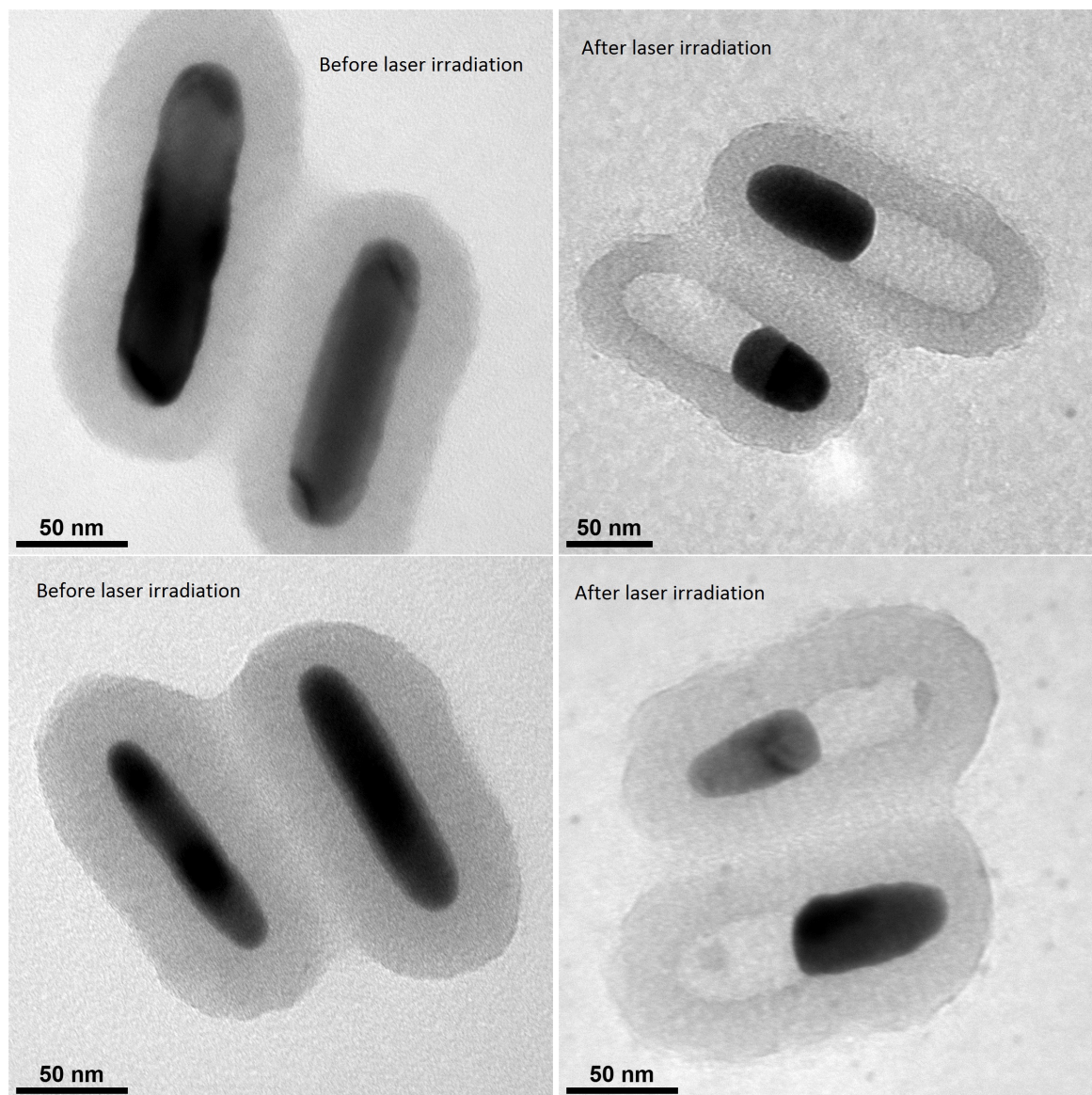
Figure 5.17: The same particles before (left) and and after laser irradiation (right). A laser fluence of 8.1 mJ/cm^2 was used. It looks like silver has escaped the particles, meaning alloying did not take place.

Figure 5.17 in Table 5.8. This is just an estimation, because the TEM images are a 2D projection of the sample. While it is true that the NRs deform due to the influence of the laser, this should not result in a volume loss. Albrecht et al. did not observe a volume loss after applying laser pulses with a fluence of 8.1 mJ/cm^2 on Au NRs in mesoporous silica shells.[105] Their Au NRs had an average volume of $(9.9 \pm 0.4) \cdot 10^4$ nm^3, which is larger than the volume of our core-shell NRs, which means our NRs should be more stable due to faster heat dissipation for smaller NPs. This leads us to believe that the volume loss is caused by Ag departing the particle as was observed for thermal heating of Au-Ag core-shell NRs in air.[25] The mechanism of the way in which the Ag leaves the particles is still unclear. Hodak et al. did not observe a volume loss for their laser-induced alloying of Au-Ag nanospheres.[103] Their particles were synthesized via radiation chemistry, while our particle are synthesized via wet chemistry methods.[6,94,95] As a result of our synthesis Cetyl trimethylammonium bromide (CTAB) is present in the pores of the silica shell. CTAB has a melting point between 237 and 243 °C. When this melting point is reached and oxygen is present an exothermic reaction can occur. The extra local heat when CTAB burns, due to the oxygen present, may be the cause for Ag escaping from our particles as the particles used by Hodak et al. did not contain CTAB. However, the temperatures due to laser excitation are already quite high, so the extra local heat due to burning CTAB may not be significant. It is likely that the reason for Ag escaping the particle in this experiment is the same reason as for Ag escaping the particle when heated in an oven under air.[25] What that reason is, is still unclear.

Table 5.8 shows that most likely not the complete fraction of Ag initially present in the particle is lost under laser irradiation. This evidence is, however, not conclusive as the volumes are estimated from a TEM image, which is a 2D projection of the sample. When some Ag initially leaves the particle, the volume loss gives the remaining particle free space in the silica shell. This allows the particle to be deformed more easily. The plasmon resonance of the particle shifts

52

	V_{core} ($10^4\,nm^3$)	V_{total} ($10^4\,nm^3$)	$V_{irradiated}$ ($10^4\,nm^3$)
particle 1	0.6	1.4	1.1
particle 2	0.4	0.9	0.7
particle 3	0.6	2.4	1.1

Table 5.8: Volume of the core and the total volume of the particles before laser irradiation and the volume of the total particle after laser illumination. The volumes were obtained by measuring the width and length of the particle and then calculating the volume for a spherocylindrical or a bullet shape for the particles before and after laser irradiation, respectively.

outside the wavelength range of the laser, due to the resulting aspect ratio loss. Consequently, the laser pulses do not excite the LSPR any longer and energy is no longer efficiently absorbed. This could be the reason why the estimated volume of the irradiated particle is somewhat larger than the volume of just the Au core before laser irradiation.

5.5   Conclusions

In conclusion, we have shown that we can synthesize Au-Ag core-shell NRs of various Au/Ag ratios by etching AuNRs@mesoSiO$_2$ and subsequent Ag deposition by using the method of Deng et al.[95] with a few modifications, such as doing the Ag deposition in an ice bath and using H_2O_2 instead of air as an oxidant in the etching procedure. We characterized samples that we use for heating experiments using BF-TEM imaging and extinction spectroscopy. It was observed that Mie-Gans calculations for single core-shell NRs could qualitatively describe the plasmon resonance wavelengths and relative intensities of measured ensemble measurements. However, it became clear that aspect ratio polydispersity needs to be included to quantitatively describe ensemble spectra, as shown for Au NRs in chapter 4.

The core-shell NPs were used in heating experiments. We first showed that it is possible to alloy Au-Ag core-shell NRs by thermal heating under nitrogen atmosphere at temperatures lower than 300° C for heating times on the order of days. We investigated three samples with different aspect ratios and Au/Ag ratios. The determined activation energies were 2 to 3 times lower than bulk activation energies for these Au-Ag compositions. No large shape dependence on the alloying process could be deduced from the data.

We also performed in-situ heating experiments in the electron microscope on nanospheres and nanorods of similar volumes and Au/Ag ratios. Via EDX mapping, we found that the alloying temperature of both spheres and rods were 400 °C, indicating no shape dependence on the alloying process. We found somewhat lower alloying temperatures for NRs than Albrecht and Van der Hoeven, who found an alloying temperature of 450 °C, with similar time duration per heating temperature, for NRs of the same aspect ratio but 5 times larger volumes.[25] This is likely a size effect. Melting temperatures decrease for NPs smaller than 20 nm,[92] so diffusion could be expected to be faster at low sizes. The alloying temperature of 400 °C we found for spheres is in strong disagreement with the alloying temperature of 930 °C found for spheres of 1.5 times smaller volume by Gao et al.[88]

Lastly, we were not able to alloy the Au-Ag NRs with femtosecond laser pulses. Instead, we observed a volume loss after laser irradiation. This is likely due to the presence of oxygen, which was observed to cause a volume loss due to Ag escaping the particle in thermal heating experiments of Au-Ag core-shell particles.[25]

6   Summary & Outlook

We performed calculations and experiments to investigate the important parameters in plasmon resonances of (bi)metallic NRs. Firstly, we studied the theory of plasmons via Mie-Gans calculations for Au NRs that were employed to study the influence of parameters such as size, aspect ratio and surrounding medium on the LSPR. We extended the calculations to bimetallic Au-Ag systems and looked at the influence of the composition on the plasmonic properties. We found that the resonance wavelengths for both core-shell and alloyed NRs could be tuned by changing the composition of the particles. It was also observed that the strength of the extinction cross section for the alloyed NRs compared to the pure Au NRs got worse for higher aspect ratio, which is due to a higher imaginary part of the dielectric function in the energy regime below 1.8 eV. For the lower aspect ratios, with resonance energies above 1.8 eV, this effect was partly compensated by the shifted onset of interband transitions.

We then moved on to numerical calculations to study the radiative decay mode of the LSPR for Au NPs. With finite-difference time-domain calculations we found that the radiative decay increased linearly with the dielectric constant of the medium around the particle. Besides, the radiation damping at high energies was suppressed. The suppression of the radiation damping was observed for energies above 1.8 eV, at which interband transitions occur. We described the data by a dependence on the imaginary part of the dielectric function of the metal, which describes interband damping. This lead us to the phenomenological description for radiation damping $\Gamma_r = 2\hbar \frac{\kappa_{metal}\varepsilon_m}{\varepsilon_2(\omega_{res})}V$, which described the calculated data reasonably well for the investigated metals Au, Ag, Cu and Al. It also matched experimental data for Au NPs obtain with dark-field scattering experiments.[28,34,35] We used this description to calculate widths of particles for which their plasmon resonance experiences the least amount of damping. We also proposed that the influence of the interband transition on the radiative decay could explain the decrease in the quantum yield quantum yield for photoluminescence of Au NRs below 1.8 eV.[70,71] We believe that the new observation of radiative decay being influenced by interband transitions helps to design optimal systems for decay-mediated applications such as photostable labels for biological sample imaging.[68,106]

We also analyzed ensembles of NRs by using Mie-Gans modelling and experimental ensemble extinction spectra. We managed to extract aspect ratio distributions and concentrations of the sample in a fast and non-destructive way. Furthermore, we investigated the electron-surface scattering contribution to plasmon damping and found $A = 0.30 \pm 0.02$, which is in good agreement with single particle experiments.[34–36,38]

Furthermore, we explored the alloying process in Au-Ag NRs experimentally. For that, we synthesized Au-Ag core-shell NRs with a mesoporous silica shell and used them in heating experiments. Specifically, we performed in-situ heating measurements to study the alloying process using extinction spectroscopy. From these measurements we derived activation energies for diffusion in the NPs that were two to three times lower than activation energies for bulk alloy metals. No shape dependence on the activation energy could be deduced from the few data points. Furthermore, we employed in-situ heating experiments in the electron microscope to compare the alloying rates of nanorods and nanospheres of the same volume and composition. We did not observe a notable difference in alloying temperature for nanospheres and nanorods. We conclude that the alloying process does not depend heavily on shape. The alloyed NRs could only be obtained when heating Au-Ag NRs in inert atmosphere. Attempts to alloy Au-Ag NRs in non-inert conditions by femtosecond laser excitation failed. The synthesized alloyed NRs could be particularly useful in photocatalysis due to their composition and reasonably good plasmonic properties.

Research is never finished and this thesis is no exception. There are a few experiments that would be interesting as a continuation on this work. Firstly, it would be nice to observe the suppression of the radiative decay due to interband transitions in an experimental setting. A dark-field scattering experiment with Au NRs of various aspect ratios and volumes would be a good way of investigating it. By determining the photoluminescence quantum yield of the same particles, we could potentially show the relation between radiative decay and photoluminescence in Au NPs. A lot of research is still to be done on the alloyed NRs. Firstly, it would be interesting to do dark-field scattering experiments on the alloyed NRs to measure the homogeneous linewidth of these particles and compare them with Mie-Gans and FDTD calculations. In order to further study the alloying of the Au-Ag NPs, molecular dynamics simulation would be helpful to research the influence of interface defects and interface shape on the diffusion of the Au and Ag atoms. Experimentally, the experiments in chapter 5 could be expanded. For example, the Linkam cell could be used to study the activation energy for diffusion in a Au-Ag nanosphere. This cannot be done in our current FTIR setup but would need to be done with e.g. a UV-vis spectrometer. Lastly, laser-induced heating of Au-Ag particles can be attempted at lower laser fluences or in an inert atmosphere.

7   Acknowledgements

References

[1] Gustav Mie. Beiträge zur optik trüber medien, speziell kolloidaler metallösungen. *Annalen der physik*, 330(3):377–445, 1908.

[2] R Gans. Über die form ultramikroskopischer goldteilchen. *Annalen der Physik*, 342(5):881–900, 1912.

[3] Uwe Kreibig and Peter Zacharias. Surface plasma resonances in small spherical silver and gold particles. *Zeitschrift für Physik*, 231(2):128–143, 1970.

[4] Babak Nikoobakht and Mostafa A El-Sayed. Preparation and growth mechanism of gold nanorods (nrs) using seed-mediated growth method. *Chemistry of Materials*, 15(10):1957–1962, 2003.

[5] Mingzhao Liu and Philippe Guyot-Sionnest. Mechanism of silver (i)-assisted growth of gold nanorods and bipyramids. *The Journal of Physical Chemistry B*, 109(47):22192–22200, 2005.

[6] Xingchen Ye, Chen Zheng, Jun Chen, Yuzhi Gao, and Christopher B Murray. Using binary surfactant mixtures to simultaneously improve the dimensional tunability and monodispersity in the seeded growth of gold nanorods. *Nano letters*, 13(2):765–771, 2013.

[7] S Shiv Shankar, Akhilesh Rai, Balaprasad Ankamwar, Amit Singh, Absar Ahmad, and Murali Sastry. Biological synthesis of triangular gold nanoprisms. *Nature materials*, 3(7):482–488, 2004.

[8] Jill E Millstone, Sungho Park, Kevin L Shuford, Lidong Qin, George C Schatz, and Chad A Mirkin. Observation of a quadrupole plasmon mode for a colloidal solution of gold nanoprisms. *Journal of the American Chemical Society*, 127(15):5312–5313, 2005.

[9] Isabel Pastoriza-Santos and Luis M Liz-Marzán. Synthesis of silver nanoprisms in dmf. *Nano letters*, 2(8):903–905, 2002.

[10] Yugang Sun and Younan Xia. Increased sensitivity of surface plasmon resonance of gold nanoshells compared to that of gold solid colloids in response to environmental changes. *Analytical Chemistry*, 74(20):5297–5305, 2002.

[11] Jorge Pérez-Juste, Isabel Pastoriza-Santos, Luis M. Liz-Marzán, and Paul Mulvaney. Gold nanorods: Synthesis, characterization and applications. *Coord. Chem. Rev.*, 249:1870–1901, 2005.

[12] Catherine J. Murphy, Tapan K. Sau, Anand M. Gole, Christopher J. Orendorff, Jinxin Gao, Linfeng Gou, Simona E. Hunyadi, and Tan Li. Anisotropic Metal Nanoparticles: Synthesis, Assembly, and Optical Applications. *J. Phys. Chem. B*, 109:13857–13870, 2005.

[13] Na Li, Pengxiang Zhao, and Didier Astruc. Anisotropic gold nanoparticles: Synthesis, properties, applications, and toxicity. *Angew. Chemie - Int. Ed.*, 53:1756–1789, 2014.

[14] David Rioux, Simon Vallières, Sébastien Besner, Philip Muñoz, Eric Mazur, and Michel Meunier. An analytic model for the dielectric function of au, ag, and their alloys. *Advanced Optical Materials*, 2(2):176–182, 2014.

[15] Ovidio Peña-Rodríguez, Magdalena Caro, Antonio Rivera, José Olivares, José Manuel Perlado, and Alfredo Caro. Optical properties of au-ag alloys: An ellipsometric study. *Optical Materials Express*, 4(2):403–410, 2014.

[16] Peter B Johnson and R-W₋ Christy. Optical constants of the noble metals. *Physical Review B*, 6(12):4370, 1972.

[17] Kevin M McPeak, Sriharsha V Jayanti, Stephan JP Kress, Stefan Meyer, Stelio Iotti, Aurelio Rossinelli, and David J Norris. Plasmonic films can easily be better: rules and recipes. *ACS photonics*, 2(3):326–333, 2015.

[18] Robert L Olmon, Brian Slovick, Timothy W Johnson, David Shelton, Sang-Hyun Oh, Glenn D Boreman, and Markus B Raschke. Optical dielectric function of gold. *Physical Review B*, 86(23):235147, 2012.

[19] Peter Zijlstra, James WM Chon, and Min Gu. Five-dimensional optical recording mediated by surface plasmons in gold nanorods. *Nature*, 459(7245):410–413, 2009.

[20] Leonid Vigderman, Bishnu P. Khanal, and Eugene R. Zubarev. Functional Gold Nanorods: Synthesis, Self-Assembly, and Sensing Applications. *Adv. Mater.*, 24(36):4811–4841, 2012.

[21] Jian Feng Li, Yi Fan Huang, Yong Ding, Zhi Lin Yang, Song Bo Li, Xiao Shun Zhou, Feng Ru Fan, Wei Zhang, Zhi You Zhou, De Yin Wu, Bin Ren, Zhong Lin Wang, and Zhong Qun Tian. Shell-isolated nanoparticle-enhanced Raman spectroscopy. *Nature*, 464:392–395, 2010.

[22] Harry A Atwater and Albert Polman. Plasmonics for improved photovoltaic devices. *Nat. Mater.*, 9:205–213, 2010.

[23] Xiaoyan Liu, Aiqin Wang, Xiaofeng Yang, Tao Zhang, Chung-Yuan Mou, Dang-Sheng Su, and Jun Li. Synthesis of thermally stable and highly active bimetallic au- ag nanoparticles on inert supports. *Chemistry of Materials*, 21(2):410–418, 2008.

[24] Suljo Linic, Umar Aslam, Calvin Boerigter, and Matthew Morabito. Photochemical transformations on plasmonic metal nanoparticles. *Nat. Mater.*, 14(6):567–576, 2015.

[25] Wiebke Albrecht, Jessi van der Hoeven, Tian-Song Deng, Petra de Jongh, and Alfons van Blaaderen. Fully alloyed metal nanorods with highly tunable properties. *Nanoscale*, 2017. doi:10.1039/C6NR08484B.

[26] Charles Kittel and Donald F Holcomb. Introduction to solid state physics. *American Journal of Physics*, 35(6):547–548, 1967.

[27] Jana Olson, Sergio Dominguez-Medina, Anneli Hoggard, Lin-Yung Wang, Wei-Shun Chang, and Stephan Link. Optical characterization of single plasmonic nanoparticles. *Chemical Society Reviews*, 44(1):40–57, 2015.

[28] C Sonnichsen, T Franzl, T Wilk, Gero von Plessen, J Feldmann, Ov Wilson, and Paul Mulvaney. Drastic reduction of plasmon damping in gold nanorods. *Physical Review Letters*, 88(7):077402–077402, 2002.

[29] M Moskovits, I Srnová-Šloufová, and B Vlčková. Bimetallic ag–au nanoparticles: extracting meaningful optical constants from the surface-plasmon extinction spectrum. *The Journal of chemical physics*, 116(23):10435–10446, 2002.

[30] Craig F Bohren and Donald R Huffman. *Absorption and scattering of light by small particles*. John Wiley & Sons, 2008.

[31] L Genzel, TP Martin, and U Kreibig. Dielectric function and plasma resonances of small metal particles. *Zeitschrift für Physik B Condensed Matter*, 21(4):339–346, 1975.

[32] Eduardo A Coronado and George C Schatz. Surface plasmon broadening for arbitrary shape nanoparticles: A geometrical probability approach. *The Journal of chemical physics*, 119(7):3926–3934, 2003.

[33] Mingzhao Liu and Philippe Guyot-Sionnest. Synthesis and optical characterization of au/ag core/shell nanorods. *The Journal of Physical Chemistry B*, 108(19):5882–5888, 2004.

[34] Carolina Novo, Daniel Gomez, Jorge Perez-Juste, Zhenyuan Zhang, Hristina Petrova, Maximilian Reismann, Paul Mulvaney, and Gregory V Hartland. Contributions from radiation damping and surface scattering to the linewidth of the longitudinal plasmon band of gold nanorods: a single particle study. *Physical Chemistry Chemical Physics*, 8(30):3540–3546, 2006.

[35] Min Hu, Carolina Novo, Alison Funston, Haining Wang, Hristina Staleva, Shengli Zou, Paul Mulvaney, Younan Xia, and Gregory V Hartland. Dark-field microscopy studies of single metal nanoparticles: understanding the factors that influence the linewidth of the localized surface plasmon resonance. *Journal of materials chemistry*, 18(17):1949–1960, 2008.

[36] Frank Hubenthal. Increased damping of plasmon resonances in gold nanoparticles due to broadening of the band structure. *Plasmonics*, 8(3):1341–1349, 2013.

[37] Yevgeniy R Davletshin, Anna Lombardi, M Fernanda Cardinal, Vincent Juvé, Aurelien Crut, Paolo Maioli, Luis M Liz-Marzan, Fabrice Vallée, Natalia Del Fatti, and J Carl Kumaradas. A quantitative study of the environmental effects on the optical response of gold nanorods. *ACS nano*, 6(9):8183–8193, 2012.

[38] Stéphane Berciaud, Laurent Cognet, Philippe Tamarat, and Brahim Lounis. Observation of intrinsic size effects in the optical response of individual gold nanoparticles. *Nano letters*, 5(3):515–518, 2005.

[39] Vincent Juvé, M Fernanda Cardinal, Anna Lombardi, Aurélien Crut, Paolo Maioli, Jorge Pérez-Juste, Luis M Liz-Marzán, Natalia Del Fatti, and Fabrice Vallée. Size-dependent surface plasmon resonance broadening in nonspherical nanoparticles: single gold nanorods. *Nano letters*, 13(5):2234–2240, 2013.

[40] H Baida, Pierre Billaud, S Marhaba, D Christofilos, Emmanuel Cottancin, Aurelien Crut, Jean Lerme, Paolo Maioli, Michel Pellarin, Michel Broyer, et al. Quantitative determination of the size dependence of surface plasmon resonance damping in single ag@ sio2 nanoparticles. *Nano letters*, 9(10):3463–3469, 2009.

[41] Jonathan A Scholl, Ai Leen Koh, and Jennifer A Dionne. Quantum plasmon resonances of individual metallic nanoparticles. *Nature*, 483(7390):421–427, 2012.

[42] H Hövel, S Fritz, A Hilger, U Kreibig, and Michael Vollmer. Width of cluster plasmon resonances: bulk dielectric functions and chemical interface damping. *Physical Review B*, 48(24):18178, 1993.

[43] K-P Charlé, F Frank, and W Schulze. The optical properties of silver microcrystallites in dependence on size and the influence of the matrix environment. *Berichte der Bunsengesellschaft für physikalische Chemie*, 88(4):350–354, 1984.

[44] Keiko Munechika, Jessica M Smith, Yeechi Chen, and David S Ginger. Plasmon line widths of single silver nanoprisms as a function of particle size and plasmon peak position. *The Journal of Physical Chemistry C*, 111(51):18906–18911, 2007.

[45] Aleksandar D. Rakic. Algorithm for the determination of intrinsic optical constants of metal films: application to aluminum. *Appl. Opt.*, 34:4755–4767, 1995.

[46] Ellen J Zeman and George C Schatz. An Accurate Electromagnetic Theory Study of Surface Enhancement Factors for Ag, Au, Cu, Li, Na, AI, Ga, In, Zn, and Cd. *J. Phys. Chem.*, 91:634–643, 1987.

[47] M A Ordal, Robert J Bell, R W Alexander, L L Long, and M R Querry. Optical properties of fourteen metals in the infrared and far infrared: Al, Co, Cu, Au, Fe, Pb, Mo, Ni, Pd, Pt, Ag, Ti, V, and W. *Appl. Opt.*, 24:4493–4499, 1985.

[48] Martin G Blaber, Matthew D Arnold, and Michael J Ford. Search for the Ideal Plasmonic Nanoshell : The Effects of Surface Scattering and Alternatives to Gold and Silver. *J Phys Chem C*, 113:3041–3045, 2009.

[49] Chen Gong and Marina S Leite. Noble metal alloys for plasmonics. *ACS Photonics*, 3(4):507–513, 2016.

[50] Yoshiaki Nishijima and Shunsuke Akiyama. Unusual optical properties of the au/ag alloy at the matching mole fraction. *Optical Materials Express*, 2(9):1226–1235, 2012.

[51] Stuart W Prescott and Paul Mulvaney. Gold nanorod extinction spectra. *Journal of applied physics*, 99(12):123504, 2006.

[52] Hitoshi Kuwata, Hiroharu Tamaru, Kunio Esumi, and Kenjiro Miyano. Resonant light scattering from metal nanoparticles: Practical analysis beyond rayleigh approximation. *Applied physics letters*, 83(22):4625–4627, 2003.

[53] K Lance Kelly, Eduardo Coronado, Lin Lin Zhao, and George C Schatz. The optical properties of metal nanoparticles: the influence of size, shape, and dielectric environment. *The Journal of Physical Chemistry B*, 107(3):668–677, 2003.

[54] Igor Zorić, Michael Zäch, Bengt Kasemo, and Christoph Langhammer. Gold, platinum, and aluminum nanodisk plasmons: Material independence, subradiance, and damping mechanisms. *ACS Nano*, 5:2535–2546, 2011.

[55] Jack J Mock, David R Smith, and Sheldon Schultz. Local refractive index dependence of plasmon resonance spectra from individual nanoparticles. *Nano Letters*, 3(4):485–491, 2003.

[56] Amit Bansal and SS Verma. Optical response of noble metal alloy nanostructures. *Physics Letters A*, 379(3):163–169, 2015.

[57] Colleen L Nehl and Jason H Hafner. Shape-dependent plasmon resonances of gold nanoparticles. *J. Mater. Chem.*, 18(21):2415–2419, 2008.

[58] Anna Lombardi, Matthieu Loumaigne, Aurelien Crut, Paolo Maioli, Natalia Del Fatti, Fabrice Vallee, Miguel Spuch-Calvar, Julien Burgin, Jerome Majimel, and Mona Treguer-Delapierre. Surface plasmon resonance properties of single elongated nano-objects: gold nanobipyramids and nanorods. *Langmuir*, 28(24):9027–9033, 2012.

[59] Michael B Ross and George C Schatz. Radiative effects in plasmonic aluminum and silver nanospheres and nanorods. *J. Phys. D. Appl. Phys.*, 48:184004, 2015.

[60] Zhongming Li, Weizhi Mao, Mary Sajini Devadas, and Gregory V Hartland. Absorption spectroscopy of single optically trapped gold nanorods. *Nano letters*, 15(11):7731–7735, 2015.

[61] Yang Li, Ke Zhao, Heidar Sobhani, Kui Bao, and Peter Nordlander. Geometric Dependence of the Line Width of Localized Surface Plasmon Resonances. *J. Phys. Chem. Lett.*, 4:1352–1357, 2013.

[62] M Scharte, R Porath, T Ohms, M Aeschlimann, JR Krenn, H Ditlbacher, FR Aussenegg, and A Liebsch. Do mie plasmons have a longer lifetime on resonance than off resonance? *Applied Physics B*, 73(4):305–310, 2001.

[63] A Wokaun, JP Gordon, and PF Liao. Radiation damping in surface-enhanced raman scattering. *Physical Review Letters*, 48(14):957, 1982.

[64] John David Jackson. Classical Electrodynamics. In *Class. Electrodyn.*, chapter 17, pages 600–602. John Wiley & Sons, 1962.

[65] L D Landau and E M Lifshitz. The Classical Theory of Fields. In *Class. Theory Fields*, chapter 9, pages 203–206. Pergamon Press, 3rd revise edition, 1971.

[66] Tavakol Pakizeh. Optical absorption of plasmonic nanoparticles in presence of a local interband transition. *J. Phys. Chem. C*, 115:21826–21831, 2011.

[67] Hui Wang, Felicia Tam, Nathaniel K. Grady, and Naomi J. Halas. Cu nanoshells: Effects of interband transitions on the nanoparticle plasmon resonance. *J. Phys. Chem. B*, 109:18218–18222, 2005.

[68] A Bouhelier, R Bachelot, G Lerondel, S Kostcheev, P Royer, and G P Wiederrecht. Surface Plasmon Characteristics of Tunable Photoluminescence in Single Gold Nanorods. *Phys. Rev. Lett.*, 95:267405, 2005.

[69] E. Dulkeith, T. Niedereichholz, T. A. Klar, J. Feldmann, G. von Plessen, D. I. Gittins, K. S. Mayya, and F. Caruso. Plasmon emission in photoexcited gold nanoparticles. *Phys. Rev. B*, 70:205424, 2004.

[70] Mustafa Yorulmaz, Saumyakanti Khatua, Peter Zijlstra, Alexander Gaiduk, and Michel Orrit. Luminescence quantum yield of single gold nanorods. *Nano Lett.*, 12:4385–4391, 2012.

[71] Ying Fang, Wei-Shun Chang, Britain Willingham, Pattanawit Swanglap, Sergio Dominguez-Medina, and Stephan Link. Plasmon emission quantum yield of single gold nanorods as a function of aspect ratio. *ACS Nano*, 6:7177–84, 2012.

[72] Gregory V Hartland. Optical studies of dynamics in noble metal nanostructures. *Chemical reviews*, 111(6):3858–3887, 2011.

[73] Aurélien Crut, Paolo Maioli, Natalia Del Fatti, and Fabrice Vallée. Optical absorption and scattering spectroscopies of single nano-objects. *Chemical Society Reviews*, 43(11):3921–3956, 2014.

[74] Joel Gersten and Abraham Nitzan. Spectroscopic properties of molecules interacting with small dielectric particles Spectroscopic properties of molecules Interacting with small dielectric particles. *J. Chem. Phys.*, 75:1139–1152, 1981.

[75] Zhongming Li, Weizhi Mao, Mary Sajini Devadas, and Gregory V. Hartland. Absorption Spectroscopy of Single Optically Trapped Gold Nanorods. *Nano Lett.*, 15:7731–7735, 2015.

[76] R L Olmon, B Slovick, T W Johnson, D Shelton, S H Oh, G D Boreman, and M B Raschke. Optical dielectric function of gold. *Phys. Rev. B*, 86:235147, 2012.

[77] David Rioux, Simon Vallières, Sébastien Besner, Philip Muñoz, Eric Mazur, and Michel Meunier. An Analytic Model for the Dielectric Function of Au, Ag, and their Alloys. *Adv. Opt. Mater.*, 2(2):176–182, 2014.

[78] Ninghan Xu, Benfeng Bai, Qiaofeng Tan, and Guofan Jin. Fast statistical measurement of aspect ratio distribution of gold nanorod ensembles by optical extinction spectroscopy. *Optics express*, 21(3):2987–3000, 2013.

[79] Susie Eustis and Mostafa A El-Sayed. Determination of the aspect ratio statistical distribution of gold nanorods in solution from a theoretical fit of the observed inhomogeneously broadened longitudinal plasmon resonance absorption spectrum. *Journal of Applied Physics*, 100(4):044324, 2006.

[80] Ninghan Xu, Benfeng Bai, Qiaofeng Tan, and Guofan Jin. Accurate geometric characterization of gold nanorod ensemble by an inverse extinction/scattering spectroscopic method. *Optics express*, 21(18):21639–21650, 2013.

[81] Boris Khlebtsov, Vitaly Khanadeev, Timofey Pylaev, and Nikolai Khlebtsov. A new t-matrix solvable model for nanorods: Tem-based ensemble simulations supported by experiments. *The Journal of Physical Chemistry C*, 115(14):6317–6323, 2011.

[82] Boris N Khlebtsov, Vitaly A Khanadeev, and Nikolai G Khlebtsov. Extinction and extra-high depolarized light scattering spectra of gold nanorods with improved purity and dimension tunability: direct and inverse problems. *Physical Chemistry Chemical Physics*, 16(12):5710–5722, 2014.

[83] Guillaume Baffou and Romain Quidant. Thermo-plasmonics: using metallic nanostructures as nano-sources of heat. *Laser & Photonics Reviews*, 7(2):171–187, 2013.

[84] Laura C Kennedy, Lissett R Bickford, Nastassja A Lewinski, Andrew J Coughlin, Ying Hu, Emily S Day, Jennifer L West, and Rebekah A Drezek. A new era for cancer treatment: Gold-nanoparticle-mediated thermal therapies. *Small*, 7(2):169–183, 2011.

[85] Alaaldin M Alkilany, Lucas B Thompson, Stefano P Boulos, Patrick N Sisco, and Catherine J Murphy. Gold nanorods: their potential for photothermal therapeutics and drug delivery, tempered by the complexity of their biological interactions. *Advanced drug delivery reviews*, 64(2):190–199, 2012.

[86] Christopher J Orendorff and Catherine J Murphy. Quantitation of metal content in the silver-assisted growth of gold nanorods. *The Journal of Physical Chemistry B*, 110(9):3990–3994, 2006.

[87] Xiong Liu, Mark Atwater, Jinhai Wang, and Qun Huo. Extinction coefficient of gold nanoparticles with different sizes and different capping ligands. *Colloids and Surfaces B: Biointerfaces*, 58(1):3–7, 2007.

[88] Chuanbo Gao, Yongxing Hu, Mingsheng Wang, Miaofang Chi, and Yadong Yin. Fully alloyed ag/au nanospheres: combining the plasmonic property of ag with the stability of au. *Journal of the American Chemical Society*, 136(20):7474–7479, 2014.

[89] Hristina Petrova, Jorge Perez Juste, Isabel Pastoriza-Santos, Gregory V Hartland, Luis M Liz-Marzán, and Paul Mulvaney. On the temperature stability of gold nanorods: comparison between thermal and ultrafast laser-induced heating. *Physical Chemistry Chemical Physics*, 8(7):814–821, 2006.

[90] Tomohiro Shibata, Bruce A Bunker, Zhenyuan Zhang, Dan Meisel, Charles F Vardeman, and J Daniel Gezelter. Size-dependent spontaneous alloying of au-ag nanoparticles. *Journal of the American Chemical Society*, 124(40):11989–11996, 2002.

[91] WC Mallard, AB Gardner, Ralph F Bass, and LM Slifkin. Self-diffusion in silver-gold solid solutions. *Physical Review*, 129(2):617, 1963.

[92] Kimberly Dick, T Dhanasekaran, Zhenyuan Zhang, and Dan Meisel. Size-dependent melting of silica-encapsulated gold nanoparticles. *Journal of the American Chemical Society*, 124(10):2312–2317, 2002.

[93] Adam B Taylor, Arif M Siddiquee, and James WM Chon. Below melting point photothermal reshaping of single gold nanorods driven by surface diffusion. *ACS nano*, 8(12):12071–12079, 2014.

[94] Ivan Gorelikov and Naomi Matsuura. Single-step coating of mesoporous silica on cetyltrimethyl ammonium bromide-capped nanoparticles. *Nano letters*, 8(1):369–373, 2008.

[95] Tian-Song Deng, Jessi ES Van Der Hoeven, Anil O Yalcin, Henny W Zandbergen, Marijn A Van Huis, and Alfons Van Blaaderen. Oxidative etching and metal overgrowth of gold nanorods within mesoporous silica shells. *Chemistry of Materials*, 27(20):7196–7203, 2015.

[96] Eszter Gergely-Fülöp, Dániel Zámbó, and András Deák. Thermal stability of mesoporous silica-coated gold nanorods with different aspect ratios. *Materials Chemistry and Physics*, 148(3):909–913, 2014.

[97] Nikhil R Jana, Latha Gearheart, and Catherine J Murphy. Seeding growth for size control of 5- 40 nm diameter gold nanoparticles. *Langmuir*, 17(22):6782–6786, 2001.

[98] Michael Grün, Klaus K Unger, Akihiko Matsumoto, and Kazuo Tsutsumi. Novel pathways for the preparation of mesoporous mcm-41 materials: control of porosity and morphology. *Microporous and Mesoporous Materials*, 27(2):207–216, 1999.

[99] Gregory Guisbiers, Ruben Mendoza-Cruz, Lourdes Bazan-Díaz, J Jesus Velazquez-Salazar, Rafael Mendoza-Perez, Jose Antonio Robledo-Torres, Jose-Luis Rodriguez-Lopez, Juan Martín Montejano-Carrizales, Robert L Whetten, and Miguel Jose-Yacaman. Electrum, the gold–silver alloy, from the bulk scale to the nanoscale: Synthesis, properties, and segregation rules. *ACS nano*, 10(1):188–198, 2015.

[100] Joongchul Park and Joonho Lee. Phase diagram reassessment of ag–au system including size effect. *Calphad*, 32(1):135–141, 2008.

[101] Ph Buffat and Jean Pierre Borel. Size effect on the melting temperature of gold particles. *Physical review A*, 13(6):2287, 1976.

[102] Clemens Burda, Xiaobo Chen, Radha Narayanan, and Mostafa A El-Sayed. Chemistry and properties of nanocrystals of different shapes. *Chemical reviews*, 105(4):1025–1102, 2005.

[103] Jose H Hodak, Arnim Henglein, Michael Giersig, and Gregory V Hartland. Laser-induced inter-diffusion in auag core-shell nanoparticles. *The Journal of Physical Chemistry B*, 104(49):11708–11718, 2000.

[104] A Arbouet, C Voisin, D Christofilos, Pierre Langot, N Del Fatti, F Vallée, J Lermé, G Celep, E Cottancin, M Gaudry, et al. Electron-phonon scattering in metal clusters. *Physical review letters*, 90(17):177401, 2003.

[105] Wiebke Albrecht, Tian-Song Deng, Bart Goris, Marijn A van Huis, Sara Bals, and Alfons van Blaaderen. Single particle deformation and analysis of silica-coated gold nanorods before and after femtosecond laser pulse excitation. *Nano letters*, 16(3):1818–1825, 2016.

[106] Richard A Farrer, Francis L Butterfield, Vincent W Chen, and John T Fourkas. Highly efficient multiphoton-absorption-induced luminescence from gold nanoparticles. *Nano Letters*, 5(6):1139–1142, 2005.